Title
Microtubule-kinesin based active matter

Author
Tan, Amanda

Publication Date
2020

Peer reviewed|Thesis/dissertation

UNIVERSITY OF CALIFORNIA, MERCED

Microtubule-kinesin based active matter

A dissertation submitted in partial satisfaction
of the requirements
for the degree of Doctor of Philosophy
in Physics

by

Amanda Tan

Committee in charge:
Professor Kevin A. Mitchell, Chair
Professor Bin Liu
Professor Dustin Kleckner
Professor Linda S. Hirst

2020

The dissertation of Amanda Tan, titled Microtubule-kinesin based active matter, is approved and it is acceptable in quality and form for publication in print and electronically:

_____ Date: _____

Professor Kevin A. Mitchell, Chair

_____ Date: _____

Professor Bin Liu

_____ Date: _____

Professor Dustin Kleckner

_____ Date: _____

Professor Linda S. Hirst, Graduate Advisor

University of California, Merced

To Mom and Dad, for your never-ending support and encouragement in everything I do.
Thank you for always believing in me.

Table of Contents

Acknowledgements

First and foremost, I would like to extend my gratitude to my advisor Linda Hirst for her constant support, encouragement, and guidance throughout graduate school. I could not have asked for a better mentor. Her passion and curiosity for science is truly an inspiration. Thank you for always reminding me to be optimistic and helping me grow as a scientist. This work would not have been made possible without your mentorship and I am forever grateful.

Next, I'd liked to express my appreciation to Kevin Mitchell, who was like my second advisor. Thank you for your patience and understanding whenever it came to explaining theory and Matlab to this experimentalist. I'd like to thank my committee members, Bin Liu and Dustin Kleckner, for their advice and helpful discussions about my projects. I'd also like to thank Jing Xu for helpful discussions about microtubules and kinesin and her guidance through my first few years of graduate school. I must extend my gratitude to Sayantani Ghosh and Ajay Gopinathan for all their help and support through CCBM.

I have to thank the members of the Hirst lab, past and present, for making lab a great place to learn and to spend my days. I'd like to especially thank Sheida, Nathan, Chai, Joe, and Alauna for great conversations day in and day out. Next, I want to thank Thinh, Ahmeed, and Mourad of the Muñoz group for always making me feel welcome in their lab and offering invaluable help and advice about proteins and protein purification.

Thank you to Jenny Ross, who introduced me to research and biophysics. She gave me my first exposure to doing research in a lab, and for that I am so grateful.

I could never express enough gratitude to my bio-friends Anna, Megan, and Leslie. Thank you for your constant advice, guidance and friendship over the years. I'm so lucky to have such amazing and inspiring mentors.

To my old friends Kristen, Rachel, Gabriel, Brianna, Dong-Yeop, Jaymes, and Donnie; thank you for sticking with me throughout the years! I can't express how much I appreciate your friendship and always enjoy catching up with each one of you every chance we get.

I have to thank Donald and Dennison who were my first friends when I came to Merced. I'm so proud of all that you two have achieved since graduating.

To my Merced family, Kat, Nivin, Som, Eric, John, Alex, and Molly, thank you for all the laughs and fun that made Merced feel like home. I have learned so much from each one of you during my time here. I am so happy and grateful to have crossed paths with you all and I will cherish these friendships forever. A special thanks to Kat and Nivin who have become two of my closest friends. Our shared love for food (and jamming to Boney M) along with unconditional understanding for each other has created an unbreakable bond.

I want to acknowledge my brotherman and best friend, Jon, who I will always look up to. Thank you for always reminding me to look on the bright side and for showing an enthusiastic interest in everything I do. I can always count on you for a much-needed good laugh!

To Austin, thanks for the adventure, bud! I wouldn't be here without you. Your constant understanding and encouragement kept me motivated to reach the finish line.

Thank you for driving the countless miles (through Kettleman City) over the years, making me laugh when I most needed it, seeing into my brain, and being my go-to person for everything. Sharing all these experiences with you has made this journey exceptional.

Most importantly, I'd like to acknowledge my parents for their unconditional love and support. Their sacrifices gave me opportunities that led me to where I am today. I want to thank my Mom for being my biggest cheerleader and my Dad for always bringing humor into my day. You both have showed me the meaning of hard-work and will always be an inspiration and my role models. I love you both and this is all for you.

I acknowledge the sources of funding NSF DMR-1808926, NSF MRSEC DMR 1420382, NSF-HRD-1547848, UC Merced Faculty Mentor Fellowship, UC Merced President's dissertation fellowship, COR grant from UC Merced, and funding from UC Merced Physics Department.

Curriculum Vitae

AMANDA TAN
(781) 308-1882 | atan25@ucmerced.edu **Citizen status: US Citizen**

EDUCATION

University of California, Merced – Merced, CA
Anticipated Summer 2020 | Ph.D Candidate in Physics | GPA: 3.8/4.0
University of California, Merced – Merced, CA
2017 | M.S in Physics | GPA: 3.8/4.0
University of Massachusetts, Amherst – Amherst, MA
2014 | B.S. in Physics, minor in Mathematics | Commonwealth Honors College | GPA: 3.8/4.0

PUBLICATIONS

• Khaladj, D. A., **Tan, A.J,** Hirst, L.S, "Using epoxy-based lithography to probe confinement effects on active nematics" Proc. SPIE (2019)
• **Tan, A.J**, Roberts, E, Smith, S.A, Alverado Olvera, U, Arteaga, J, Fortini, S, Mitchell, K.A, Hirst, L.S, "Topological Chaos in active nematics", Nature Physics (2019)
• **Tan, A. J.**, Chapman, D. E., Hirst, L. S. & Xu, J. Understanding the role of transport velocity in biomotor-powered microtubule spool assembly. RSC Adv. 6, 79143–79146 (2016).
• Pringle, J, Muthukumar, **A., Tan**, A., Cranksaw, L., Conway,L., and Ross, J.L., "Microtubule organization by Kinesin motors, and microtubule crosslinking protein MAP65," J. Phys.: Condens. Matter, 25, (2013)

RESEARCH EXPERIENCE

University of California, Merced – Merced, CA | 2014-Present
Graduate student research assistant | Dr. Linda S. Hirst
• Conducted kinesin motor purification, tubulin purification from porcine brains, DNA transformation, and microtubule polymerization
• Applied fluid dynamic concepts to describe the dynamics of a microtubule/kinesin motor based active matter system
• Used fluorescence and bright field microscopy to image in vitro active matter assays
• Image analysis using MATLAB and Image J
• Data analysis using MATLAB for particle tracking and Particle Image Velocimetry (PIV) analysis
• (In collaboration with Dr. Jing Xu) Analyzed the role of gliding velocity on microtubule spool formation in microtubule motility assays
• Coated beads with lipid membrane mixtures for multi-motor transport studies
University of Massachusetts, Amherst – Amherst, MA | 2012-2014
Undergraduate research assistant | Dr. Jennifer L. Ross
• Assisted in research with microtubule organization by kinesin motors with MAP-65 in microtubule motility assays
• Studied microtubule organization by kinesin under crowding conditions from polyethylene glycol
• Research focused on kinesin transport in crowded conditions with single-molecule motility assays
• Used epi-fluorescence and TIRF microscopy to image in vitro motility assays
• Data analysis using ImageJ and Kaleidagraph

FELLOWSHIPS/AWARDS

President's Dissertation Fellowship – UC Merced | 2019-2020
GSOFT travel award, American Physical Society-Soft matter topical group | 2019
CCBM Fellow – CREST: Center for cellular and bio-molecular machines, UC Merced | 2019
Physics Department Travel Award, UC Merced | 2015-2020
Physics Department Summer Fellowship, UC Merced | 2018
Award for excellence in contribution to outreach activities in academic year, UC Merced | 2017-2018
CCBM Scholar – CREST: Center for cellular and bio-molecular machines, UC Merced | 2016-2020
Faculty Mentor Program Fellowship – UC Merced | 2016-2017
LeRoy F. Cook, Jr. Memorial Scholarship – UMass Amherst Physics Department | 2014

TEACHING EXPERIENCE

Teaching Assistant, University of California, Merced | 2014-2018
• Lead undergraduate discussion sections and lab
• Courses:

Math 05: Preparatory Calculus
Math 11: Calculus I
Math 12: Calculus II
Math 22: Calculus II - physical sciences and engineering
Physics 08: Introductory Physics I (Mechanics)
Physics 09/09H: Introductory Physics II (Electricity and Magnetism)
Physics 19: Physics II – Bio majors
Physics 108: Thermal Physics

Tutor, Learning Resource Center, University of Massachusetts, Amherst | 2012-2014
•Tutor for introductory math and physics courses
Undergraduate Teaching Assistant for Bio-bootcamp, Ross Lab, UMass Amherst | 2013-2014
•Assisted in training lab techniques for protein purification

PRESENTATIONS

Seminar talk for Saleh Group at UCSB | 2020
Oral Presentation, "Stretching and mixing in a microtubule/kinesin based active nematic"
American Physical Society: Division of Fluid Dynamics – Seattle, WA | 2019
Oral Presentation, "Chaotic mixing in an active nematic in viscous environments"
American Physical Society: March Meeting – Boston, MA | 2019
Oral Presentation, "Chaotic Mixing in a biological active fluid"
Gordon Research Conference: Complex Active and Adaptive Material Systems – Ventura, Ca | 2019
Poster Presentation, "Stretching and Braiding of a biological active nematic"
American Physical Society: Division of Fluid Dynamics – Atlanta, GA | 2018
Oral Presentation, "Characterizing Mixing in a biological active nematic"
American Physical Society: March Meeting – Los Angeles, CA | 2018
Oral Presentation, "Quantifying Mixing in Active Fluids"
Biophysical Society Meeting – San Francisco, CA | 2018
Poster Presentation, "Investigating the quality of mixing of a biological active nematic"
American Physical Society: Far West Section – Merced, CA | 2017
Oral Presentation, "Investigating the mixing quality of a biological active nematic"
American Physical Society: March Meeting – New Orleans, LA | 2017
Oral Presentation, "Fluid dynamics of a biological active nematic"
American Physical Society: Far West Section – Davis, CA | 2016

Oral Presentation, “Understanding the role of transport velocity on bio-motor powered microtubule spool assembly”

Biophysical Society Meeting – Los Angeles, CA | 2016

Oral Presentation, “The effect of active kinesin motor density on microtubules during self-assembly of spools”

American Physical society: Far West Section – Fullerton, CA¬ | 2015

Oral Presentation, “The effect of active motor density of microtubule spool formation”

Biophysical Society Meeting – San Francisco, CA | 2013

Poster Presentation, “The effect of depletion forces on gliding microtubules”

WORKSHOPS/PROFESSIONAL DEVELOPMENT

Advanced Studies Institute– Los Alamos National Laboratory | 2019

Participated in research program development and proposal writing

CCBM Scientific Computing Module – University of California, Merced | 2019

Introduction to scientific computing with Python

CCBM NanoBiofabrication Module – University of California, Merced | 2017

Training in lithography, confocal microscopy, profilometer and focused ion beam (FIB)

Summer school on Soft Solids and Complex Fluids – UMass, Amherst | 2016

Attended lectures on soft matter theory

OUTREACH/COMMITTEES

CCBM Scholar Mentor, CREST: Center for cellular and bio-molecular machines, UC Merced | Fall 2019

Assist in monthly professional development workshops for undergraduate student researchers

Graduate student representative, Division of Soft Matter, American Physical Society | 2019

Student Executive Committee, Physics Department – UC Merced | 2017-Present

- Serve to bridge communication between graduate students and faculty
- Graduate student assistant for department events and recruitment

Peer mentor – Grad Excel Peer Mentor program – UC Merced | 2016-2019

Mentor to 2-3 first year physics graduate students

Classroom Observer at El Capitan High school – Merced, CA | 2015-2016

Assist with physics labs in the classroom

CERTIFICATES

Certificate of Undergraduate Learning Outcomes Assessment: Pedagogy and Program Planning

Participation in lesson planning and creating assessment tools for discussion courses

PROFFESIONAL AFFILIATIONS

American Physical Society | 2014-Present

Biophysical society | 2013-2018

List of Figures

List of Abbreviations

ATP	Adenosine-5'-Triphosphate
AMP-PNP	Adenylyl-imidodiphosphate
DTT	Dithiothreitol
GTP	Guanosine-5'-Triphosphate
GMPCPP	Guanosine-5'-(α,β)-methyleno-triphosphate
h	topological entropy
h'	Dimensionless topological entropy
K_m	Michaelis-Menten constant
MT	Microtubule
M2B	Microtubule Buffer
PEG	Polyethylene Glycol
PDMS	Polydimethylsiloxane
v	velocity
λ	Lyapunov exponent
λ'	Dimensionless Lyapunov exponent
η	Viscosity

Abstract

Active matter is a field that continues to grow in interest because of its widespread relevance to fields such as biology and nanotechnology. Active matter describes systems composed of individual entities that consume energy leading to complex motion. Often, active matter systems exhibit collective motion with emerging patterns, structures, and flows. Active materials can span large length scales ranging from macroscopic (i.e. bird flocks, schools of fish, and marching locusts) to microscopic (i.e. bacterial colonies, self-propelled colloidal particles and proteins). This dissertation explores active matter systems using cytoskeletal proteins, microtubules and kinesin motors.

The first project in this dissertation explores microtubules propelled by kinesin motors that self-assemble into rotating spools. These structures are an example of a potential bio-actuator that can convert chemical energy into mechanical work. Understanding the underlying mechanisms of how to control the spool formation is vital to further development in bio-inspired applications. We explore the role of microtubule gliding velocity during initial spool assembly and once it has reached steady state. Our results show that microtubule spool assembly occurs at a faster rate at higher gliding velocities. Also, slower gliding velocities lead to a lower average spool circumference size. At lower velocities, microtubules do not disperse away from their initial isotropic state as quickly, therefore microtubules are confined to a smaller space when initial spool formation occurs. Once the system has reached a steady state, ~120 minutes later, the gliding velocity no longer plays a role in in spool size or spool density. These results build upon prior work in understanding the fundamental parameters contributing to spool formation.

The second project in this dissertation explores a microtubule-kinesin based active system in a different geometry. Here, kinesin motor clusters crosslink microtubule bundles and form an active network. As the kinesin motors move, the microtubule bundles extend, bend, buckle, fracture and recombine with neighboring bundles. This continuous activity generates complex fluid flows in the network. When confined in two dimensions (2D) at an oil/water interface, spontaneous active ±1/2 topological defects emerge. The ±1/2 defects are reminiscent of defects observed in the nematic liquid crystal phase, which is why the term 2D active nematic was coined to describe the confined network. The topological defects are created and annihilated constantly, which generates fluid flows. Until now, only turbulence was considered to characterize the rich dynamics seen in the network. We take a new approach to study this system from the perspective of chaos and introduce concepts from chaos theory to describe the dynamics generated by the defects. Additionally, we propose to consider the fluid as an active fluid, where the fluid material is the microtubule, that is self-mixed.

We use topological entropy and Lyapunov exponents to quantify the complexities generated in the active nematic. Using two methods to measure the local stretching of the active nematic, our results show there is exponential stretching at the local level which is a characteristic of chaotic advection. Our results show three independent measures of topological entropy that probe the system at different length scales are all consistent and agree with the computed Lyapunov exponent. This consistency demonstrates these

measures of chaos are robust across varying length scales in the system. We then vary the activity in the active nematic by changing the energy injected at the local level (ATP concentration) to study how changes in the dynamics affects mixing. There is a non-monotonic dependence of topological entropy and Lyapunov exponent on the activity level; however, nondimensionalizing these quantities with a time-constant derived from the network velocity and characteristic length scale leads to remarkably constant values for all levels of activity. The insensitivity of the dimensionless topological entropy and dimensionless Lyapunov exponent to activity level indicates that this may be a universal feature.

In the third project of this dissertation, we expand on the second project and explore how the active fluid responds to external changes in its environment. To probe this, we change the viscosity of the bounding oil that the active nematic is in contact with at the oil/water interface. We observe both changes in the dynamics and morphology of the active nematic with changing viscosity. We measure defect pair separations for all viscosities to probe local stretching dynamics in the active nematic. Defect pair separations show exponential stretching at the local level which is consistent behavior to our previous work. Again, there are nonmonotonic relationships observed for both topological entropy and Lyapunov exponent as a function of viscosity; however, dimensionless topological entropy and dimensionless Lyapunov exponents result in relatively constant values. The dimensionless topological entropy is about three times the Lyapunov exponent. The source of this discrepancy is still unclear. We speculate that changes in the morphology that result in defect fracturing may enhance defect stretching but may not be captured in computations for the Lyapunov exponent. More work must be done to fully understand this difference.

Overall in this dissertation we explore interesting structures and collective behavior that arise from active microtubules driven by kinesin motors. In the first project, we contribute to some fundamental understandings for the mechanism behind spool formation that may be useful for future development of bio-inspired nanomachines. In the last two projects we have introduced a new concept to create a bridge between chaotic advection and active nematics. This new perspective introduces possibilities of new analysis methods to understand the fundamental dynamics in the system. Additionally, we have shown early evidence that the active nematic can be considered to be a self-mixing active fluid.

Chapter 1: Motivation and Overview

1.1 What is Active Matter?

A mesmerizing sight in nature is watching hundreds of individual birds fly together in a coordinated fashion, all moving as a single unit. Similarly, shoals of fish exhibit collective behavior when they all swim together in a school for reasons such as defense against predators or increasing chances for foraging food. These examples of collective motion fall under a broader category of materials called active matter.

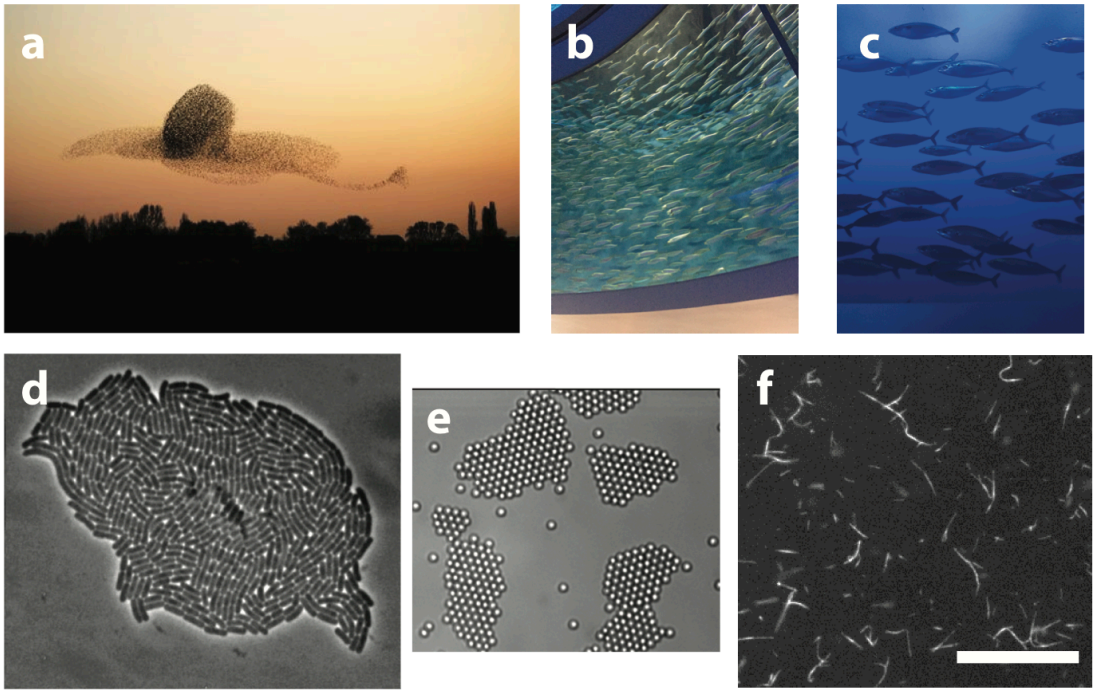

Fig. 1.1) Examples of active matter. a) A flock of birds form a coherent pattern (reproduced from Popkin, 2016 with permission ©2016 Springer Nature). b) A school of fish swim collectively in the same direction at the Monterey Aquarium. c) A group of fish show local alignment. d) Bacteria colony growing forming defects (reproduced from Dell'Arciprete et al, 2018 with permission © 2018 Springer Nature). e) Self-propelled synthetic colloidal suspension forming clusters (adapted from Palacci et al, 2013 with permissions ©2013 The American Association for the Advancement of Science). f) Microtubules bound to kinesin motors gliding. Scale bar, 50μm.

Active matter refers to groups of objects that individually consume energy and move collectively. As the units move together, large-scale patterns and flows spontaneously emerge, as in the bird flocks and schools of fish[1,2]. A constant supply of

energy must be available for the particles in order to maintain the flocking and fluid flows observed in the active steady state. This requirement separates active systems from ordered systems in equilibrium since equilibrium systems can maintain their ordered structure once the system reaches its ground state. What's unique about active matter is that the behavior spans a large range in scales. Figure 1.1 shows active matter examples from the macroscopic scale seen in animals, as mentioned before, down to the microscopic scale, with bacteria colonies[3] and proteins[4–6]. Not only does active matter refer to biological systems and processes, but also, this collective motion has been observed in synthetic materials with self-propelled colloidal particles[7–9] and agitated granular rods[10]. Since these individual components constantly consume energy, active matter systems operate far-from equilibrium, therefore equilibrium statistics cannot be used to describe these rich dynamics.

Common biological processes involve self-assembly, self-organization, and collective motion. For example, microtubules, which are biopolymers, self-assemble into hollow tubes from smaller tubulin protein subunits. Actin, another biopolymer, self-assembles into filaments from globular protein subunits. These biopolymers often self-organize during important cell processes such as cell division, muscle contraction, and cell motility. During cellular trafficking, microtubules create these highways allowing molecular motors, such as dynein and kinesin to travel along to deliver cellular cargo. All these processes rely on energy consumption in order to function properly.

Biological processes self-organize and self-assemble efficiently and are a main inspiration for studying active matter systems. Using biological materials gives insight to the mechanisms driving efficient self-organization and self-assembly. Understanding these mechanisms helps to extend active matter to synthetic materials where we can harness these unique properties in biology to create new materials. Exploring active matter experimentally and developing theories that accurately describe the rich nonequilibrium dynamics is crucial to understanding biological processes and extending their properties to creating new materials.

1.2 Active Matter Models

One of the first models presented to describe clustering, transport, and phase transitions in nonequilibrium systems was developed by Tamás Vicsek in 1995. His model is an active analog to the equilibrium model that describes ferromagnetic alignment of neighboring spins. Vicsek's model imposes a simple rule where particles driven at a constant velocity align in the average direction of motion of the particles in the neighborhood of radius, r, at every time step, with some random added perturbation[11]. Here, the alignment of particles in a specific direction of motion is analogous to ferromagnetic interactions that lead to spin alignment. Additionally, the random added perturbations (noise component) is analogous to temperature in the ferromagnetic picture.

Simulations from Vicsek's model resulted in realistic dynamics and kinetic phase transitions similar to those seen among biological examples. In the simulations, the particles were placed in a square shaped cell with length, L, and periodic boundaries. Tuning the particle density and noise, η, leads to different phases of the system shown in Figure 1.2. The particle density, ρ, is given by

$$\rho = \frac{N}{L^2}$$

where N is the number of particles, and L is the box length. In its initial state, the particles are random and have disordered motion as shown in Fig. 1.2a. As density and noise decrease, the particles start to form groups and move coherently, similar to clustering shown in Fig. 1.2b. At higher density and noise, the particles will move randomly but in a correlated direction shown in Fig. 1.2c. Finally, when particles are at a high density and low noise, the particles spontaneously have ordered motion that can be seen macroscopically as shown in Fig. 1.2d. From this simple model, it was evident that these active particles undergo a phase transition where the kinetic order parameter goes from 0 to 1, which is very similar to that seen in passive liquid crystals.

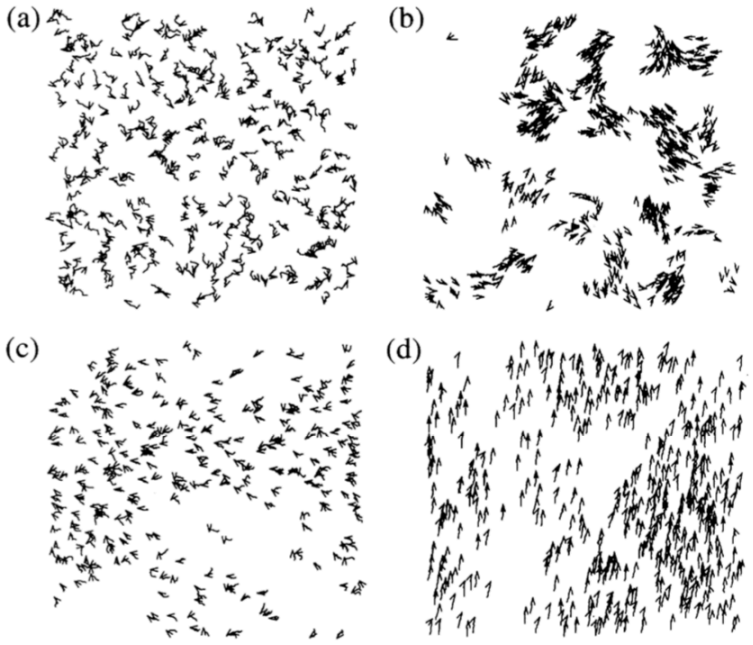

Fig. 1.2) The velocity and trajectory of a system of particles with varying density and noise from the Vicsek model. The short arrow indicates the velocity, and the line indicates the trajectory of the particle measured in the last 20 frames. All cases have N=300 particles, and each case has varying box width, L, and noise, η. a) t=0, L=7, η=2.0. b) L=25, η=0.1. At smaller densities and noise, particles form coherent clusters. c) At later time t, for L=7, η=2.0, particles start to flock and move in coherent directions collectively. d) L=5, η=0.1. At high density with low noise, the particles are ordered. (reproduced from Vicsek, 1995 with permission © 1995 American Physical Society)

Vicsek's model was the starting point for developing a theory to describe coherent motion of active particles. More theoretical frameworks were established by writing hydrodynamic equations for the evolving macroscopic fields. To describe the non-equilibrium dynamics of these fields, the hydrodynamic equations are often built from

well-known hydrodynamic equations describing liquid crystals with the addition of driving terms to account for the activity[12].

One of the first models using a hydrodynamic approach came out shortly after Vicsek's, by John Toner and Yuhai Tu in 1995[13]. Toner and Tu modeled the swarms as a continuous fluid using hydrodynamic equations with the addition of a convective term. Despite only having short-range interactions, they found long-range ordering in moving herds. Their results showed symmetry breaking consistent with the simulations by Vicsek et al.

Theoretical models to explain nonequilibrium dynamics of collective motion continued to develop as more experimental examples emerged. For example, self-propelled elongated particles suspended in a fluid[10] and active filament suspensions[14] exhibit the additional order of alignment because of the geometry of the particles. Using a hydrodynamics approach, models extended to describe self-propelled elongated particles by incorporating terms that account for the particle alignment, and the energy costs from distortions in local particle alignment. In active systems, the local distortions have shown to move and exhibit defect pair creation and annihilation events[4,15]. Much theoretical work has been done to study the role of distortions in fluid flow generated in these active systems[15–17]. Another topic of interest for theorists is to predict the behavior of propelled particles in confined geometries such as cylindrical cylinders[18], and channels[19]. Predicting the behavior of these materials in confined boundaries may provide insight into control and pattern formation in collective motion.

Theoretical models are important to mathematically tie what is observed in nature to physical phenomena. Additionally, it provides a coherent picture of the common underlying rules governing collective behavior. These models are continuously changing as more experimental examples of collective motion emerge; however, predictive theoretical models also provide inspiration to new experiments.

1.3 Collective motion in biological and synthetic materials

As new theories for active matter continue to evolve, physical experiments demonstrating collective motion have arisen alongside them. Experimental work in self-assembly and collective motion with biological materials range from large-scale locusts[20], down to the microscopic scale with bacteria colonies and cytoskeletal filaments and molecular motors. Collective motion also has been observed in synthetic materials like self-propelled colloids[7,21] and mechanically agitated flocks[10]. The fascinating aspect of these materials is, living or not, that collective motion leads to large-scale emergent patterns and flows. The fundamental difference between these active systems and other externally driven systems is that the energy is injected locally on the scale of the individual units as opposed to receiving energy from the environment.

Early experiments in the field involved the use of reconstituted biological components *in vitro,* where after energy introduction to the system, the components were able to move and self-assemble. These experiments also provided a new method to study the biophysics of cellular processes.

In 1986, Kron and Spudich published work that was the first *in vitro* experiment done where molecular motors are fixed onto a glass surface and cytoskeletal filaments were

propelled above it[22]. More specifically, myosin motors were fixed onto a glass surface, and actin filaments were bound to the motors. Actin and myosin are two main proteins responsible for muscle contraction. In the presence of an energy source, adenosine-5'-triphosphate (ATP), the motors begin to walk along the filaments, forcing the filaments to move[22]. They were able to measure the ATP dependence of actin gliding velocity and concluded that the velocities were comparable to their previous experiments where myosin motors walked along actin filaments[22]. The discovery of this assay created a huge impact in biophysical studies of cytoskeletal filaments and motor proteins, as well as studying collective motion.

In 2010, Andreas Bausch's group used motility assays with actin and myosin to experimentally show that collective motion emerges at high-density of filaments[6]. The driven actin filaments exhibited a disordered phase at low density and ordered phase once the filament density reached a critical concentration. In the ordered phase, there were intermediate phases with coherent moving clusters and as filament density increases, density waves formed[6]. The clusters constantly lose filaments and recombine with new filaments as the clusters move around. Beyond a threshold density in the ordered regime, the filaments begin to move in stable band structures in waves. There is a minimal orientational ordering that continues to persist as the waves move[6]. Another interesting phenomena the group observed was that at concentrations higher than the critical concentration, a swirling pattern emerges where the filaments rotate[6]. The observations from this work complemented the prior work done in describing active fluid theory and introduced new controlled experiments to study phase transitions in active materials.

Although much work has been done with biological systems since they inherently consume energy and move, clustering in collective ensembles has also been observed with synthetic materials. In 2012, Theurkauff et al. studied the collective motion of active colloidal particles that were half coated in gold, and half coated in platinum[1]. These active colloids are dispersed in hydrogen peroxide solution and the mechanism driving their self-propulsion is a combination of self-electrophoresis and diffusiophoresis[7,23] (there's a concentration gradient when the hydrogen peroxide is catalyzed). At high-density these synthetic self-propelled particles exhibited dynamic clustering. In another example, using agitated granular rods, Narayan et al. showed coherent motion and spontaneous local alignment emerging from a synthetic material where the only communication between neighboring particles is by contact[10].

It is interesting to see that common phenomena seen in biological systems can be recreated using synthetic materials. This is a promising result because it shows that there may be some universal rules dictating the collective behavior that can be applied to both biological and synthetic materials. The remainder of this dissertation will focus on collective organization using biological materials.

1.4 Overview

In Chapter 1, I introduced active matter with common examples seen in nature. All living things fall into the category of active matter; however, energy-consuming synthetic materials have also been observed to share characteristics of collective behavior. These non-equilibrium systems demonstrate rich dynamics that are both interesting to theorists

and experimentalists. Section 1.2 introduced early models and theoretical frameworks used to describe these collective dynamics. Finally, section 1.3 discusses early experimental systems that demonstrated collective behavior. These experiments created a large impact in the active matter community allowing for tunability and further exploration of the field in a controlled way. Studying and understanding active matter and the fundamental rules governing collective behavior can lead to new materials with unique properties. Biological processes inherently operate out-of-equilibrium and work collectively to perform specific tasks. Using biological materials to study active matter is a great way to learn about the underlying rules driving the collective phenomena. In this dissertation, I will discuss using a cytoskeletal filament, microtubules, and their associated molecular motor proteins, kinesin, to study collective organization and collective motion.

This dissertation will be organized as follows:

Chapter 2 will provide basic theory and background on materials and concepts that is relevant to the projects discussed in this dissertation.

Chapter 3 will discuss the role of transport velocity in a system where microtubules propelled by kinesin motors form rotating spools.

Chapter 4 will discuss measuring topological chaos in a microtubule active nematic network.

Chapter 5 will discuss the effects of viscosity on the transport properties of a microtubule active nematic.

Chapter 6 will conclude with overall conclusions and future directions.

Chapter 2: Background and Theory

2.1 Review of materials: Microtubules and motor proteins

The main materials used for the work described in this dissertation are microtubules and kinesin motors. The following section will discuss background information on these materials and review the literature on self-assembled structures *in vitro* and collective behavior in dense systems.

2.1.1 Microtubules

Microtubules are biopolymers that play a crucial role in eukaryotic cells. These biopolymers are part of the family of filaments that make up the cytoskeleton. The cytoskeleton is a complex, dynamic network of protein filaments found in the cytoplasm of cells. Microtubules provide structural support in the cell, and are responsible for crucial cellular processes, such as cell division and intracellular cargo transport. Microtubules form hollow cylindrical structures that have a 25 nm outer diameter and 17 nm inner diameter, shown in Fig. 2.1c. They can grow to varying lengths up to 100's of nanometers.

Microtubules are biopolymers composed of αβ-tubulin heterodimers shown in Fig. 2.1b. There is typically a high concentration of tubulin protein in brain tissue. Methods for purification of tubulin protein from porcine brain tissue can be found in the appendix (A.2). The tubulin dimers polymerize in the presence of guanosine-triphosphate (GTP) to form microtubules. Individual dimers will bind together in a head-to-tail fashion in a chain called a protofilament. Both polar and hydrophobic interactions play a role in the longitudinal interactions between dimers[24]. The protofilament is polarized based on the orientation of the dimers as they bind together. The protofilaments interact laterally at an angle to form sheets that then form the cylinder structure of the microtubule[25]. Microtubules have an intrinsic helical structure on the surface because the protofilaments are not perfectly aligned laterally. *In vivo*, 13 protofilaments join together to make the microtubule; however, microtubules made *in vitro* can have 12 – 15 protofilaments[26].

The overall structure of the microtubule is polarized with a plus-end and a minus-end (Fig. 2.1a). Each monomer has a GTP binding site. The GTP binding site on the α monomer is non-exchangeable, whereas the binding site on the β-monomer is exchangeable. The non-exchangeable binding site means the GTP is not hydrolysable, whereas the exchangeable binding site is hydrolysable. At the exchangeable binding site, the GTP can lose a phosphate group and turn into guanosine-diphosphate (GDP). The non-exchangeable binding site on the α-tubulin is known as the N-site and the exchangeable binding site on the β tubulin is known as the E-site. When a new dimer binds to another dimer, the GTP at the E-site hydrolyzes. There is a time-lag between polymerization and GTP hydrolysis, so there is typically a section of the microtubule with GTP-bound tubulin. This section is known as a GTP cap[24,27,28].

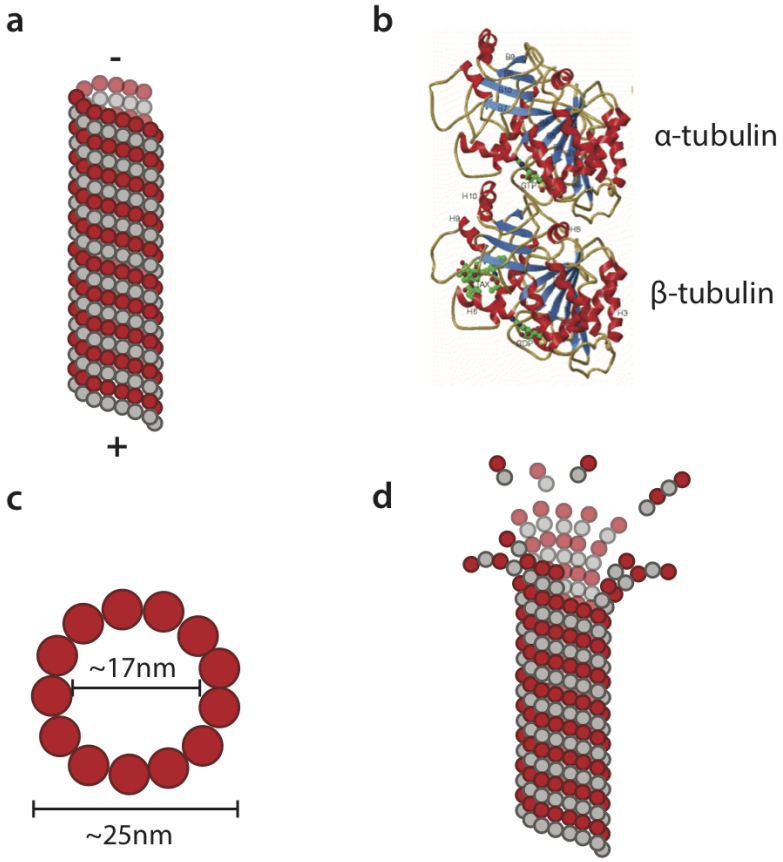

Fig. 2.1) a) Schematic of microtubule comprised of α-tubulin (red) and β-tubulin (grey). The end of the microtubule that has mostly β-tubulin exposed is labeled the plus-end and the end with α-tubulin exposed is the minus-end. b) Ribbon diagram of αβ-tubulin heterodimer showing the GTP binding sites (Adapted from Nogales, 1998 with permission © 1998 Springer Nature) c) Schematic of the dimensions of the cross section of a microtubule. d) Schematic of microtubule disassembly where protofilaments peel away by curling backward.

Microtubules undergo dynamic instability meaning they can go through cycles of growth and shrinking. Dynamic instability is important for processes like cell division. It has been shown that microtubules remain in the growth phase when there is a sufficient GTP cap on the lattice[25,28]. Ends without the GTP cap are unstable and can lead to depolymerization[25,28]. Cryo-electron microscopy studies show that when the microtubules are in the growth phase, the protofilaments remain straight; however, when the microtubules are in a shrinking phase, the protofilaments peel off by curling backward into a ring[25]. Evidence suggests that GTP-bound tubulin enforces a straight conformation in the protofilament, and hydrolyzing GTP causes a conformational change forcing the protofilament to bend and curl[25,29].

This disassembly is often unwanted in studies regarding collective motion, so microtubules can be stabilized to avoid spontaneous depolymerization. Two common

methods of stabilizing microtubules are using Paclitaxel[30], a cancer therapeutic drug, or guanylyl-(alpha, beta)-methylene-diphosphonate (GMPCPP)[31,32], a slowly hydrolysable analog of GTP. Paclitaxel, or Taxol, is a hydrophobic molecule that binds to the inside of the β-tubulin and stabilizes the lateral bonds of the microtubule.

The rigidity of the microtubules depends on the concentration of Taxol used to stabilize the filaments. Persistence length is often used to characterize microtubule flexibility. Persistence length is defined as the length over which correlations along the tangent of the filament drops off[33] and is defined using this the following formula

$$< cos\theta \geq e^{\frac{\Delta L}{2L_p}}$$

where L_p is the persistence length of the filament, and θ is the angle between two tangents along a filament ΔL apart (Fig. 2.2)[33]. Another way to understand persistence length is the length at which thermal fluctuations at 300K can bend a filament. For example, the thermal persistence length of uncooked spaghetti is 10^{18} m, which means its stiffness is such that it need 10^{18} m of length for thermal fluctuations to bend it.

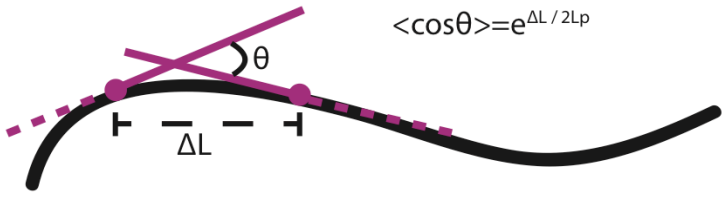

Fig. 2.2) Determining persistence length. Schematic of the angle, θ, between the tangent lines of two points (purple) along a curve. The distance between these two points is labeled ΔL.

The persistence length of microtubules stabilized with low concentrations of Taxol (10μM) is about 5 mm[34] and microtubules stabilized with higher concentration (50 μM) are more flexible with a persistence length of 0.6 mm[32]. Methods of polymerizing Taxol-stabilized GTP microtubules can be found in the appendix (A.3).

GMPCPP prevents microtubules from depolymerization because it takes more energy to hydrolyze GMPCPP than GTP. GMPCPP-stabilized microtubules, however, result in short and stiff filaments[31,35]. The average persistence length of GMPCPP-stabilized microtubules is about 1.8 mm[32]. The average length of these microtubules is tunable by changing the initial concentration of tubulin used to polymerize microtubules. Increasing the initial concentration of tubulin used in polymerization in the presence in GMPCPP results in shorter filaments[36]. Methods on polymerizing GMPCPP microtubules can be found in the Appendix (A.8).

2.1.2 Motor Proteins

Molecular motors are essential components for movement in living things. These molecular motors convert chemical energy into mechanical work. Molecular motors operate at a scale where thermal fluctuations in its environment are significant. In biology, molecular motors are largely responsible for maintaining proper cellular function. Myosin motors are associated with actin filaments and are used in muscle contraction. Molecular motors associated with microtubules include dynein and kinesin and both are required in cellular cargo transport. Small molecules are transported by diffusion within the cell; however, for larger biomolecules, diffusion is too slow to be an effective transport mechanism, so these processes rely on active transport by molecular motors. These cytoskeletal tracks and molecular motors help facilitate transport of materials at faster timescales. For the purposes of this research, I will focus on kinesin motors for the remainder of this dissertation.

Kinesin-1 motors, or conventional kinesin, is part of a family of proteins responsible for maintaining internal function within a eukaryotic cell by transporting cellular cargo along cytoskeletal filaments. Kinesin was first discovered by Vale et al. in the axoplasm of giant squid and bovine brain[37]. They found that purified kinesin can facilitate organelle transport along microtubules in one direction, as well as induce movement of microtubules on a glass slide in the presence of ATP[37].

Up until that point, dynein was the only known microtubule-associated motor protein. This new motor purified from giant squid and bovine brain was not only structurally different from dynein, but also, had different enzymatic properties. For example, AMP-PNP (adenylyl-imidodiphosphate, a non-hydrolyzable analog to ATP) causes a decrease in dynein affinity to microtubules, whereas there is an increase in kinesin affinity to microtubules in the presence of AMP-PNP[37]. Vale et al. ultimately named this new motor protein, Kinesin, after the Greek word *kinenin*, meaning to move. This discovery led to a better understanding of bi-directional organelle transport on a single microtubule and sliding of microtubules during mitosis[38].

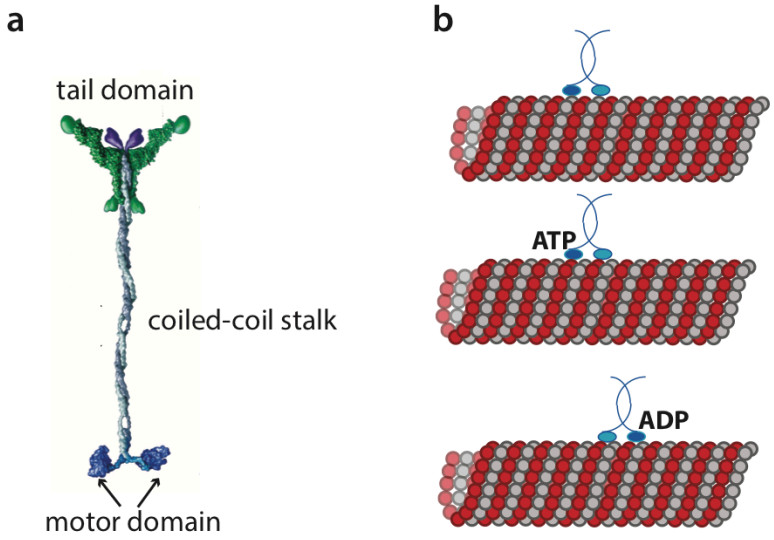

Fig. 2.3) a) Kinesin-1 structure contains two motor domains, a long coiled-coil stalk with a central hinge, and the tail domain (adapted from Vale, 2003 with permission ©2003 Elsevier). b) Schematic of kinesin-1 hydrolyzing ATP to ADP to take a step along the microtubule toward the plus-end.

The structure of kinesin-1, which will be referred to as kinesin for the remainder of this dissertation, contains an N-terminal motor domain, a long coiled-coil stalk with a central hinge and a globular tail domain, shown in Fig. 2.3a. The motor domains bind to the microtubule through electrostatic interactions[39]. The tail domain is responsible for folding into an autoinhibited conformation, or binding to cargo[40]. Kinesin motors have been largely studied in both fungi (*Ustilago*, *Neaurospora*, and *Dictyostelium*) and metazoan systems. In fungi systems, kinesin have been known to transport membrane vesicles. Kinesin found in metazoan systems transport both membrane cargoes, such as mitochondria, lysosomes, endoplasmic reticulum, and anterograde-moving vesicles in the axon, and non-membranous cargo, such as mRNA[40]. *In vitro* experiments showed that kinesin motors were required for transporting vesicles along microtubules[41]. Kinesin motors used for *in vitro* studies are typically truncated with enough of the coiled-coil to help dimerize the motor domains, but does not contain the hinge and tail responsible for autoinhibition.

Kinesin is highly processive, i.e. it takes more than 100 steps along a microtubule before dissociating and falling off[42]. This motor converts chemical energy into mechanical motion by hydrolyzing one ATP molecule per step along the microtubule filament[43]. Kinesin walks along the microtubule in a hand-over-hand motion, taking 8 nm steps[44], shown in Fig. 2.3b. The motor alternates between a two-head bound state, where both motor domains are bound to the filament, and a one-head-bound state, where one of the heads (the tethered head) remains free from the microtubule[44]. The motor velocity is related to ATP concentration by Michaelis-Menten kinetics[43]. This allows kinesin motor activity to be highly tunable by controlling the amount of ATP available.

2.1.3 Michaelis-Menten Kinetics

Michaelis-Menten kinetics describe enzyme-catalyzed reactions. Enzymes are protein catalysts that lower the activation energy, or the energy required for the reaction to start, of a reaction process and speeds up biological processes. Enzymes bind to a substrate, which is a molecule or atom on which the enzyme acts on, to create an enzyme-substrate complex. Michaelis-Menten kinetics relates how the rate of an enzyme catalyzed reaction is related to the concentration of a substrate, [S].

Catalytic enzyme reactions on a substrate can be described by two parameters: the Michaelis constant, K_m, and the maximum rate of the reaction at saturating levels of substrate, V_{max}. The Michaelis constant describes the enzyme affinity for the substrate. Smaller K_m values indicate the enzyme can bind more easily to a substrate from a dilute concentration of substrate and a smaller amount of substrate to reach the half-maximal reaction rate.

In the reaction, 1) a substrate binds to the enzyme, 2) catalysis occurs forming an enzyme-product complex, and 3) the product is released resulting in a free enzyme and product.

$$E + S \rightleftharpoons ES \longrightarrow E + P$$

The Michaelis-Menten equation that describes this reaction is given by

$$v = V_{max} \frac{[S]}{[S] + K_m}$$

where v is the rate of the reaction, and [S] is the substrate concentration. Fig. 2.4 shows an example of reaction rate as a function of substrate concentration. Kinesin motors stepping rate follows this kinetics where ATP is the substrate and the kinesin motors are the enzymes. ATP binds to the kinesin motor domain and hydrolyzes a phosphate group, turning ATP into ADP.

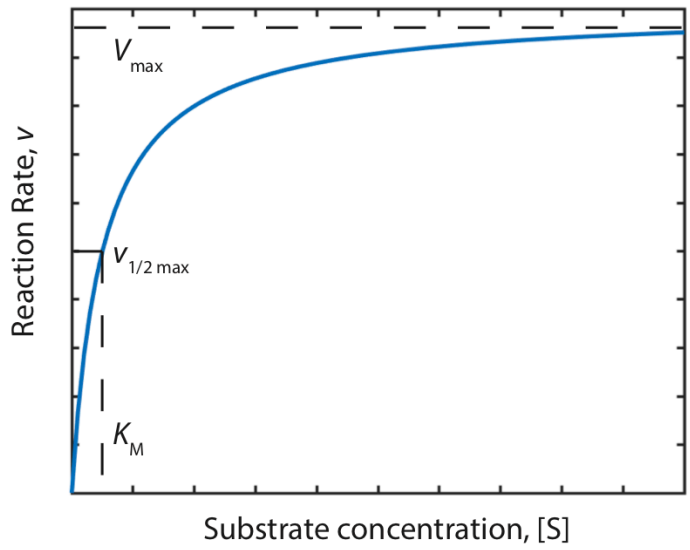

Fig. 2.4) Michaelis-Menten kinetics. Enzyme reaction rate, v, as a function of substrate concentration. Enzyme reactions following Michaelis-Menten kinetics saturates at V_{max}. The concentration at which the reaction rate reaches ½ max is the parameter K_m.

2.2 Microtubule-kinesin based collective motion

Within the cell, important cellular structures self-assemble. These cellular processes rely on regulating proteins to function properly. Microtubules and kinesin motors are commonly used to study cytoskeletal organization and collective motion *in vitro*. *In vitro* studies are a useful tool to isolate specific proteins to study their interactions and roles in organization. Also, microtubules and kinesin motors are good building blocks for studying collective motion because the systems can be highly tunable. Adjusting specific parameters provides better insight to the underlying mechanisms driving the collective dynamics. The following section will discuss prior work done with microtubule-kinesin based assays to study self-assemblies, organization, and collective patterns.

2.2.1 Self-assemblies

An important part of cell development and cell function is self-assembly of microtubules and molecular motors. For example, microtubules and molecular motors self-assemble into spindles, centrioles and asters that play a role during cell division. These cellular structures inspired *in vitro* studies to understand the mechanisms driving the formation of the structures.

During cell morphogenesis, microtubules self-organize to form bipolar spindles. Early studies of microtubule self-organization were motivated by understanding the mechanism behind the bipolarity and microtubule orientation in the mitotic spindle. Heald et al.[45] discovered microtubules can self-organize into bipolar spindles from mitotic

chromatin and does not require the centrosomes or centromeric DNA that was formerly thought to have a crucial role dictating the bipolarity and microtubule organization. This group demonstrated chromatin-coated beads were sufficient to direct spindle assembly and the bipolarity of microtubules is intrinsic to how the filaments assembly around the mitotic chromatin. Then, using polarity marked microtubules, they showed dynein-dependent microtubule sliding are responsible for sorting microtubule minus-ends to the poles[45].

To study the role of microtubules and molecular motors during spindle formation Nédélec et al. created a simplified model experiment only consisting of microtubules and kinesin motors. Fig. 2.5a shows a schematic of the experimental components. The kinesin motors were functionalized with biotin and clustered together with streptavidin. Biotin, also known as vitamin B7, has a strong affinity for the protein streptavidin and forms a strong non-covalent bond. Using just these two components, microtubules self-assembled into asters. Previously, Urrutia et al. also observed aster formation from a mixture of kinesin motors and microtubules[41] Under circular constraints, the microtubules first form the asters and then the active drives the network for form a vortex. When confined to a torus, the microtubules formed a steady-state structure with vortices of the same core size.

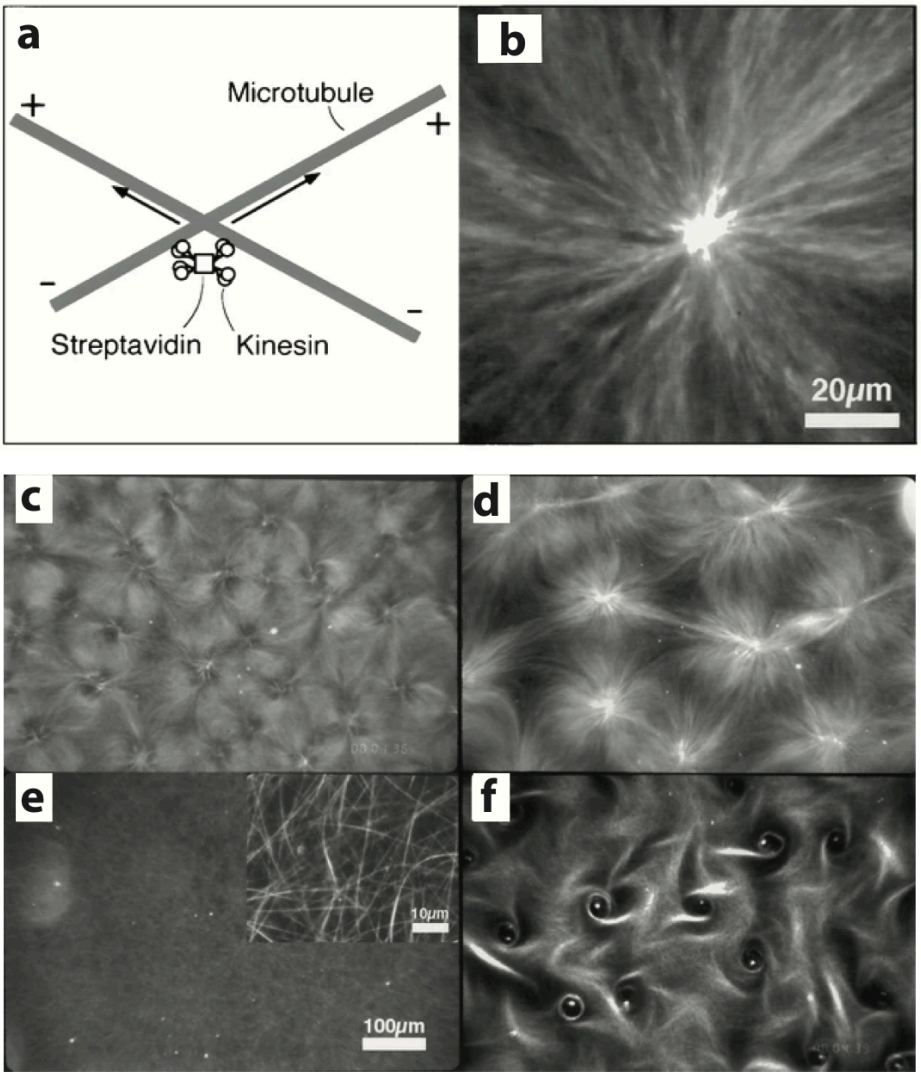

Fig. 2.5) Lattice of vortices form from a microtubule kinesin complex a) Schematic of the microtubules crosslinked by kinesin clustered by streptavidin. b) A dark-field microscopy image of an aster self-organized by kinesin motors and taxol-stabilized microtubules. The bright center indicates a collection of motors and microtubules. c-f) Pattern formation from dynamic microtubules with varying concentrations of kinesin motors. c) Vortex and aster lattice formed with ~25 μg ml^{-1} kinesin. d) Aster lattice formation with ~37.5μg ml^{-1} kinesin. e) At ~50μg ml^{-1} kinesin concentration, microtubules formed bundles. f) A lattice of vortices form at low concentrations of kinesin motors (< 15μg ml^{-1} kinesin). (Reproduced from Nédélec et al. 1997 with permission ©1997 Springer Nature)

Additionally, the group studied unconfined dynamic microtubules with varying kinesin concentrations[5]. Varying the concentration of kinesin motors changes the overall system organization shown in Fig. 2.5c-f. The microtubules organized into asters, a combination of asters and vortices, vortices, and bundles depending on the concentration

of kinesin motors. In this simplified system, they have shown organizing into specific structures is highly sensitive to the motor and tubulin concentration; however, this may not be the case within a cell since the cell has regulatory processes that control these self-assemblies, such as the use of associated binding proteins or covalent modifications[5].

Using a similar experimental setup, self-assembled bundles bound on one end to the boundary exhibited similar beating patterns found in cilia[46]. Since the bundles are attached to the boundary, the bundles self-oscillate. An important component in this system is the addition of polyethylene glycol (PEG) as a depleting agent to help push the microtubules together. Although both *in vitro* and *in vivo* cilia systems are composed of microtubules, the minimal model system described here has significant differences from biological axonemes. Biological axonemes contain microtubules and more that 650 different proteins[47], whereas the model system only has three main components. Despite this difference, the beating patterns from this *in vitro* system, can shed light on the mechanisms that drive the oscillations in biological systems[1].

A variety of self-organized structures can emerge from experimental model systems using minimal components. Reducing the system down to a few components is valuable in understanding the roles of specific proteins during self-organization. Addition of more components to these model systems will provide more insight to how self-organization is regulated. Seeing that these *in vitro* experiments are able to replicate mechanisms that drive formation of biological structures opens up an avenue for utilizing these mechanisms to develop novel structures not seen in biology.

2.2.2 Assemblies from motility assays

Motility assays are another experimental setup used to study interactions between molecular motors and cytoskeletal filaments. Microtubule and kinesin motors have been used extensively in motility assays to study self-assembly and collective motion. Similar to the motility assay using myosin and actin[22], Vale et al. successfully used kinesin motors to show that this protein was also able to translocate microtubules on a glass surface and transport beads along microtubules[37].

In motility assays, molecular motors are immobilized on a substrate and microtubules are bound above them, shown in Fig. 2.6. Since the kinesin motors walk in one direction along the microtubule filament, once the kinesin start walking, the microtubules are propelled forward with the minus head leading the way. This experimental setup is a versatile system that allows for studies on biophysical interactions that affect cytoskeletal filament organization and studies about collective motion.

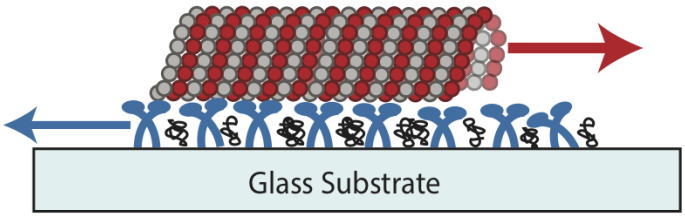

Fig 2.6) Schematic of microtubule motility assay. Kinesin motors (blue) are adsorbed onto the glass substrate and a surface blocker (black) is added to minimize microtubules from sticking to the surface. Microtubules (red) are bound to the motors. As motors walk toward the plus-end of the microtubule, microtubules are propelled forward, minus-end in front.

Motility assays are a model to study molecular motor transport because the substrate that the motors are bound to acts as a cargo that contains multiple motors as they walk along the microtubule filament. One of the benefits of using this model to study transport is fluorescent microtubules can be visualized using fluorescence microscopy allowing this to be an easily accessible system to study. In addition, the simplicity of motility assays allows for adding microtubule-associated proteins to investigate their roles in microtubule organization. For example, introducing MAP-65, a microtubule-associated protein from plants that crosslinks microtubules that are antiparallel, in gliding microtubules induces bundling and curled bundles[48]. Interestingly, when microtubules were pre-bundled with MAP-65 before binding to kinesin motors, the kinesin motors are able to pull apart the bundles forming patterns similar to structures seen in cells[48,49]. Varying the concentration of crosslinker and microtubules changes whether there are contractile or extensile dynamics when the kinesin motors pull on the bundles[49].

Propelled microtubules can also form high-order structures such as bundles and spools[50–54]. Hess *et al.*[50] enhanced lateral interactions between gliding microtubules and observed formation of linear and circular structures. The group used biotin tubulin to polymerize microtubules and included streptavidin into the motility assay. The biotin-streptavidin interaction induces lateral binding of microtubules. Gliding microtubules travelling in the same direction will stick together and form a bundle and continue moving in the same direction. If the bundle forms a kink as it's continued to propel forward, the bundle can bend and stick on itself forming a circular rotating structure, or spool[50]. Fig. 2.7 shows the progression of spool formation over time.

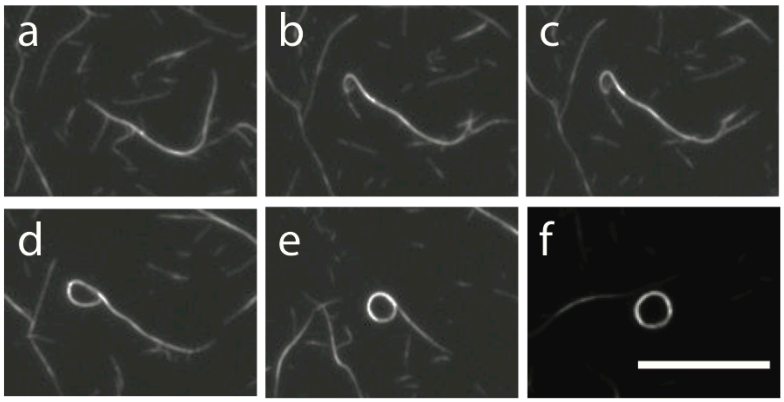

Fig. 2.7) Fluorescence images of spool formation over time. a) A microtubule bundle gliding forward until b) the front of the bundle forms a kink as the rest of the bundle is propelled forward. c) As the rest of the filament moves forward, the bundle bends and d) sticks on itself. e) The bundle spools into a rotating structure and continues to rotate. f) the final spool remains in a stable circular structure. Scale bar, 36 μm.

There are a few proposed mechanisms for spool formation: twist-bend coupling, simultaneous sticking, and pinning at defect[51,55]. Twist-bend coupling refers to spools emerging because of the intrinsic twist in the microtubule structure. As kinesin walk along the microtubule helical structure, the filament will twist, giving rise to a rotation in the microtubule trajectory. Simultaneous sticking occurs when three or more microtubules collide at an intersection where the filaments are traveling in a rotary-like orientation and stick together. Finally, pinning at defect occurs when a microtubule bundle encounters an inactive motor and the head gets pinned. As the rest of the bundle translocate in its current path, the bundle will eventually buckle and stick onto itself forming the initial loop. As the bundle continues to push forward, it is wrapped up into the spool[51].

These spools are an example of a biological actuator converting chemical energy, as kinesin motors hydrolyze ATP, into mechanical work, rotating spools. Based on the average spool diameter of 2.3 μm and microtubule persistence length of 5.2mm[34], the bending energy required to form these spools is about 30,000 kT[50]. These microtubule spools cannot be formed via thermal fluctuations, but rather require the force from kinesin motors actively propelling the filaments.

In the absence of biotin and streptavidin, microtubules were observed to form circular structures when gliding at high density[56]. Lui *et al.*[53] observed an increase in number of microtubule loops in high density motility assays. These microtubule loops are different from spools because there are no crosslinkers enhancing lateral interactions and the loops are formed by single-microtubule filaments. Additionally, the loops they observe are significantly smaller with an average loop radius of 1 μm. These microtubule loops formed at the intersections of surrounding microtubules moving in opposite directions. The trapped microtubule in the center was forced into a rotating loop[56].

Motility assays proved to be an excellent tool for studying *in vitro* assemblies in simplistic systems. Reducing the system down to a few components allows for investigating the role of proteins during transport. In addition, gliding microtubules have

shown to organize into higher-order structures such as large bundles, spools, and loops. The tunability of this experiment makes it a versatile system to study roles of proteins for transport as well as collective motion and assemblies.

2.3 Active Nematics

The term "active nematics" refers to materials that have some orientational alignment reminiscent of the phases that occur in passive liquid crystals. The major difference between the materials I discuss here, and passive liquid crystals is that the active materials are driven. They form a steady-state, non-equilibrium system, whereas passive liquid crystals are an equilibrium phase of matter. Despite this major difference, there are still similar attributes in the active nematic system that are defining features in passive liquid crystals. The following section will discuss passive liquid crystals, depletion forces, velocity-velocity correlation, and prior work on microtubule/kinesin based active nematics.

2.3.1 Liquid Crystals

A liquid crystal is a state of matter which has properties of both a liquid and a crystal. In this state of matter, the molecules flow freely, like a liquid, but have also have orientational order. There are various phases of liquid crystals that are determined by the organization of the molecules.

Two main classifications of liquid crystals include thermotropic and lyotropic liquid crystals. Thermotropic liquid crystal phases form when a material is heated or cooled. Lyotropic liquid crystal phases form by varying the concentration of a material in a solvent. Lyotropic liquid crystal phases are often found in biology, such as lipid membranes. Lipid molecules can arrange themselves in various configurations, such as micelles or bilayers, depending on their concentration in water. Commonly, the molecules in fluid-like materials, such as liquid crystals will collectively move and rearrange in response to an external influence until they have reached equilibrium.

A simple phase observed in thermotropic liquid crystals is the nematic phase. In the isotropic phase (more commonly known as a standard liquid), rod-like molecules will have random orientations, independent from one another. When this material transitions into the nematic phase, the rod-like molecules on average locally align parallel to a direction specified by the director, **n**, as shown in Fig. 2.8. In the nematic phase, the director vector **n** and –**n**, represent the same physical state, since the molecules are not polar. In the nematic phase, the molecules have no positional order, but on average have short-range directional ordering. Though the molecules are on average oriented with **n**, there is still variation in molecular tilt with respect to **n**. This variation is described by the order parameter, S, given by

$$S = \frac{1}{2} < 3cos^2\theta - 1 >$$

where θ is the angle between a molecule's long axis and **n**, shown in Fig. 2.8. The order parameter describes the degree of ordering in the material. For a perfectly ordered state, where all molecules are aligned, S=1, and for a phase with no alignment, S=0.

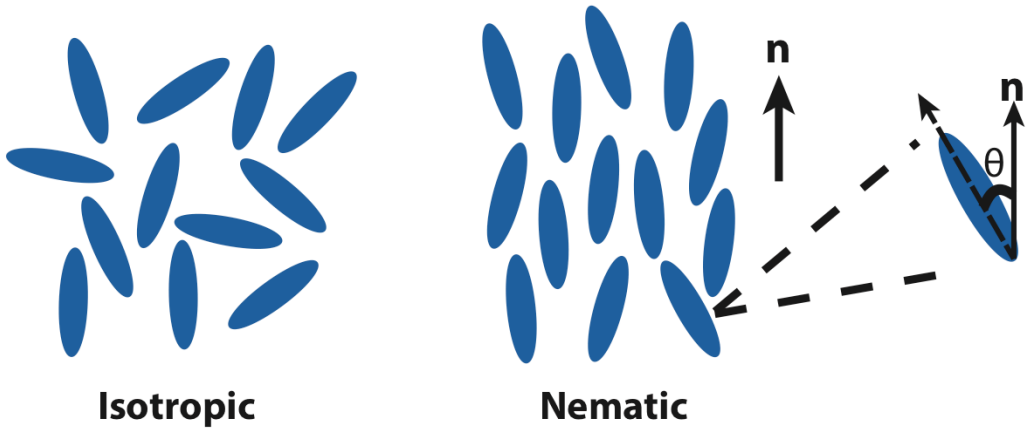

Fig. 2.8) Schematic of molecules in the isotropic phase and nematic phase. In the nematic phase, the molecules on average align with the director, **n**. θ is the angle between the molecule's long axis and **n**.

Liquid crystal phase can have topological defects, which are singularities in the local molecular alignment. These defects are located where there is a distortion in the director field of the material. For example, when you try to lay rods on the surface of a sphere, there will be two points where the rods cannot align, which are the two defect points. Similarly, a topological defect can be found on the top of people's heads where the hair lays radially relative its neighbors. Fig. 2.9 shows an example of a natural topological defect found at the top of a head at the point where the hair alignment is ill-defined. Topological defects are characterized by a charge that is determined by measuring the change in ϕ that the director makes at the distortion[33,57]. To find the change in ϕ, a circle is drawn around the defect, shown in Fig. 2.10, and find the change in ϕ going counterclockwise around the circle[33,57]p. The defect charge, q, is defined as

$$\oint d\varphi = 2\pi\, q_{enclosed}$$

The net change in direction of the director gives the defect charge. Fig. 2.10 a-b) represent q=+1, and Fig. 2.10 c-d) represent q= + ½ and q= - ½ respectively.

Fig. 2.9) Example of a topological defect in hair where all neighboring hairs lay radial to a point. (Dome courtesy of Austin Barnes)

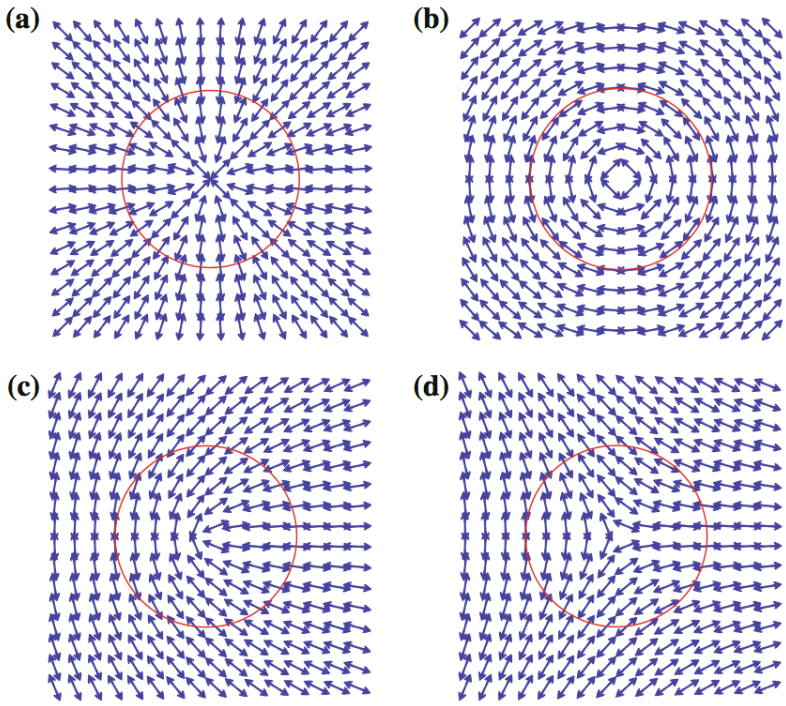

Fig. 2.10) Topological defects for the nematic phase (a,b) charge q=1, (b) q=+ ½ (c) q= -½. (reproduced from Selinger, 2016 with permission ©2016 Springer International Publishing).

Liquid crystal molecules can reorient under the application of external forces. For example, a surface inserted into the liquid crystal may act to impose a local anchoring condition, where the molecules are forced to orient a certain way. Liquid crystal displays are designed using a mixture of liquid crystal compounds that can be aligned and reorient using an electric field. When the liquid crystal molecules reorient, they will exhibit a "on" or "off" state corresponding to a dark or light[1]. Another way liquid crystal molecules can be deformed is to introduce colloidal particles. Introducing colloidal particles, like gold nanoparticles or quantum dots, distorts the liquid crystal which costs energy[58]. To minimize the energy strain, the colloidal particles cluster together.

Any distortion to the order in the liquid crystal results in an energy cost to the system. When the external forces are removed, the material relaxes back to its equilibrium state. Possible deformations to the orientation can be classified by bend, splay, and twist. Fredrick Charles Frank extended energy associated with elastic deformations to liquid crystal medium deformations. In Frank's theory, he defines the free energy, *F*, associated with deformations in a liquid crystal medium as,

$$F = \frac{1}{2}K_1(\nabla \cdot \hat{n})^2 + \frac{1}{2}K_2(\hat{n} \cdot \nabla \times \hat{n})^2 + \frac{1}{2}K_3(\hat{n} \times \nabla \times \hat{n})^2$$

where $\hat{n}$, is the normalized director of the molecule, K_1, K_2, and K_3 are the Frank elastic constants that correspond to the splay, twist, and bend deformations respectively[33,57]. In two-dimensional systems, only splay and bend deformations are present. These distortions in the director field lead to long-range interactions between topological defects. Defects of like charge repel, and defects of opposite charge attract and annihilate.

A common characteristic of emergent patterns in active matter is the individual particles in the ensemble have orientational order. Anisotropic self-propelled particles can lead to orientational ordering when the particles collectively move. Anisotropy implies that the material has directionally dependent properties. A common example of these orientational ordered states in thermal equilibrium is the nematic liquid crystal phase. Here, the liquid crystal molecules align with each other in response to an external stimulus, such as temperature change or an electric field. In the case of active matter, there is similar alignment and organization in the case of bird flocks, schools of fish and bacterial suspensions that arise without external stimulus.

2.3.2 Depletion Forces

The depletion force is an effective attractive force between large colloidal particles in a solution of depletants. Depletants are particles of intermediate size between the size of the large colloidal particles and the smaller molecules that makeup the solution. Polyethylene glycol (PEG) is a polymer that can be used as a depletant in *in vitro* experiments to induce microtubule bundling. Since PEG is a polymer chain, when put in solution, the polymer chain coils on itself. One way to characterize the size of the coiled-up polymer chain is by the radius of gyration, R_g, defined as

$$R_g{}^2 = \frac{1}{N}\sum_{i=1}^{N} < |r_i - r_c|^2 >$$

where r_c is the position vector to the center of mass of the polymer coil, r_i is the position to the ith segment out of a total of N segments of the polymer chain.

The various particles in the solution experience Brownian motion, or random motion, from constant particle collisions stemming from thermal fluctuations in the system. When the large colloidal particles are well spaced apart, the forces from the small particle collisions is isotropic. Once the large colloidal particles are close enough together such that the distance between them is smaller than the R_g of the depletant, there is an increase in the forces from the depletants on the outside of the large colloidal particles further forcing them together as shown in Fig. 2.11. Depletants are often included in *in vitro* active matter assays with cytoskeletal filaments to induce bundling.

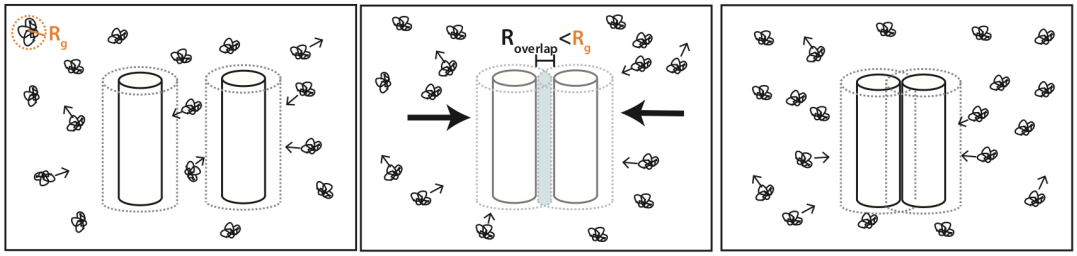

Fig. 2.11) Schematic of cylindrical particles in a suspension with depletants. When the overlap radius of two cylindrical particles becomes smaller than the radius of gyration, R_g, the depletants will have an effective force pushing the cylinders together, forcing them to bundle.

2.3.3 Microtubule/kinesin based active nematic

An active network self-assembled from microtubules and kinesin motors exhibit unique extensile dynamics the generates fluid flows. This system drawn much attention and interest in the past few years. Zvonimir Dogic and his group extended on the system described by Nédélec *et al.*[5] and created an active extensile network made of microtubules and kinesin. The active network requires three main components, biotin-kinesin motors, microtubules, and a depletion agent as shown in Fig. 2.12 Biotin tagged kinesin motors are clustered together in the presence of streptavidin. GMPCPP microtubules are ideal for the active network because of their short length and rigidity. Longer microtubules tend to create more elastic gels that are not suitable for maintaining a nonequilibrium state[59,60]. Polyethylene glycol (PEG) is introduced to the network to force the microtubules closer together into bundles through depletion forces. When the microtubules are in close proximity, to each other the kinesin motor clusters can crosslink the bundles together. In the presence of an energy source (ATP), the kinesin motors start to walk along the microtubule bundles and naturally sort by polarity of the microtubules. The oppositely polarized bundles will extend away from each other, thus forming the active network. In

the active network, microtubule bundles are constantly extending, bending, fracturing, and recombining with neighboring bundles as shown in Fig. 2.13.

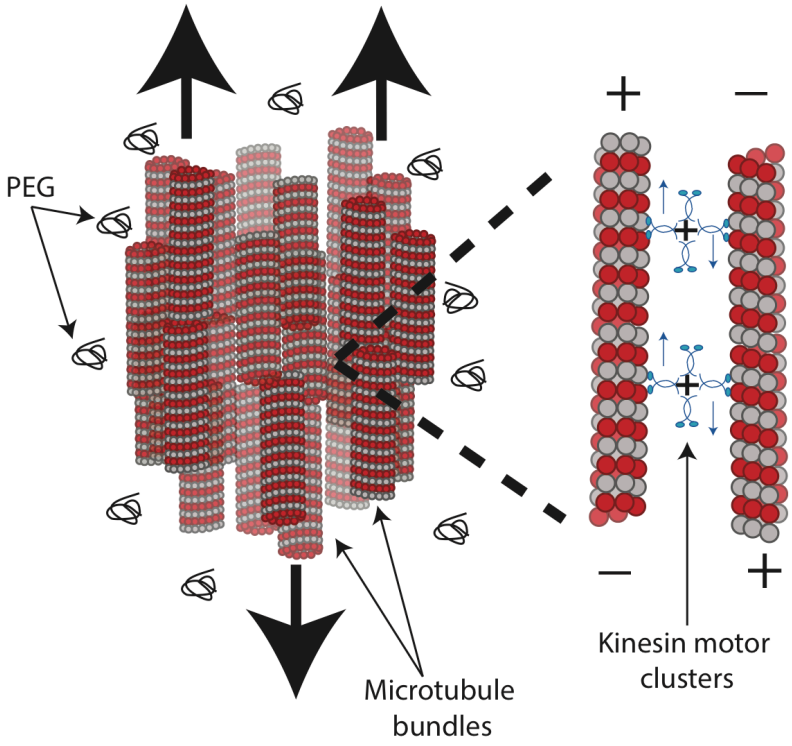

Fig. 2.12) Schematic of microtubule/kinesin active network. Depletion forces from PEG force microtubules to bundle together. Kinesin motor clusters crosslink microtubule bundles together. When kinesin motors walk along oppositely polarized bundles, the microtubules extend away from each other.

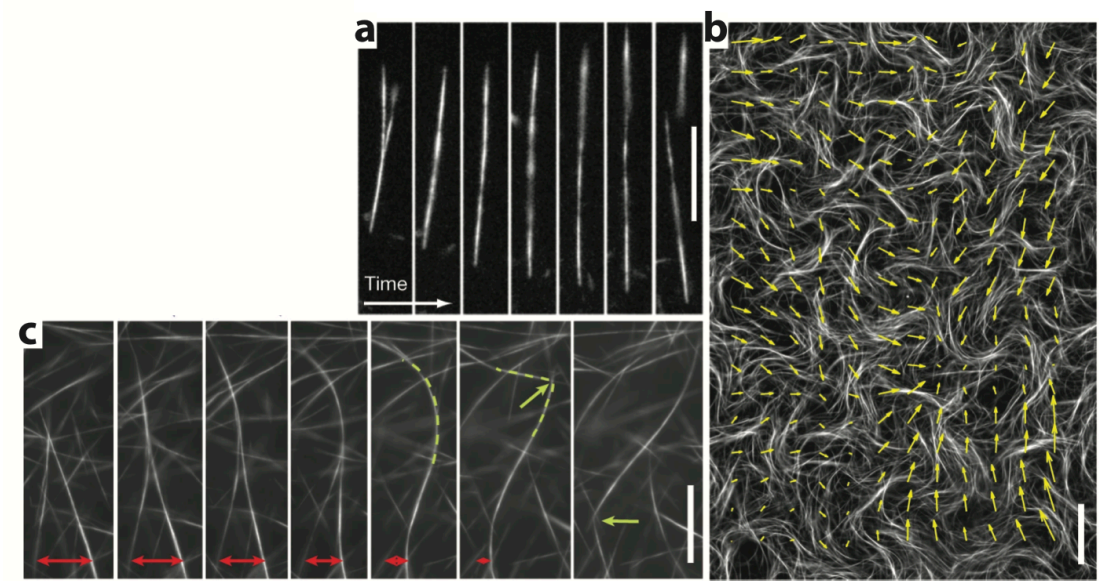

Fig. 2.13) Extensile behavior in a microtubule-kinesin based active network. a) Two microtubule bundles come together and extend, eventually fracturing into two separate bundles. Time interval, 5 s. Scale bar, 15μm. b) The percolating network viewed at large-scale. The yellow arrows indicate the local bundle velocity direction. Scale bar, 80 μm. c) An example of local bundles merging together, extending, bending (green dashed line), fracturing (green arrow), and recombing leading to a highly dynamic network. Time interval, 11.5 s. Scale bar, 15 μm. (Adapted from Sanchez, 2012 with permission ©2012 Springer Nature)

What's unique about this system is when the active network is confined in 2D at an oil/water interface, ±1/2 topological defects spontaneously emerge as shown in Fig. 2.14. Not only do these defects annihilate each other, like in passive liquid crystals, but also, they can also be created where pairs of defects spontaneously emerge and stretch away from each other. This two-dimensional network of active defects creates self-generating flows[4]. The hydrodynamics of these flow fields are complex and have shown similarities to characteristics of turbulent flows[16,61,62]. This new material with self-generating flows opened up a whole avenue of questions to be studied, ranging from how to control the defect dynamics to understanding the underlying physics of these generated flows.

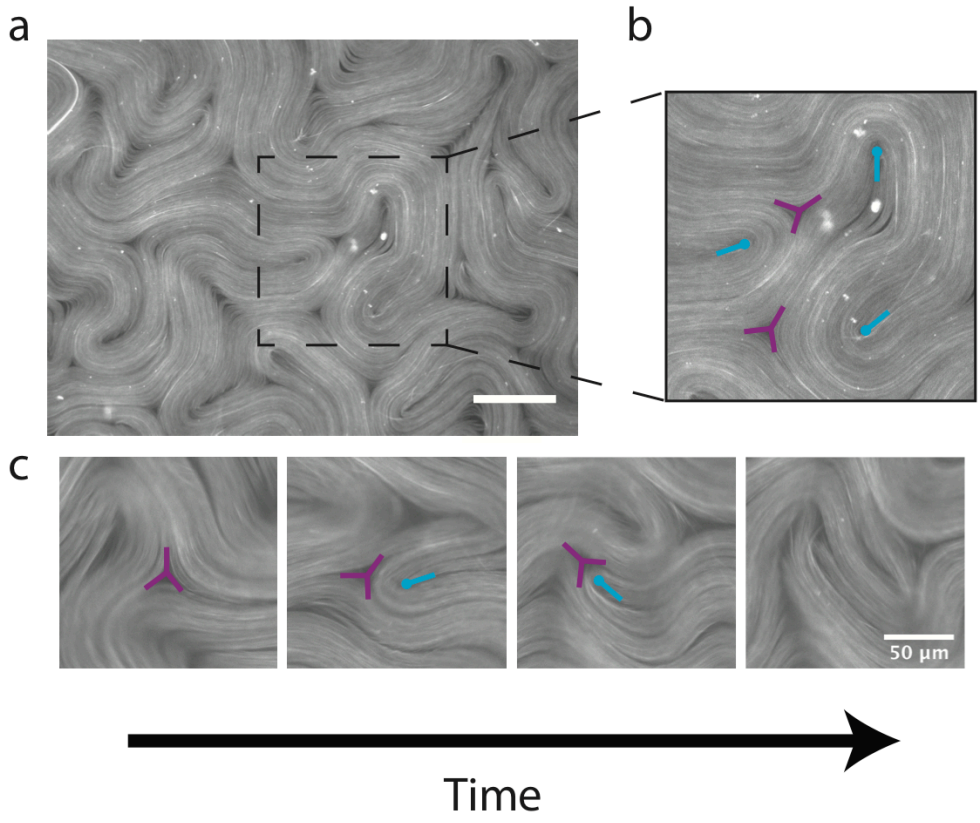

Fig. 2.14) 2D active microtubule fluid with emerging ±1/2 topological defects. a) Fluorescence microscope image of the microtubule network when confined in 2D. Scale bar, 100 µm. b) Close-up of +1/2 defects (blue) and -1/2 defects (purple) that emerge when the network is in 2D. c) Time-lapse of active defects of opposite charge annihilating over time. Scale bar, 50 µm.

In 2D, the flows are driven by the active topological defects. Controlling the defect dynamics is an interesting direction to study this system. Controlling the defect dynamics and flows generated by the system could potentially provide insight to further applications for this unique material. Two potential ways of controlling the dynamics would be to use geometric constraints and tune the internal parameters of the active network.

Collective motion can be controlled by constraining systems to boundaries of various geometries. Asymmetric ratchet gears have been able to create persistent rotation in bacterial baths[63]. This behavior is evidence for how geometric constraints can influence collective behavior. The microtubule/kinesin based active nematic has been studied in confinements such as microchannels of varying width[19,64], circular wells[65], spherical droplet[4,66,67], and toroidal droplets[68]. In this review, I will focus on two examples in which an active nematic is confined to a flat surface (microchannels and wells).

When confined to microchannels, there are three observed flow states, 1) a quasi-stable shear flow, 2) quasi-stable vortex lattice, and 3) an unconfined chaotic state, shown in Fig. 2.15. Theory predicts that in the intermediate state, pairs of active +1/2 defects form

a quasi-stable vortex lattice and braid round each other as they process through the channel[19]. Given its similarity to a traditional Gaelic dance, this phenomenon was named dancing disclinations, or Ceilidh dynamics[19]. Experimentally, the vortex lattice is shown to be transient and undergo an instability where the +1/2 defects will occasionally annihilate with their -1/2 counterpart[64]. Additionally, under even smaller confinement in width, a quasi-stable shear flow state was observed. In the shear flow state, microtubules move passed each other in a smooth way. Unlike the stable laminar flow predicted by simulations[19], in experiment, the shear flow state would undergo an instability where a +1/2 defect emerged and processed across the channel[64].

Similar defect dynamics were observed when the active nematic was confined to circular wells with decreasing size, shown in Fig. 2.16. At intermediate confinement (200μm-400μm), pairs of +1/2 defects exhibited doubly-periodic dynamics where the two defects would rotate within the confinement until one of the defects annihilated with a -1/2 defect at the boundary, and two new +1/2 defects emerged[65]. In both the channel and disk confinement, the defect dynamics are well-controlled with some system instability.

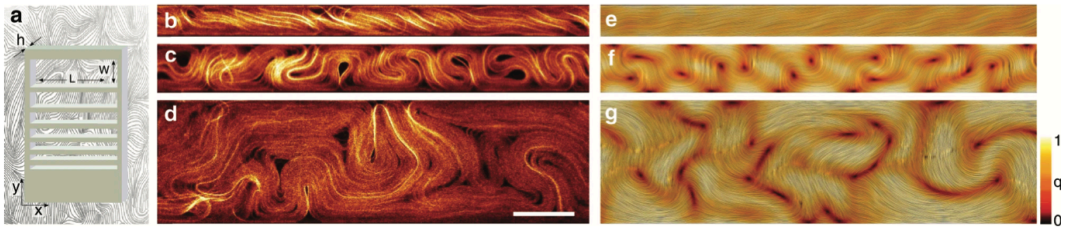

Fig. 2.15) 2D active nematic confinement in microchannels. a) Schematic of the experimental setup where a polymer plate with rectangular openings positioned at the interface between the active fluid and silicon oil, thus confining the active nematic into the channels. b-d) Confocal fluorescence images of the active fluid confined in varying widths channels. e-g) Corresponding simulations of the experimental system. Shown is the director field tangents produced from the Line Integral Convolution of the director field. In strongly confined channels, the active fluid forms quasi-stable laminar flows where the instability causes defect creation at the boundary. Intermediate confinement results in a "dancing" state where +1/2 defects behave as they are travelling along the channel in opposite directions passing each other in a sinusoidal-like pattern. This dancing state again is not as stable as predicted by simulations. In the widest channels, defects resumed chaotic behavior where defect creation and annihilation occur both in the bulk and at the boundaries. (reproduced from Hardoüin et al, 2019 with permission ©2019 Springer Nature)

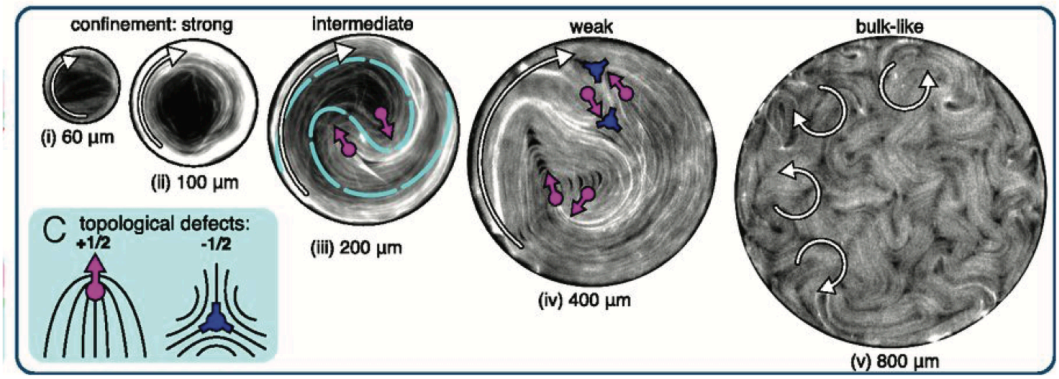

Fig. 2.16) 2D active nematic confined in wells of increasing diameters. There are three confinement regimes: strong, intermediate and weak. Under strong confinement, the diameter of the well is comparable to the defect core size. Microtubules accumulate along the boundary, leaving a void in the center. Microtubules found in the center would be rigid and rotate with respect to the boundary. Under weak confinement, ±1/2 defects nucleated and annihilate both at the boundaries and in the center. The dynamics are representative of those observed under no confinement. Under intermediate confinement, the system exhibited persistent circular flows in the well with interesting defect dynamics. Two +1/2 defects show doubly periodic dynamics where two +1/2 defects will wind around each other until the configuration is almost circular. At this point, the system buckles, and new defects are nucleated at the boundary. (Adapted from Opathalage, A., 2019 with permission)

Interestingly, similar defect dynamics were observed where the active nematic was patterned over a liquid crystal substrate[69]. In this experimental setup, the active nematic did not have physical boundaries. Instead, the defects exhibited patterning based on the underlying substrate. In this experiment, they use 8CB, a Smectic-A liquid crystal, to create polydisperse domains to pattern the surface for the active nematic. In the Smectic phase, liquid crystal molecules are positionally ordered in one direction in a layered structure[33]. Topological defects can be trapped in these domains and rotate around similar to those seen in active nematics confined to a circular well. However, the number of topological defects trapped in the domain ranged from two, three, and four +1/2 defects. Three +1/2 defects rotating in the domain was accompanied by a -1/2 defect, and four +1/2 defects was accompanied by a +1/2 defect in the center. In all cases, the total charge of +1 remained[69]. This work showed that using patterned substrates can be an alternative way to control the defect dynamics in the active nematic.

Using geometric constraints is an external way to control the defect dynamics; however, changing the parameters that form the network is a way to alter the network dynamics internally. Henkin *et al*.[59] did a comprehensive study on the underlying factors in creating the 3D active network, or active gel. Parameters they tuned in this study include ATP concentration, microtubule concentration, kinesin/streptavidin concentration and PEG concentration[59]. The group quantified the dynamics of the flows generated by the 3D active network by using tracer beads.

Tuning ATP concentration, Henkin *et al*.[59] found that the average network speed, defined as the average distance beads traveled over 10 seconds, increased monotonically

until it reached saturation. Interestingly, the max network velocity measured here was about 2 μm/s, which is significantly faster than the 0.8μm/s velocity typical for single kinesin motors. This could be attributed to the velocities adding up for multiple bundles extending from each other. They also observed similar trends for measuring the flow length scale with increasing ATP. The flow length scale was measured by measuring the decay of the velocity-velocity correlation function.

When tuning the kinesin motor concentration, Henkin *et al*.[59] found an optimal motor concentration that maximized dynamics. At low motor concentrations, the likelihood of clusters crosslinking neighboring microtubule bundles and inducing a sliding motion is low, therefore, leading to slower dynamics. If the concentration of motors is too high, there may be too many motors bound to microtubules at a time, leading to traffic jams and a slow-down in the network dynamics[70,71]. Altering the microtubule concentration in the network gave similar results in network activity as that observed for changing motor concentration. The notable finding here is there is an optimal microtubule/kinesin concentration ratio that leads to optimal network dynamics.

The final parameter the group altered was the concentration of depletants (PEG concentration). PEG assists in forcing microtubules into bundles through depletion forces. Below 0.6% (w/w%), depletion interactions were not strong enough to force the filaments together, so the system remained isotropic and nonactive. The microtubules quickly transitioned to a highly dynamic network when PEG concentration was increased to 0.8%. Increasing the PEG concentration past 4.4% slowed the average velocity of the network significantly. Increasing the PEG concentration increases the depletion forces experienced by the microtubules, which is analogous to increasing the friction between microtubule bundles. This increase in friction can explain the decrease in activity since the motors are working against a larger load. Overall, this comprehensive investigation showed that the parameters in the microtubule/kinesin active gel are highly tunable. Tuning various parameters in this system allows for detailed investigations of factors driving the generated flows and characterization of the dynamics.

2.3.4 Active Length Scale

Active nematics are described by characteristic length-scales present in the system. Two important length scales that are inherent to active nematics are the coherence length of the nematic phase, $l_s = \sqrt{\frac{K}{C}}$, and the active length-scale $l_a = \sqrt{\frac{K}{|\alpha|}}$. Here, K is related to the elastic constant, C is a material constant, and α is related to the activity in the system. The coherence length-scale dictates how quickly the nematic order drops off in the neighborhood of a topological defect and can be used as a measure of the defect core radius. The active length-scale is the length at which the elastic stresses and active stresses balance in the system[16]. The elastic and active stresses give rise to spontaneous elastic distortions and flows in the system.

Hemingway *et al.* describes several ways to measure the active length scale: 1) mean defect separation, 2) director correlation length, 3) Vorticity correlation length, and 4) velocity correlation length[62]. Correlation functions are used to quantify the spatial

structure of a system by measuring how microscopic variables at all respective locations relative to an initial point are related. Hemingway *et al.* performed an extensive numerical study and found that the length-scales calculated from each respective method scale as $1/|\alpha|^{1/2}$ [62]. The active length-scale is the length scale that controls the onset of instability in the active fluid, and since the correlation lengths described above scale with this active length-scale, then it is a helpful method to quantify the spatial structure of the system. Other groups have used vorticity correlation length to quantify the active length-scale in the context of characterizing turbulent flow[16,61]; however, for the purpose of this research, I will focus on velocity correlation lengths.

The velocity-velocity correlation is defined as follows

$$C(r) = \sum_{i,j} \hat{v}_i \cdot \hat{v}_j \delta(r - r_{ij})$$

where $\hat{v}$ is the normalized velocity vector of the ith and jth particle, r is the position vector to the ith and jth particle. The active length is defined as, $l_a = r$, where $C(r) = 1/2$ following the definition from Hemingway *et al.*[62] The velocity-velocity correlation measures how closely related the velocity at two points, i and j, are. If the velocities are the same at the two points, $C(r) = 1$, if the two velocities are perpendicular to each other, $C(r) = 0$, and if the two velocity vectors are oriented antiparallel, then $C(r) = -1$.

2.4 Fluid mixing and braiding

Fluid dynamics is a field of study that describes fluid flows. This field has a wide range of applications including understanding evolution of stars, ocean currents, weather patterns, and blood circulation. There are various types of fluid flows, all with complex dynamics, namely laminar, turbulent and chaotic flows. Laminar flows are characterized by fluid materials following a smooth path in layers, where no mixing occurs. Turbulent flows, on the other end, are characterized by an excess of kinetic energy in parts of the fluid flow that overcomes the damping effects from the fluid viscosity and causes energy cascades from large scales of motion to smaller scales of motion. Turbulent flows exhibit high levels of mixing and the onset of interacting vortices with a distribution in sizes. Chaotic flows are characterized by complex fluid material trajectories, where neighboring fluid material will separate exponentially with time. One important subfield of fluid dynamics is studying mixing dynamics of a fluid. Turbulent and chaotic flows have the required conditions to instill efficient mixing. In this section I will focus on quantities of chaos theory that describe mixing.

2.4.1 Mixing

Fluid mixing is a complex phenomenon that is applicable to a wide range of fields from ocean mixing from currents to mixing dough for pastries. The goal of achieving a well-mixed system is to minimize the time it takes to reach a homogenous system from an

initial inhomogeneous state. The main mechanisms responsible for mixing in fluids are diffusion and advection. In many cases, diffusion occurs too slowly in liquids for efficient mixing, so advection is needed for efficient mixing.

Advection refers to the transport of matter by a fluid flow. In chaotic advection, the flow generates complex patterns from an initial simple state. The term chaotic advection was first introduced by Hassan Aref in 1984 when he proposed a regime of advective motion that falls between laminar flow and turbulence[72]. Chaotic advection generates small scale structures based on the material stretching and folding generated by the chaotic flows[73]. Flows that are chaotic are highly sensitive to initial conditions[74]. Chaotic advection is characterized by fluid material that quickly diverges in the flow. If a flow is chaotic, nearby trajectories will separate exponentially in time.

The Lyapunov exponent is a quantity in chaos theory that characterizes the rate of separation of infinitesimally close trajectories and is given by

$$|\delta r(t)| \approx e^{\lambda t}|\delta r_0|$$

where δr_0 is the initial separation rate between trajectories, and λ is the Lyapunov exponent[75]. The maximal Lyapunov exponent is defined as

$$\lambda = \lim_{t\to\infty} \lim_{\delta r(0)\to 0} \frac{1}{t} \ln\left(\frac{\delta r(t)}{\delta r(0)}\right)$$

A positive Lyapunov exponent indicates the growth of the material lines is exponential.

Chaotic advection can be well visualized in the example where paint is actively stirred. When paints are mixed together, as the fluid is stirred, the paint is exponentially stretched and folded until it is well-mixed and uniform. The more stretching and folding in the material when stirred, the more efficiently mixed the system becomes. When a system is actively stirred, either with rods or through external forces, the stirring protocol becomes crucial in determining whether the resulting flow will be chaotic[76,77].

Topological entropy is a non-negative quantity used as a measure of mixing efficiency in a system[78]. Topological entropy is defined as the minimum stretching rate rod motions imparts on the material lines in a flow. During active mixing, adjacent rods in the system exchange positions to stretch the material lines. As the rods exchange position, the material becomes more stretched and folded. For every exchange, a finite amount of topological entropy is imparted into the system. A positive topological entropy indicates exponential stretching, and the magnitude indicates the level of stretching.

The stirring protocol followed by the rods is crucial in determining the final state of the system. Fig. 2.17 shows experimental results from Boyland *et al*.[77] that compares fluid mixing of two stirring protocols. In Fig.2.17a the first iteration is a clockwise exchange between the first two rods, whereas in Fig. 2.17b, the first iteration is a counterclockwise exchange between the first two rods. Comparing the successive iterations and final state, it is evident that the stirring protocol shown in Fig. 2.17a, is not as effective as the stirring protocol shown in Fig. 2.17b. The well-stretched and folded dye-lines in Fig. 2.17b are characteristics of a well-mixed system.

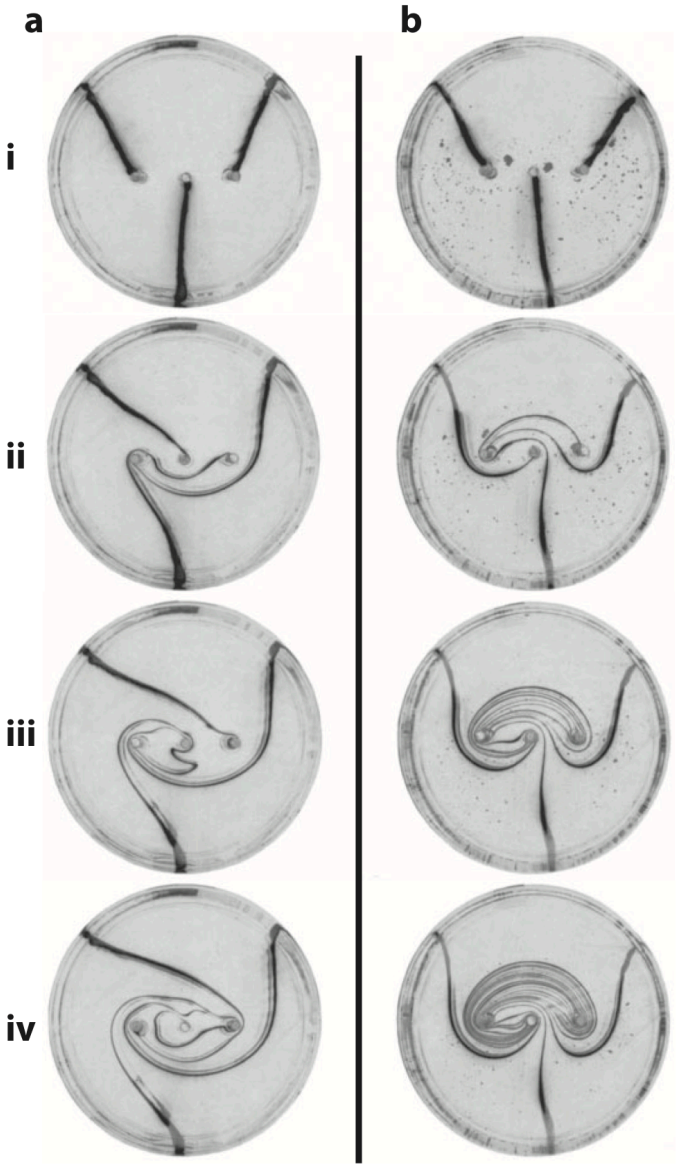

Fig. 2.17) Two examples of three-rod stirring system mixing glycerol with dye. The two columns show two different stirring protocols. (i-iv) indicate each iteration of rod exchanges. The stirring protocol in (a) results in a poorly mixed system where the dye lines are not well stretched, whereas the stirring protocol in (b) results in a well-stretched, well-mixed system. (Adapted from Boyland, 2000 with permission ©2000 Cambridge University Press)

2.4.2 Braiding in Fluid Mixing

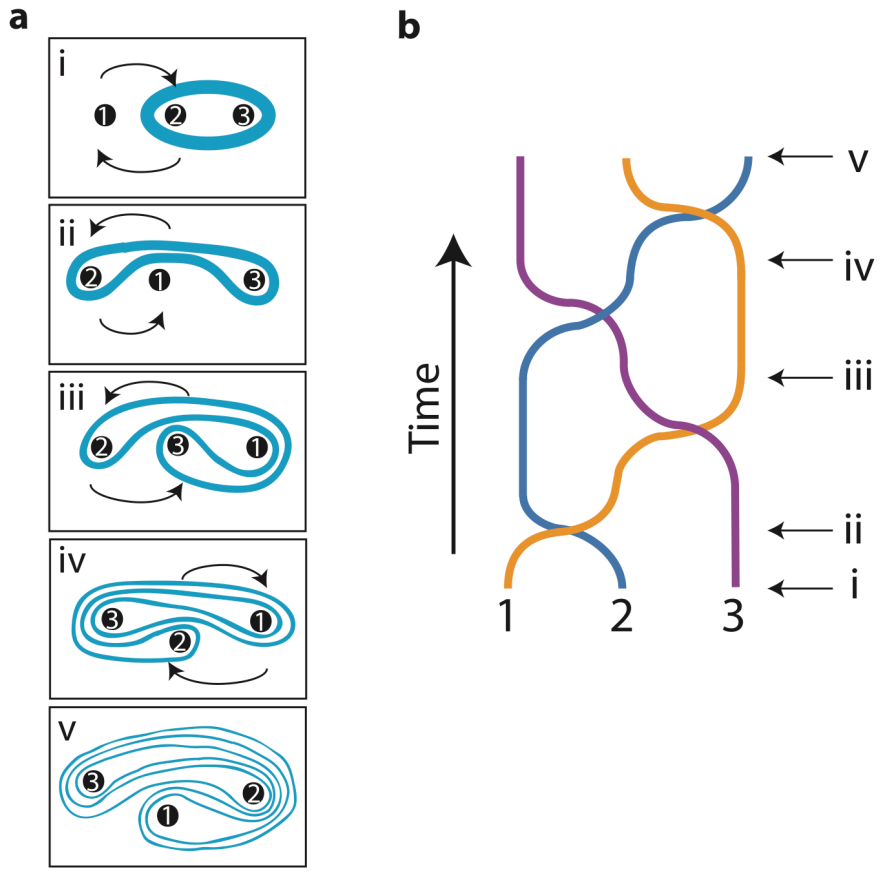

Fig. 2.18) a) Schematic of three rods (1, 2, 3) interchanging positions to pull and mix a fluid. b) corresponding braid diagram to (a). (Adapted from Tan et al. 2019 with permission © Springer Nature)

Jean-Luc Thieffault developed a method to calculate topological entropy, by creating braids[79]. Fig. 2.18a is a schematic representing a three-rod system mixing dye (in blue). To keep track of the rod exchanges, Thieffault developed the concept of braiding, where each strand in a braid represents a rod and for each exchange, the strands exchange position as shown in Fig. 2.18b. The complete motion of the rods can be described as a braid[79]. The braids could then be written as an algebraic expression with the use of generators, which are *(n-1) x (n-1)* matrices in the n-braid group. The Burau representation of generators offers an easy way to calculate the topological entropy[79,80]. In this representation, the generators, σ_i, represents a clockwise interchange of the *i*th rod with the (i+1)th rod in a circular path[80] and *i* is the position of the rod counting from left to right, shown in Fig. 2.19. In a three-rod system, the generators are represented by 2x2 matrices with

$$[\sigma_1] = \begin{pmatrix} 1 & 0 \\ -1 & 1 \end{pmatrix}, \; [\sigma_2] = \begin{pmatrix} 1 & 1 \\ 0 & 1 \end{pmatrix}$$

where σ_1 represents a clockwise exchange using the rod in the first position counting from left to right, and σ_2 represents a clockwise exchange using the rod in the second position counting from left to right.

The generators for counterclockwise exchange, σ_i^{-1} are found by inverting the matrices above. A sequence of rod exchanges can therefore be rewritten in terms of the generators. The largest eigenvalue from the sequence of generators gives the spectral radius. The topological entropy can be calculated by taking the log (spectral radius). If the stretching rate for the material is exponential, then the interface between the two solutes is becoming more convoluted with time which implies good mixing[79]. For a three-rod system, the optimal braiding pattern is referred to as the "golden braid", which is described by an initial clockwise exchange between the first two rods, followed by a counterclockwise exchange between the third and first rod[81]. This braiding is the same set of motions for braiding hair. Repeating this motion generates the optimal mixing pattern.

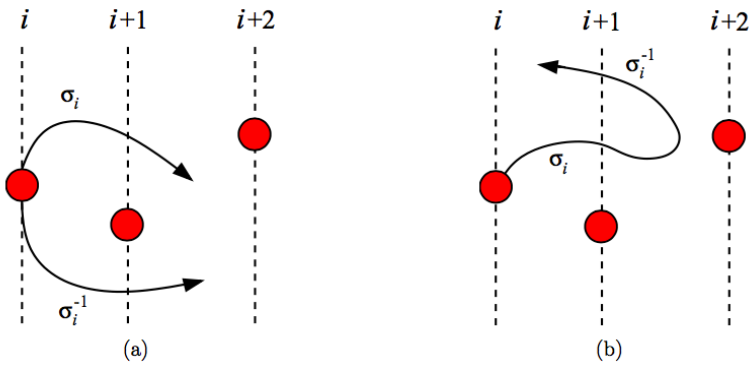

Fig. 2.19) Example of three rods in a mixing system. The dotted lines represent projection lines corresponding to each rod. (a) Generators σ_i represent a clockwise interchange with the adjacent rod, and σ_i^{-1}represents a counter-clockwise interchange. (b) When a rod crosses the adjacent rod and returns to its initial position, the net interchange is 0. (Thieffault, 2014)

The topological entropy for trajectory data can be calculated using braiding method. The trajectories of a fluid flow can be tracked by incorporating tracer particles embedded in the fluid. The tracer particles can serve as rods and a braid can form as they exchange position with neighboring tracers. A topological entropy can be calculated from the resulting braid. This method is an important contribution to characterizing chaos in experimental systems.

One interesting connection that has yet to be explored is to directly tie fluid dynamics to this soft matter system by considering the active network as a fluid itself. Previously, only the hydrodynamic flows generated by the system were considered and the term turbulence has been used to describe the flows. We introduce the concept of chaos and propose that the 2D active nematic may have properties of chaotic advection. Our aim is to directly measure flows within the network by considering the material itself to be a

fluid. We will introduce concepts from chaos theory that will be used to measure the transport properties in the active nematic.

2.5 Summary

In Chapter 2, I have discussed the important background and theory that will be referenced in the rest of this dissertation. This chapter begins with an introduction on the materials we use, specifically microtubules and kinesin motors.

I then discuss prior work done using microtubules and kinesin to study self-assemblies and organization. The microtubules driven by kinesin motors in motility assays can self-assemble into interesting higher-order structures like bundles, loops, and spools. Additionally, motility assays have been used to study the role of microtubules-associated proteins in microtubule organization.

Then, I discuss another microtubule/kinesin based active matter system that has recently gained much traction. The active system is made of a dense concentration of microtubules and kinesin motor clusters that self-assemble into an active network that has extensile dynamics. This active system in 2D has characteristics resembling passive nematic liquid crystals. I discuss a brief overview of liquid crystal theory to provide context to the microtubule/kinesin-based active network.

The active microtubule/kinesin network has unique self-generated flows leading to extensive studies on the fundamental physics driving the flow. A topic of interest is studying these flows under various confinements, which provided insight to how this active fluid can be controlled, and a deeper understanding of the dynamics in the flow. Prior work has shown interest in the generated flows by the active material; however, another perspective would be to consider the active network as a fluid itself. In attempt to directly tie fluid dynamics to soft matter, we propose to treat the microtubule/kinesin-based active network to be an active fluid and quantify its chaotic dynamics using chaos theory. The chapter ends with a brief introduction to concepts in fluid dynamics pertaining to chaos theory.

The main focus of this dissertation is to build upon the prior work done studying microtubule/kinesin-based self-organization at low filament density and collective behavior at high filament density. We explore how the microtubule gliding velocity plays a role in assembling microtubules spools in Chapter 3. Then, we aim to quantify chaotic behavior in the active nematic system, by treating the network as an active fluid and directly apply concepts from chaos theory to fluid in Chapter 4 and 5.

Chapter 3: Understanding the role of transport velocity in bio-motor powered microtubule spool assembly

In this chapter, I discuss the system described in section 2.2.2 where microtubules are propelled by immobilized kinesin motors. In our work, we use biotin and streptavidin to increase the microtubules' "stickiness" so that the interactions between microtubules is enhanced. Using "sticky" microtubules have been observed to form bundles and rotating spool structures. We studied the role of gliding velocity on the initial spool formation rate and spool density as well as at the steady state. This work contributes to understanding fundamental mechanisms of spool formation.

3.1 Introduction

Microtubules propelled by immobilized kinesin motors are a versatile tool used to study microtubule organization. Prior work has shown that microtubules polymerized with tubulin functionalized with biotin can enhance lateral filament interactions during gliding in the presence of streptavidin[50]. Streptavidin has a high binding affinity for biotin, with a dissociation constant on the order of $\sim 10^{-14}$ mol/L. The dissociation constant is an equilibrium constant that measures the tendency of a larger complex to separate reversibly into its component molecules. When neighboring microtubules, decorated with biotin, glide near each other, streptavidin molecules can form a bond with both microtubules, thus promoting microtubule bundling. With this enhanced interaction, gliding microtubules can bend, stick onto itself and form a spool. Spools are circular bundle-like structures that continually rotate in the presence of ATP. These spools are an example of how active microtubules can self-assemble into specific structures that are far from equilibrium. Fig. 3.1 shows an example of spools and bundles formed from biotin functionalized microtubules in the presence of streptavidin. These rotating spools are bio-actuators, turning chemical energy (ATP) into mechanical work (spool rotations). Understanding the factors driving the self-assembly process is an important stepping-stone to constructing similar nanostructures using synthetic materials.

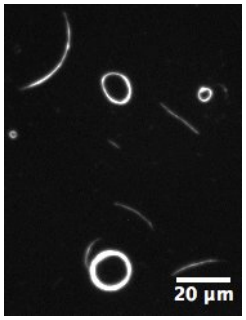

Fig. 3.1) Fluorescence microscope image of gliding biotin-functionalized microtubules forming bundles and circular spools in the presence of streptavidin. Scale bar, 20 µm.

In a recent paper, Kawamura *et al.* explored optimum concentrations of streptavidin, microtubules, and kinesin that will form complexes such as bundles and spools[82]. Tuning the concentration of kinesin motors affects the overall mobility of microtubule filaments. The ratio of the concentration of streptavidin to microtubules of 1 mol/mol with an optimal concentration of microtubules at 48nM resulted in long microtubule bundle formation which is ideal for creating larger micromachines[82].

Another important factor playing into the structure of the spools is the length and rigidity of the microtubules. Since microtubule filaments are quite rigid with persistence lengths that can range from 0.5[32] mm to 5.2mm[50], the spools are capable of storing a large amount of bending energy (ranging from 2500kT[56] to 30,000kT[50]). This energy is dependent on the spool size, persistence length and average length of microtubules. Wada et al.[83] investigated the effects of spool size using GTP microtubules, which are more flexible, and GMPCPP microtubules, which are more rigid. With GTP microtubules, longer filaments resulted in larger spool sizes. An average filament length of ~17µm gave an average spool size of ~8µm[83]. Using GMPCPP microtubules, with an average length of ~10µm, resulted in an average spool size of ~18µm[83]. It is evident that stiffer microtubules play a large role in creating larger spool sizes. Spools can grow in thickness by continuously adding more microtubules after their initial assembly[84].

Probing the kinesin density is an important parameter for understanding the underlying mechanism for spool formation. Lam et al.[51] varied kinesin density and observed high kinesin density formed spools with smaller radius and higher density compared to low kinesin density[51]. There was a larger population of short microtubules in the section of the flow cell with high density of kinesin motors. When there is a high density of kinesin motors, the motors can exert sufficient force on bent microtubules to break them and sustain gliding for the shorter filaments, which can explain the smaller spool sizes[51].

There has been extensive work studying factors that play a role in spool formation and tunable parameters that control characteristics of the spools; however, the role of microtubule gliding velocity on self-assembly still remained unclear. In this Chapter, we vary the microtubule gliding velocity by tuning the ATP concentration and studied how this affects the initial rate of spool formation. Our findings showed gliding velocity plays a role in the initial rate of spool assembly and the initial spool circumference; however, at

the steady state, the velocity no longer plays a role in the spool number or spool circumference.

3.2 Experimental Methods

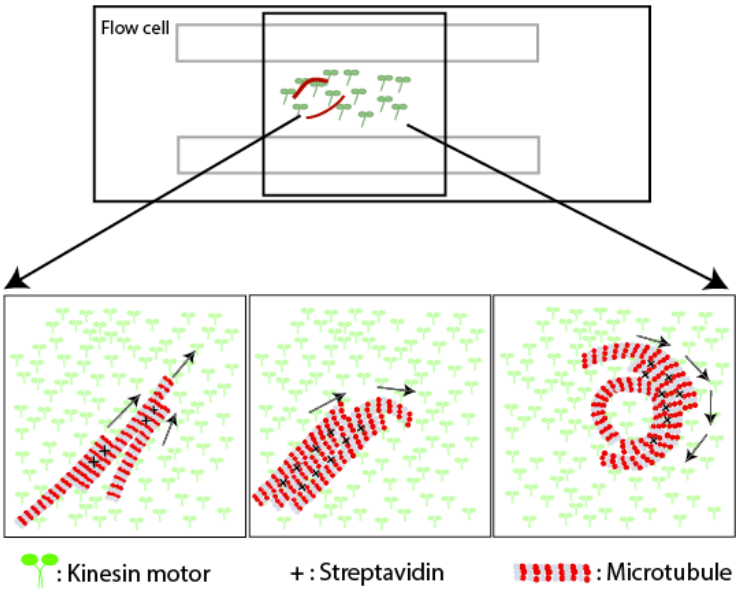

Fig. 3.2) Schematic of flow cell. The kinesin motors coat the surface of the glass slide. The biotin-functionalized microtubules coated with streptavidin bundle together and form spools as they glide on the immobilized kinesin. (reproduced from Tan, A.J, et al. 2016 with permission ©2016 Centre National de la Recherche Scientifique (CNRS) and The Royal Society of Chemistry)

3.2.1 Biotin-labelled microtubule polymerization

Microtubules were labeled with both rhodamine and biotin. The rhodamine labeling allowed us to use fluorescence imaging, and the biotin labeling was necessary to induce the lateral interactions from the biotin-streptavidin bonds between microtubules. These microtubules were prepared by incubating tubulin mix (6:1 biotinylated tubulin to rhodamine-labeled tubulin, 0.47 mg/ml in PEM 80 buffer (80mM PIPES, 1mM ethylene glycol bis(β-aminoethyl ether),1mM $MgSO_4$, pH 6.9)) supplemented with 20μM Taxol and 2mM GTP for 1 hour at 37º C. Microtubules were kept in at room temperature in a dark box and used within four days of preparation.

3.2.2 Flow-cell setup

Microtubule spooling experiments were carried out *in vitro* using standard flow cells and imaged using a fluorescence microscope (Leica DM 2500P) equipped with a

QImaging Retgia Exi camera. Flow cells were constructed by sandwiching a coverslip (22x22 mm^2) and a microscope slide using double-sided tape. Both the coverslip and the microscope slide were biologically clean (via acetone and ethanol washing). The volume of each flow cell was approximately 10 µl.

Kinesin (100 nM in PEM80 buffer supplemented with 20mM Dithiothreitol (DTT)) was incubated in the flow cell for 5 min to allow them to bind to the glass surface. Next, we buffer exchanged the kinesin mix with 5 mg/ml bovine serum albumin (BSA) in PEM80 buffer, supplemented with 20mM DTT and 50 µM Taxol to wash away excess/unbound kinesins as well as blocking the surface that is not covered by kinesin. To buffer exchange, 10 µl of the new solution is flowed in on one end of the flow cell and a piece of filter paper was placed at the opposite end to absorb the current solution in the flow cell. Microtubules (6 biotin : 1 rhodamine, 0.047 mg/mL) were then exchanged into the flow cell and left to incubated for 3 min to allow binding to the kinesin. Excess/unbound microtubules were washed away using an anti-fade solution (20 mM DTT, 8.5 mg mL-1 glucose, 0.28 mg mL-1 glucose oxidase, and 210 mM catalase in PEM80 buffer) supplemented with 8 µM ATP. Streptavidin-FITC conjugate (0.01 mg mL-1 in PEM80 buffer, supplemented with 10µM ATP, 20 µM Taxol and 0.2 mg mL-1 BSA) was exchanged into the flow cell and incubated for 3 minutes. Excess streptavidin-FTIC was washed out with anti-fade solution. Finally, anti-fade solution supplemented with ATP (0-1000 µM as indicated) and an ATP regenerating system (2 mM phosphocreatine, 70 µg mL-1 creatine phosphokinase) was added to the flow cell to initiate kinesin-based microtubule gliding. Unless otherwise indicated, the flow cell was sealed using vacuum grease (Dow Corning high vacuum grease, Dow Corning Corporation, Midland, MI) to prevent solution from drying out.

3.2.3 Image analysis

The sizes of spool images were 658µm x 492µm and 328 µm x 245 µm. Image analysis was carried out using Image Processing and Analysis in Java (ImageJ, http://imagej.nih.gov/ij/). The gliding velocity of microtubules was measured using the MTrackJ plugin for ImageJ. Self-assembly of microtubule spools at each velocity and time point was characterized by the circumference and the number density of spools assembled (73-639 spools and 10-29 images each). The circumference of microtubule spools was determined manually using the circle tool and segmented line tool in ImageJ. The number of microtubule spools in images was counted manually.

3.3 Results

3.3.1 Nonzero velocity necessary for spool formation and rotation

The velocity of kinesin walking on microtubules as a function of ATP is well characterized by Michaelis-Menten kinetics. We first verified the relation of microtubule gliding velocity as a function of ATP, shown in Fig. 3.3. Our results follow Michaelis-Menten kinetics that is defined as:

$$v = \frac{V_{max}[S]}{K_m + [S]}$$

where v is the velocity, [S] is the substrate concentration (ATP concentration), V_{max} is the velocity at saturating substrate concentrations and K_m is the Michaelis constant that describes the substrate concentration when the reaction rate is half of V_{max}.

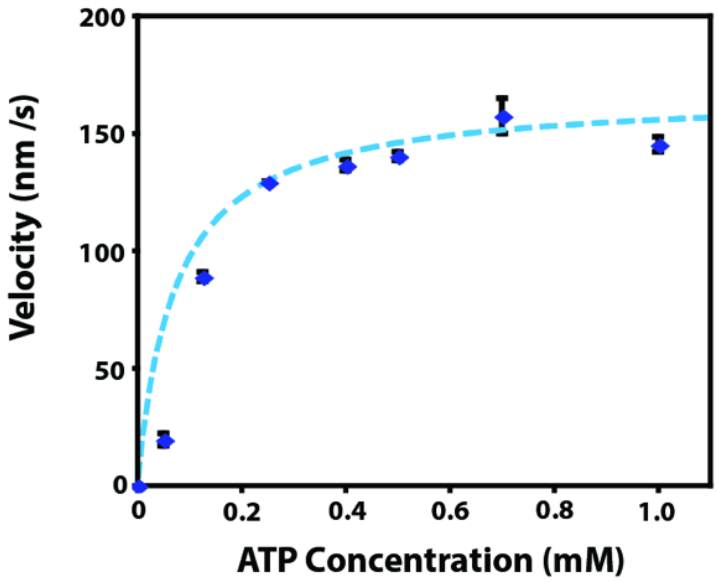

Fig. 3.3) Microtubule gliding velocity as a function of ATP concentration. Error bars are standard error of the mean. The dashed line represents the Michaelis-Menten fit with K_m=154±54μM and V_{max}=286±28 nm/s. (reproduced from Tan et al. 2016 with permission ©2016 Centre National de la Recherche Scientifique (CNRS) and The Royal Society of Chemistry)

We chose three velocities spanning from slow to fast transport velocities (31±1 nm/s, 190 nm/s, 222±9 nm/s) and imaged the spool formation over the span of 2 hours. A time lapse image of the spool formation for the lowest velocity and highest velocity are shown in Fig. 3.4. A non-zero transport velocity is necessary for spool assembly. The non-zero transport velocity is necessary to decrease the distance between the microtubules so that the filaments can form bundles and potentially form a spool.

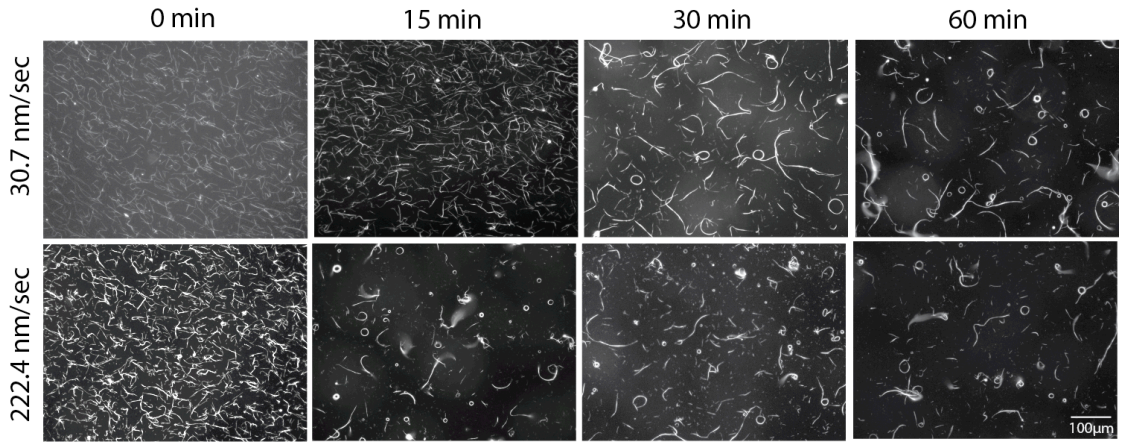

Fig. 3.4) Fluorescence microscope images of microtubule spool formation over 1 hour at 30 nm/s and 222.4 nm/s. (reproduced from Tan et al. 2016 with permission ©2016 Centre National de la Recherche Scientifique (CNRS) and The Royal Society of Chemistry)

ATP is required for spool rotation. Fig. 3.5 shows the relative tangential velocity of three spools rotating as a function of time. The relative velocity was normalized by the max velocity in the system. In time interval I, spools are rotating at a non-zero velocity at saturating levels of ATP (1mM). ATP was subsequently flushed out by flowing in motility mix without ATP. Time interval II shows evidence for ATP reduction as the relative velocity of spools decreases to a stop. ATP is reintroduced, and the spools continue to rotate, show in time interval III.

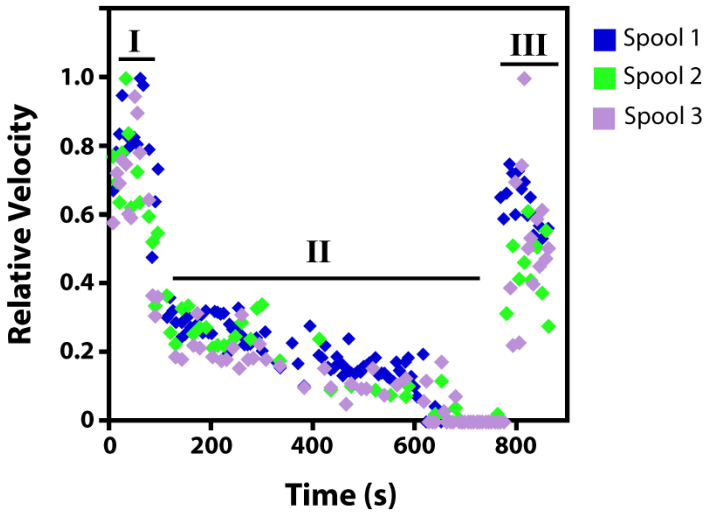

Fig. 3.5) Spool rotation stop and restart with ATP. Relative tangential velocity, normalized by maximum velocity of each spool, of three spools as a function of time. Time interval I is spool rotations at saturating levels of ATP (1mM). Time interval II shows the gradual decrease in ATP levels until the spools halt rotations. Time interval III shows relative velocities after reintroducing ATP at 1mM.

3.3.2 Transport velocity influences initial spool formation rate

Initially, we measured the number of spools as a function of time for three transport velocities as shown in Fig. 3.6. The rate of spool assembly was well characterized by the asymptotic function

$$y = A\left(1 - e^{\frac{-t}{\tau}}\right)$$

where A is a fitting constant, t is time, and τ is a time constant describing the time at which the system reaches a steady state.

At the lowest transport velocity, 31±1 nm/s, the time constant, τ, was measured to be 29±10 min, at the intermediate transport velocity of 190±2 nm/s, τ=5±1 min, and at the highest transport velocity 222±9 nm/s, τ=3±2 min. At the maximum transport velocity, we observed the maximum number of assembled spools reached a peak of 27 spools at 15 min, which then reduced by ~20% over the next 40 min. This peak and reduction in number of spools is consistent with observations of a metastable state where spools were observed to disassemble before reaching a steady state[85]. When the spools are in a metastable state, there is a balance between the mechanical strain from the bent microtubules and the energy stored between the biotin and streptavidin bonds[52]. Over the 2-hour time period, the maximum number of spools assembled for all transport velocities was between 15-20 spools.

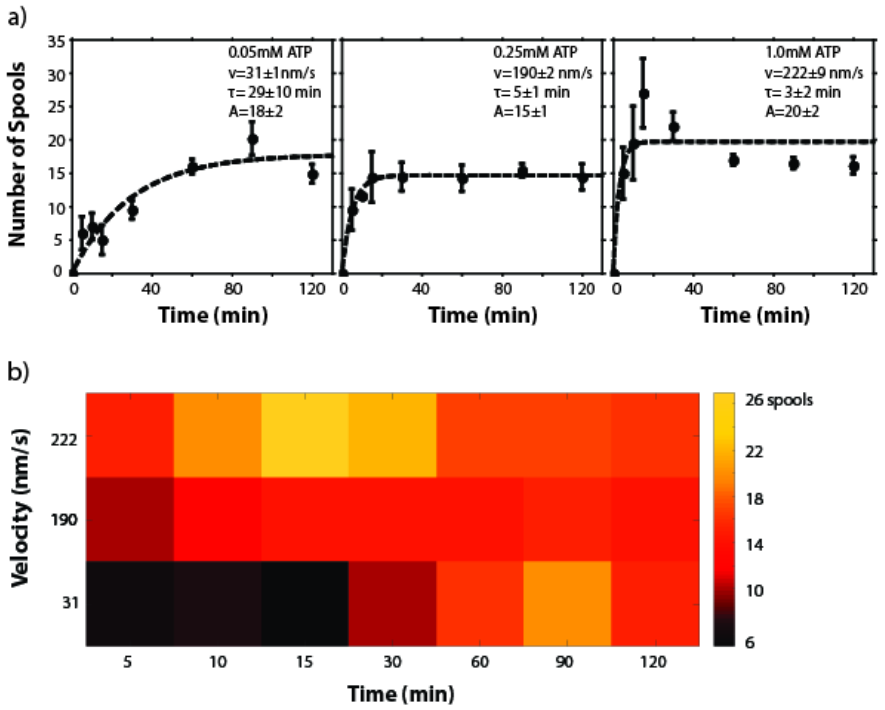

Fig. 3.6) a) Spool density as a function of time for each transport velocity (31±1nm/s, 190±2 nm/s and 222±9 nm/s). b) Heat map of number of spools as a function of velocity(nm/s) and time (min). (reproduced from Tan et al. 2016 with permission ©2016 Centre National de la Recherche Scientifique (CNRS) and The Royal Society of Chemistry)

3.3.3 Transport velocity has no influence on spool density at steady state

At steady state, the number of spools remained approximately constant for all transport velocities. We compared the number of spools assemble at the same time points over a 2-hour period Fig. 3.6. During the first ~40 min, there was a strong dependence on the spool number with increasing transport velocity. The number of spools increased more rapidly at higher transport velocities. Fig. 3.6b shows a heat map of the spool density as a function of time and velocity. After 60 min, we did not observe any dependence of spool number on transport velocity. At the steady state the transport velocity does not influence the number of spools.

3.3.4 Transport velocity influences spool size at initial assembly

For each transport velocity we observed the change in spool size (spool circumference) over time. We again fit the data to the asymptotic function as shown in Fig. 3.7a. The circumference for spools for all transport velocities increased over time. There are two possible mechanisms for the increased spool size over time: spool relaxation over time, or possible spool disassembly. The relaxation model suggests a metastable state exists at approximately 15 min where the spools can disassemble[86]. From our data, there was no

detectable change in spool circumferences between 15-60 min; therefore, our data does not support the relaxation model. Instead, our data supports the model where spools can disassemble, but the spools size is mainly dependent on initial conditions at spool nucleation[87]. A possible reason for the smaller spool circumferences initially could be due to confinement. Initially, the microtubules are all in close proximity to each other; therefore, if spools are formed, the size is limited by the surrounding microtubules. Small spool sizes due to this confinement effect was previously observed for bare microtubules (no biotin and streptavidin) at high concentrations[56]. In our experiment, since the microtubules are decorated with biotin and streptavidin, they can bundle and form spools at faster rates at high transport velocities, we expect the influence of the confinement effect to decrease, and the spool size increases with increasing transport velocity. Over the range of velocities tested, there was an increase in initial spool size, which supports our prediction. At the lowest velocity, 31±1 nm/s, the initial spool size was measured to be 3 ± 1 μm, and at the highest velocity 222±9 nm/s, the initial spool size was 9±1μm.

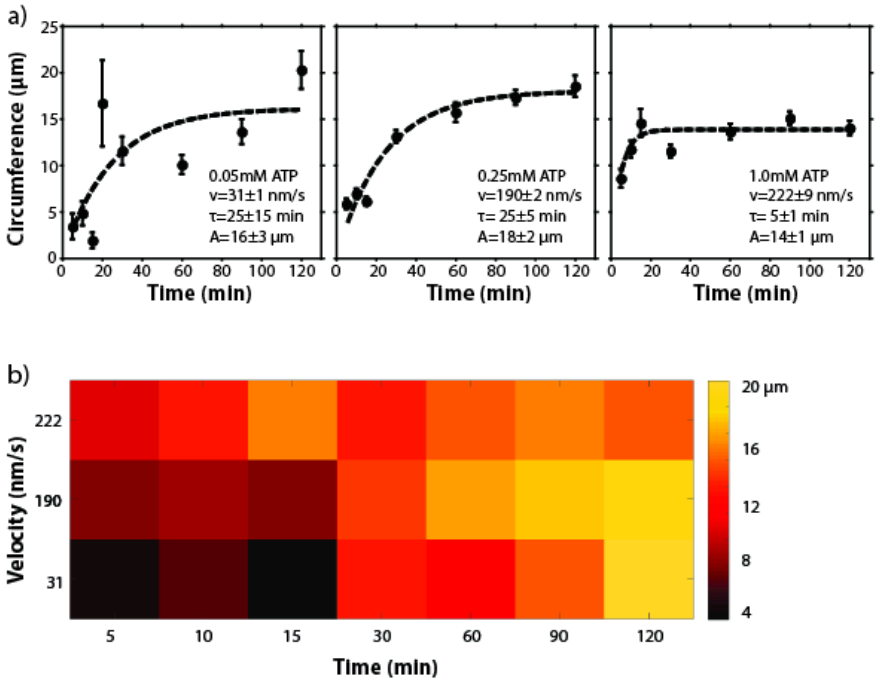

Fig. 3.7) a) Average spool circumference as a function of time for three transport velocities. b) Heat map of spool circumference as a function of velocity (nm/s) and time (min). (reproduced from Tan et al. 2016 with permission ©2016 Centre National de la Recherche Scientifique (CNRS) and The Royal Society of Chemistry)

3.3.5 Transport velocity has no influence on spool sizes at steady state

Over the 2-hour period, the average spool circumference for all transport velocities approached similar values (14-18 μm). This result is still consistent with the speculation that the confinement effect largely influences the spool size at initial assembly. As

microtubules assemble into bundles and the number of spools increases over time for low transport velocities, the distance between neighboring bundles increases and the confinement effect has a reduced effect on the spool sizes formed. The heat map in Fig. 3.7b shows the circumference size as a function of time and velocity. There were no observable differences in spool sizes at time points past 30 min for all transport velocities; therefore, the spool size is not substantially influenced by transport velocity at the steady state.

3.4 Conclusions

In conclusion, we studied the role of transport velocity on spool assembly. We found that a non-zero transport velocity is necessary to reduce the distance between microtubules to initiate spool formation, but has no influence on number of spools formed at times >40 min. Also, transport velocity influences the size of spools initially because of the confinement effect due to crowding from neighboring moving filaments. Over time, the distance between microtubules increases for all velocities, thus reducing the confinement effect, so the spool size for all transport velocities reached the same asymptotic value at the steady state. Understanding the factors driving spool formation is an important step toward using this self-assembly in nanotechnology, such as applications in building artificial bio-machines.

Acknowledgements
I'd like to acknowledge Jing Xu for her help and guidance throughout this project. Thank you to Dail Chapman for purifying the kinesin motors used in these experiments.

Chapter 4: Topological Chaos in Active Nematics

In Chapter 2, section 2.3.3, I discuss the active nematic composed of microtubules and kinesin motors, that has self-generated flows. In this Chapter, I will be discussing our work in approaching the generated flows in the 2D active nematic from the perspective of chaos.

4.1 Introduction

Active microtubule networks are an exciting nonequilibrium system that has self-generated flows. When the microtubule active network is confined to two-dimensions at an oil/water interface, active ±1/2 topological defects emerge. These defects constantly undergo creation and annihilation events in the active steady state. The active stresses in the moving defects generates a backflow in the surrounding flow field which drives the +1/2 defects away from their -1/2 counterpart after creation[15,88]. The active defects are considered to be self-propelled particles generating fluid flows with rich dynamics.

Groups have described the generated flow as exhibiting turbulent-like behavior. Active turbulence is characterized by highly disordered distribution of vortices[16,89,90]. Experimental evidence shows vortices are generated from the flow field[64], and there is a distribution of vortices, which is a characteristic of turbulence[61]. Turbulence has been used to describe the flows generated in the active steady state of the active nematic[16].

Here, we approach the active network from a chaotic advection point of view. Until now, the focus has been using turbulence to describe the active flows generated in the steady state; however, our hypothesis is that we consider the active nematic to be a self-mixing active fluid and introduce concepts from chaos theory to describe the flow dynamics. We use measures of chaos, specifically the topological entropy and the Lyapunov exponent, to study the complexities of the active fluid.

Experimental studies of chaotic advection in passive fluids drive the fluid motion externally at the boundaries by tangentially sliding the boundary, like with a rotating cylindrical wall[76,91,92], or by direct stirring using inserted rods[80,93,94]. As these methods drive the fluid, the material lines of the fluid become stretched and folded, increasing the complexity of the interface of the fluid. Chaos is characterized by exponential stretching of material curves. Fig. 4.1 shows examples of exponentially stretched fluid lines in a stirring experiment. Experiments involving stirring rods exhibit chaos when three or more rods move around one another, dragging and pulling the fluid with it. The rod motion can be described as braiding[79]. The topological entropy is the asymptotic (in time) growth rate of material lines stretched in a fluid. Each rod exchange during stirring imparts a minimal amount of topological entropy to the system.

Fig 4.1) Three-rod stirring experiment showing exponential stretching of the fluid material. (Reproduced from Boyland, 2000 with permission ©Cambridge University Press)

Our system differs from classic fluid mixing experiments because our fluid is driven internally with energy injected at the local level. We consider the 2D active nematic to be a fluid where the topological defects are virtual rods stirring the microtubules. The microtubules are considered to be fluid material that is advected throughout the system.

We impose three methods to measure the topological entropy and measure the Lyapunov exponent in this active fluid. Surprisingly, we observe exponential stretching in the fluid based on local stretching of the fluid material, which implies there must be some type of braiding occurring by stirring rods (defects). We quantify the braiding of defects and find that the defects move in a specific way that accommodates local stretching. This is evidence supporting the energy injected at the local level give rise to the large-scale defect stirring.

We quantified the topological entropy three ways to probe both different length-scales in the system. We also calculated the Lyapunov exponent of the flow by taking the gradient of the velocity field. We calculated the velocity field of the active fluid using PIV analysis. To measure the topological entropy from local stretching, we used beads bound to the network to measure the rate at which microtubule bundles extend away from each other. Additionally, we made a similar measurement of local stretching by measuring the rate of defect pair separations. The third method of measuring topological entropy is by defect braiding, where we tracked the defect trajectories as they process through the fluid and calculated the topological entropy through their braiding. With defect braiding, we found positive defects are responsible for generating all the topological entropy in the fluid, and negative defects contribute very little, if any, topological entropy. Remarkably, we found the three independent measures of topological entropy are consistent with one another despite the differences in length-scales. Additionally, braiding depends on the global geometric characteristics of the flow, whereas bead separation and defect stretching depend only on length measurements.

We then repeated the experiments and analysis for increasing ATP concentrations, thus tuning the energy levels driving the active fluid. With increasing energy, we observed

the topological entropy and Lyapunov exponent generally increase; however, when we nondimensionalized these quantities so that the values are based solely on geometric effects to the flow, all methods collapse to a fairly constant value for all ATP concentrations. This is a fascinating result that may imply that the nondimensionalized topological entropy is a universal quantity that describes these active fluids in the steady state.

4.2 Experimental Methods

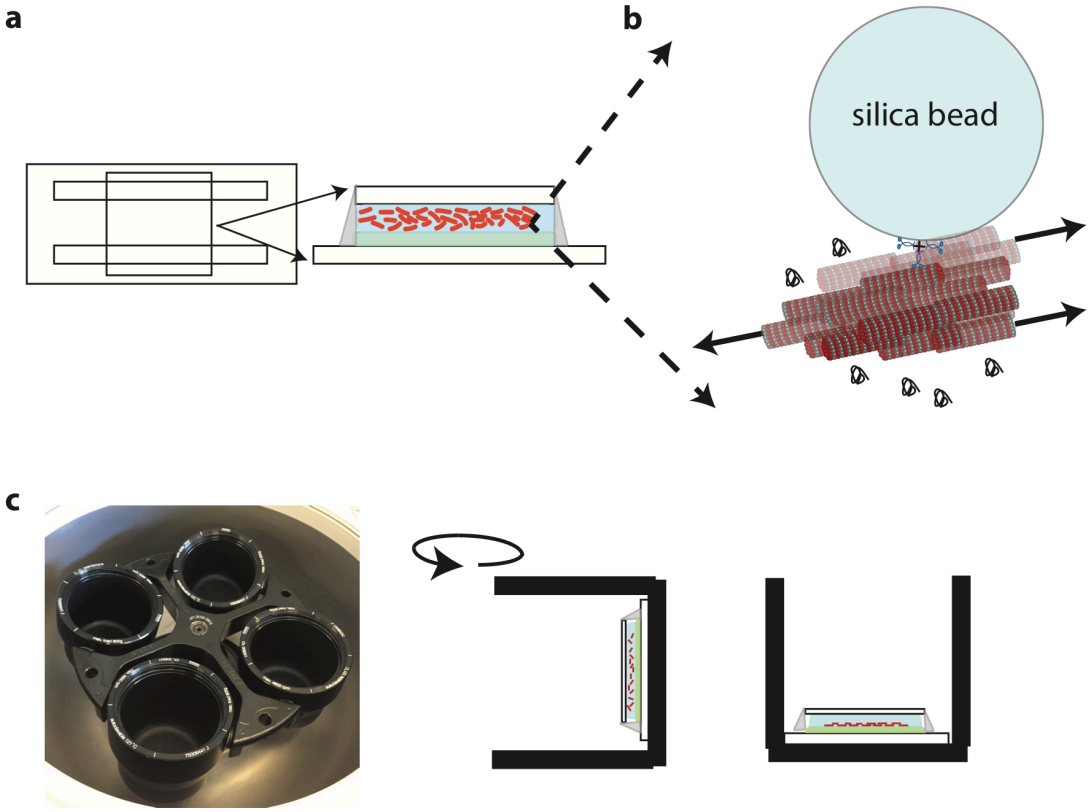

Fig. 4.2) Schematic of 2D active nematic experimental setup. a) Flow-cell constructed with double-stick tape, hydrophobic glass-slide and hydrophilic cover-slip. Side view of the sample suspended above the oil later. The edges are sealed with a UV-curable glue. b) The active network of microtubule bundles with silica bead attached. c) To confine the network to 2D, the sample is placed into a swinging bucket centrifuge to spin down the 3D network.

4.2.1 Flow-cell preparation

Flow-cells for active nematic experiments are constructed using a hydrophilic coverslip, hydrophobic glass-slide and double-stick tape as described by Sanchez et al[4]. Fig. 4.2a shows a schematic of the constructed flow-cell. Two pieces of double-sided tape are placed about 2mm apart on the glass slide to create a channel. The hydrophilic coverslip

is then placed on top of the channel. The different surface treatments are required in order to allow both oil and water to pass through the flow-cell.

The hydrophilic coverslip was treated with an acrylamide polymer brush to prevent non-specific protein binding. The coverslips are first washed with warm soap and water and rinsed with deionized water three times until all the soap residue is gone. The coverslips are then washed with ethanol and rinsed in deionized water three times. Next, the coverslips are rinsed in 0.1M NaOH and rinsed with deionized water three times. These coverslips are submerged in a solution containing 98.5% ethanol, 1% acetic acid, and 0.5% silane-bonding agent 3-(trimethoxysilyl)proylmethacrylate (Arcos Organics) for 15 min, and then rinsed three times with deionized water. Finally, the coverslips are submerged in an acrylamide solution containing 2% (w/v%) acrylamide, 35 µl per 100 ml of tetramethylethylenediamine (Bio-Rad) and 70 mg per 100 ml of ammonium persulfate. This helps polymerization of the polyacrylamide brush onto the surface of the coverslips. The coverslips are store in this acrylamide gel until use. Before use, the coverslips are rinsed in deionized water and left to air-dry.

The hydrophobic glass slides are first cleaned with acetone, methanol, and ethanol. These slides are then treated with commercially available Aquapel by putting 50µl of the solution onto a slide. Another cleaned glass slide is placed ontop, perpendicular to the first slide with Aquapel in order to spread the solution evenly on both slides. The slides are left to sit for 1 min before dried with compressed air, rinsed with water and left to air-dry before use.

4.2.2 Preparation of 2D active nematic

Microtubule polymerization and kinesin-streptavadin cluster preparation was carried out as previously reported in Sanchez et al.[4]. Biotin-coated 2µm diameter silica beads (Nanocs) are diluted to 5000 beads per µl in M2B buffer (80mM PIPES at pH 6.8, 2mM $MgCl_2$, 1mM EGTA) and placed in a bath sonicator for 30 min to 1 hr to break up bead aggregates. An active premixture containing biotin-kinesin, streptavidin, 20kD PEG (poly(ethylene glycol)), PKLDH and PEP (an ATP-regenerating system) is prepared as described in Sanchez et al. Two antioxidant mixtures are used along with Trolox to avoid photobleaching during imaging. Antioxidant solution, AO1 which contains 150 mg/ml glucose and 250mM dithiothretitol. Antioxidant solution AO2 contains 10mg/ml glucose oxidase and 1.75 mg/ml catalase. The kinesin-streptavidin clusters (KSA) are made by combining 0.31 mg/ml K401-BIO kinesin motors and 0.18 mg/ml streptavidin and 2.2 µl/ml dithiothreitol and incubated on ice for 30 min. This mixture is diluted with M2B in the ratio of 1:8.6. A high-salt buffer (MIX) is prepared containing 69mM $MgCl_2$ diluted in M2B. The ATP-regenerating system is prepared with 917 units/ml pyruvate kinase and 913 units/ml lactate dehydrogenase in aqueous buffered glycerol solution (PKLDH). The final premixture is produced by adding 1.33µl AO1, 1.33µl AO2, 1.7µl PKLDH, 2.9 µl MIX, 4 µl KSA, 6 µl 20mM Trolox, 8µl 200mM phophoenolpyruvate and 8µl 6%(w/v) 20kD PEG. The premixture is separated into 6.64 µl aliquots.

The active network is formed by adding ATP (0.05-1mM) to one aliquot and fill to 10µl with M2B. Then, 2µl of 6mg/ml Alexa-647-labelled GMPCPP microtubules (~3% labelling) is added to the premixture. The mixture is incubated for 5-30 min at room

temperature to allow the network to form. The network takes longer to form at lower ATP concentrations. Finally, 0.5µl of the silica bead solution is added to the microtubule network and tapped to mix.

Fig. 4.2 shows a schematic of the experimental setup. To create a 2D active nematic layer at the oil-water interface, we first flow an oil-surfactant mixture (HFE7500 with 1.8% (v/v) PFPE-PEG-PFPE (perfluoropholyether) surfactant) into the channel. Then, the oil is immediately exchanged with the aqueous solution containing the active network. The flow cell is sealed with ultraviolet-curable glue (RapidFix). To confine the active network into a quasi-2D layer, we place the filled flow-cell to the bottom of a swinging bucket rotor (Sorvall Legend RT+ centrifuge, four-place swinging bucket rotor), and spin the material down for 42 min at 350 rpm. The step allows the active network to sediment to the oil-water interface of the flow cell.

4.2.3 Imaging and analysis

Our samples were imaged using a Leica Microsystems Inc. DM2500 P fluorescence microscope and a QImagin Retiga Exi camera. Fluorescence microscopy movies were recorded with 500ms exposure and 100ms time interval between frames. The bright-field microscope movies of the beads are recorded using a 10ms exposure and 100ms intervals between frames. We used a MATLAB-adapted tracking algorithm from Crocker et al.[95] to track bead trajectories.

The bead attachment remained stable over the course of the experiment; unbound beads were distinguished from their characteristic Brownian motion and tendency to sediment to the glass slide during centrifugation. Unbound beads and bead clusters were eliminated from the analysis. To measure the separation distance between separating beads, we used the segmented line tool in ImageJ to measure the contour length of the nematic network connecting the two beads for each successive frame for the duration of the movie.

Defect separations were measured using a defect tracking algorithm that calculates the director field of the nematic network. The defects are identified from the singularities in the director field. Emerging defect pairs are manually selected. A contour length linking the ±1/2 defects as they separate is automatically drawn based on the underlying director field. As the defect pair separates, the growing contour length is recorded.

4.2.4 PIV analysis

Velocity fields of the nematic network were calculated by using PIVlab 1.43 in MATLAB, using the default graphical user interface settings (FFT window deformation PIV algorithm, with a 64-pixel interrogation window on the first pass, and 32-pixel interrogation window on the second pass). PIVlab calculates the velocity vector field for each frame by using sequential images of the movie. We did PIV analysis for both bright-field and fluorescence movies at every ATP concentration. We calculated the root-mean-squared velocity, v_{rms}, in the center of velocity frame. To find the average velocity in the center of velocity frame, we calculated the average velocity vector in each frame and subtracted it from every velocity vector in the frame. We then calculated the resulting root-mean-squared velocity for each frame and averaged over all frames for the final v_{rms} value.

Using the velocity field data, we computed the velocity-velocity correlation length, which is defined as the active length scale. This length scale is used to define the distance between defects in the active nematic. The velocity correlation function is defined as

$$C(r) = \sum_{i,j} \hat{v}_i \cdot \hat{v}_j \delta(r - r_{ij})$$

where i and j range over all frames and grid points within a frame, $\hat{v}_i = v_i/|v_i|$ is the unit velocity vector, and $r_{i,j} = |r_i - r_j|$ for grid points r_i and r_j. The active length scale or correlation length is defined as the distance at which the correlation function decays to half its max at $r = 0$.

4.3 Results

4.3.1 Tracking beads bound to the active network

Since topological entropy is a measure of increasing complexity in a fluid as the material stretches and folds, one method of measuring this quantity in the system is to observe filament bundles stretching or extending away from each other. This gives a measure of local stretching in the active fluid. This analysis is analogous to measuring the stretching of fluid material (such as paint) as it is mixed. Microtubules sliding next to each other within the bundle are beyond the optical resolution limit in size. To work around this issue, we introduced silica beads functionalized with biotin into the active network after its assembly. The biotin on the silica beads binds to free streptavidin binding sites in the kinesin clusters. We used the beads as a proxy for locating microtubule bundles.

It is evident that the beads are bound to the network because the mismatch in density of silica particles (~2g/cm^3) and the aqueous solution (~1g/cm^3) means that the silica particles will sediment to the bottom of the flow cell when centrifuged. When the particles are properly bound, they remain on the network. Furthermore, if particles were not tightly bound, it would be expected that these particles act like tracer particles advected by the generated flows[4]. In our system, the beads move with the moving network. Fig. 4.3a shows bound beads located on the microtubule active network and Fig. 4.3b shows the trajectories of beads. Using these beads, we measured local microtubule bundle stretching in the active nematic.

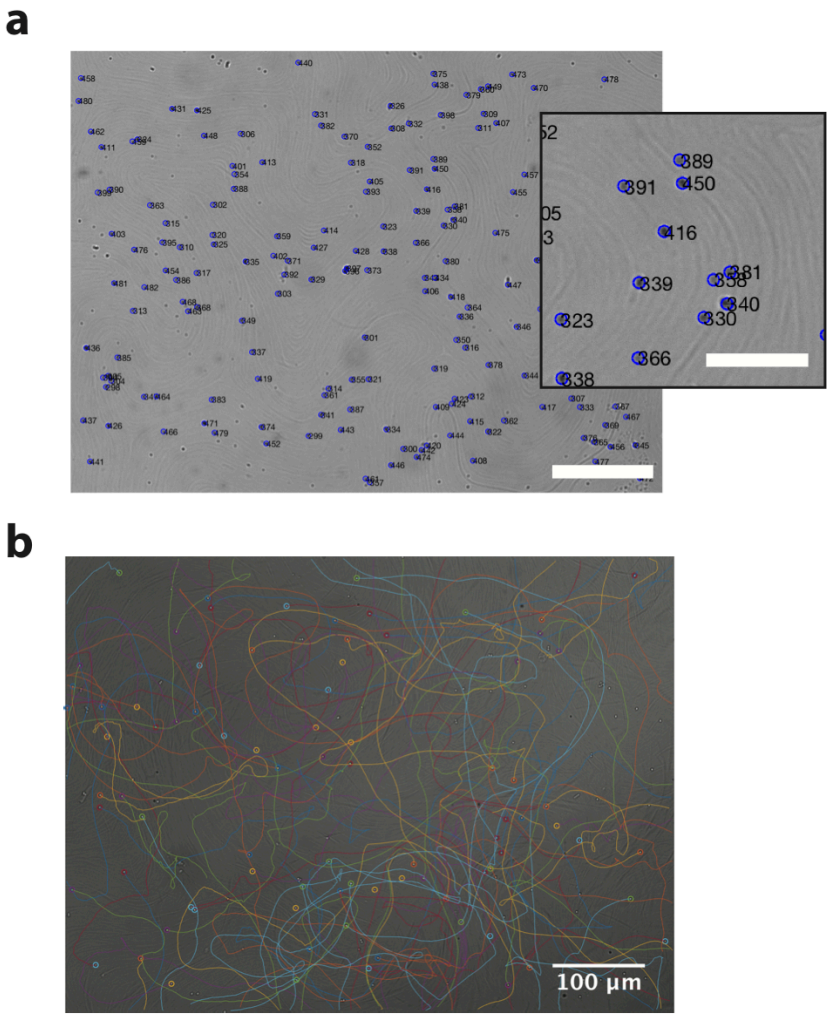

Fig. 4.3) a) Bright-field microscopy image of beads bound to the microtubule active network. Scale bar, 100 µm. Inset: a close-up of beads on the visible underlying network. Scale bar, 50 µm. b) Trajectories of beads plotted on a single frame. Scale bar, 100 µm.

4.3.2 Topological entropy measured from bead separation

We measured the topological entropy from local stretching of the network from the rate of separation of initially nearby beads. Initial experiments were done with 50 µM ATP concentration. Beads that are initially located within 2-10 µm from each other and separate over time are considered candidates. As the beads diverge away from each other, we measured the growing contour length of the underlying network connecting the two beads. Fig. 4.4a shows an example of two beads and the growing contour line between a bead pair. Tracing the contour line of the underlying network is a more accurate representation of microtubule bundle trajectories as they advected within the fluid. Tracking the growth of the contour line, as a function of time, we can extract a stretch rate by the relation

$$|d(t)| \approx e^{rt}$$

where d is the length of the contour line, t is time, and r is the stretch rate. Fig. 4.4b shows the semi-log plot of the growth of the contour length as a function of time. The slope of this semi-log plot is the stretch rate. Surprisingly, the separating beads resulted in a linear fit, indicating exponential stretching between microtubule bundles. Fig. 4.5b shows three bead pair examples from the same sample all with exponential stretch rates.

The topological entropy is the exponential stretch rate of a material in the limit that time goes to infinity where the material has stretched to fill the whole space. This proved to be challenging in the given experimental system because we had an open boundary where the field of view is only a portion of the whole flow cell. Since we had an open boundary, it is not possible to track the beads once they left the field of view. Also, the bead tracking algorithm has complications in tracking beads throughout the whole movie. It is possible for the tracking algorithm to lose the bead during tracking, which also limits the timespan for tracking a bead. To resolve these limitations, we took the weighted average of the stretch rate for several bead pairs where the weight is the contour length at the final time of the fit interval between the bead pairs. This method using a weighted average for several bead pairs is a way to sufficiently sample the space accounting for spatial variations. Therefore, we can approximate the topological entropy, h to be

$$h = < w_i \, r_i >$$

where w_i is the contour length at the final fitting point and r_i is the stretch rate between bead pairs, i. The topological entropy measured for local stretching by bead pair separation is $h_{bead} = 0.0145(\pm 0.0001)$ s^{-1}. The error is the standard error of the mean of the topological entropy

$$\Delta h_{bead} = \frac{\sigma}{\sqrt{N}}$$

where N is the number of bead pairs and σ is the weighted standard deviation given by

$$\sigma = \sqrt{w_i {r_i}^2 \, - \, (w_i r_i)^2}.$$

h_{bead} resulting in a positive value is an early indication that the 2D active nematic shows exponential stretching and chaotic advection in its fluid motion.

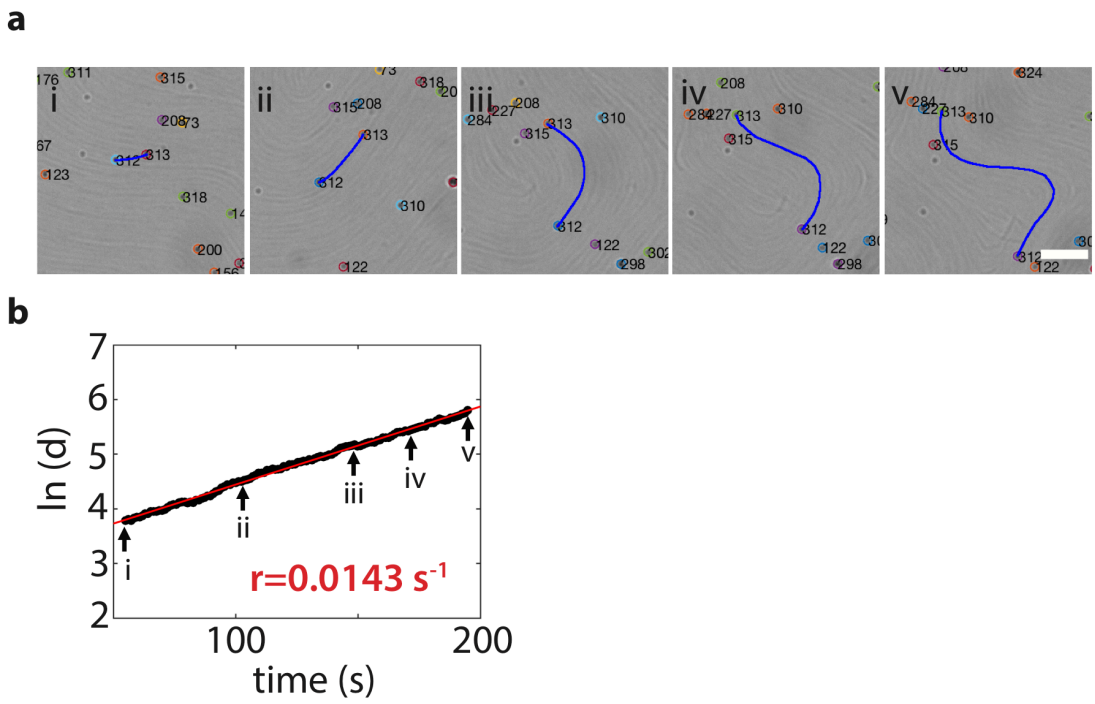

Fig. 4.4) Bead separation rate a) Time-lapse images of growing contour line growth (blue) between separating beads. Scale bar, 30 μm. b) Semi-log plot of the contour length, d, as a function of time in s for the corresponding bead pair from (a). (i-v) indicate the corresponding contour lengths shown in (a i-v). (reproduced from Tan et al, 2019 with permission ©2019 Nature Springer)

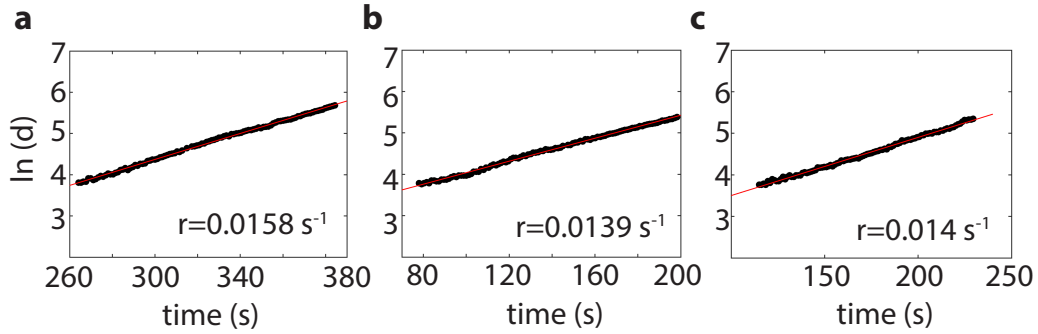

Fig. 4.5) Examples of semi-log plots of three bead pairs and their corresponding stretch rate, r = a) 0.0158 s^{-1}, b) 0.0139 s^{-1}, and c) 0.014 s^{-1}. (reproduced from Tan et al, 2019 with permission ©2019 Springer Nature)

4.3.3 Measuring topological Entropy from defect separation

Another method of measuring local stretching in the 2D active nematic is to measure the rate of separation of ±1/2 defect pair after they are created. We used the

fluorescence movies that were taken ~10 minutes after the bright-field movies of the beads to identify defect pairs. To measure defect pair separations, we used a defect tracking algorithm that extracted the director field from the images, and located the defects based on discontinuities in the director field. Fig. 4.6 shows an image from the fluorescent movie of the microtubule network with the ±1/2 defects marked. We conducted a similar analysis as with bead pairs, where we selected defect pairs that were separating and measure the contour length connecting the two pairs over time. The defect tracking algorithm automatically traces the contour length based on the director field from the selected -1/2 to +1/2 defect. This was repeated for each frame as the pair separates.

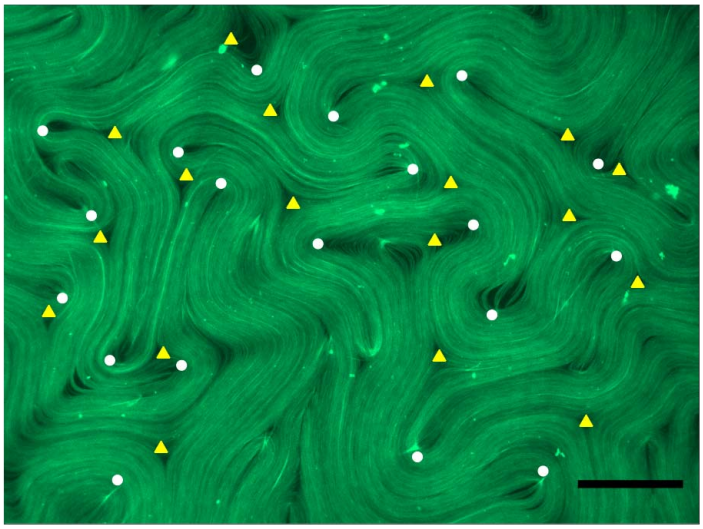

Fig. 4.6) Fluorescence microscope image pseudo-colored in green of the 2D active fluid with +1/2 (white circles) and -1/2 (yellow triangles) marked. Scale bar, 100μm. (reproduced from Tan et al, 2019 with permission ©2019 Springer Nature)

Fig. 4.7a shows an image sequence of measuring the defect separation between a pair of defects and Fig. 476b shows the corresponding semi-log plot of the contour length growth as a function of time. Similar to the bead separation, the defect separation rate shows exponential stretching. With defect stretching, the semi-log plots showed an initial steep slope which corresponds to a transient state where defect pairs first emerge. Upon creation, the defect pairs undergo a quick initial separation, which is an artifact of the defect creation, so we start the fit once there is sufficient separation. Similar to bead pair stretching, measuring multiple pairs of defect separations resulted in linear semi-log plots shown in Fig. 4.8, indicating exponential stretching in the active fluid. The topological entropy measured from the weighted average of defect separation rates is, $h_{defects}$=0.0142(±0.0002) s^{-1}. Interestingly, the topological entropy measured from both these independent methods of probing local stretching results are in close agreement. Both topological entropy measurements result in positive values which is a characteristic of chaotic advection.

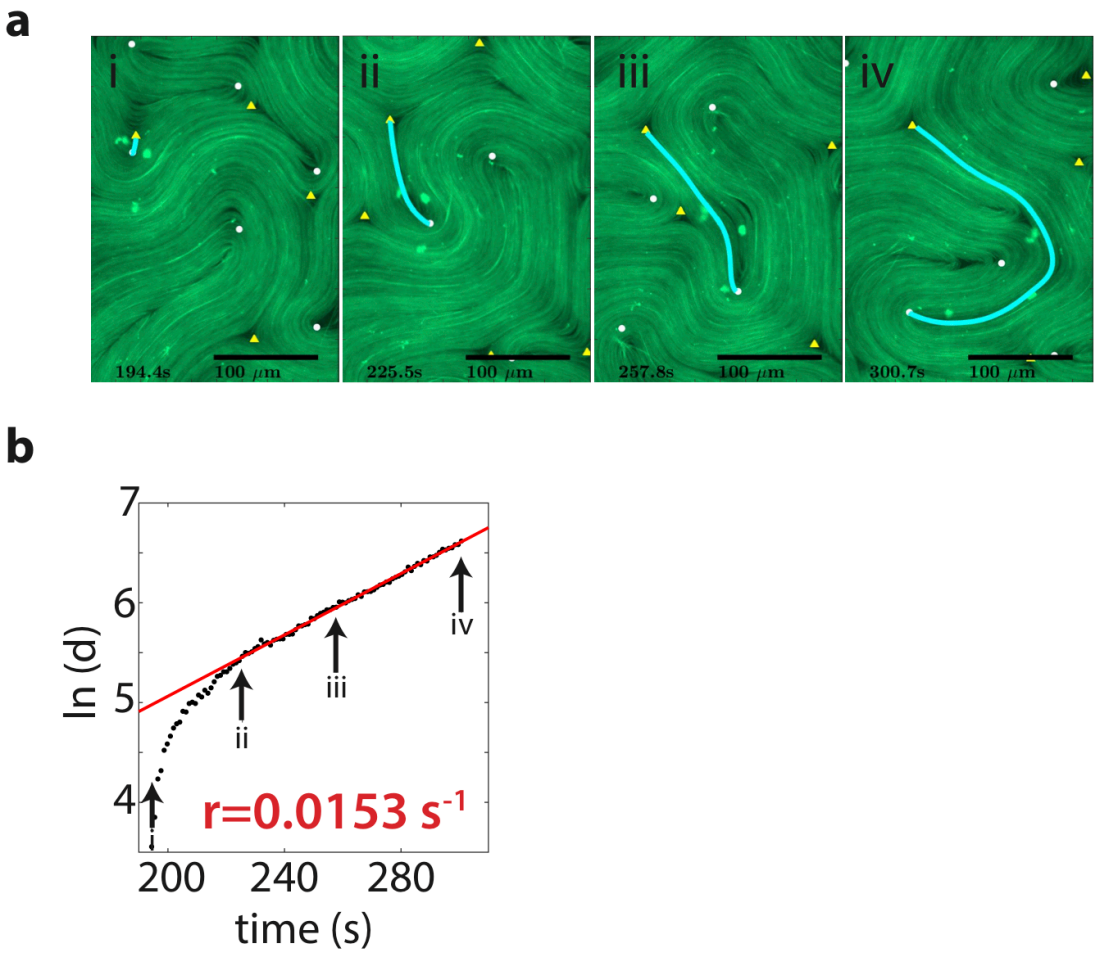

Fig. 4.7) Defect separation rate a) An image sequence of tracking the growing contour length of a pair of defects as they separate. b) Semi-log plot of the growing contour length as a function of time for the corresponding pair in (a). b i-iv) are the time points corresponding to the images in (a i-iv). (reproduced from Tan et al, 2019 with permission ©2019 Springer Nature)

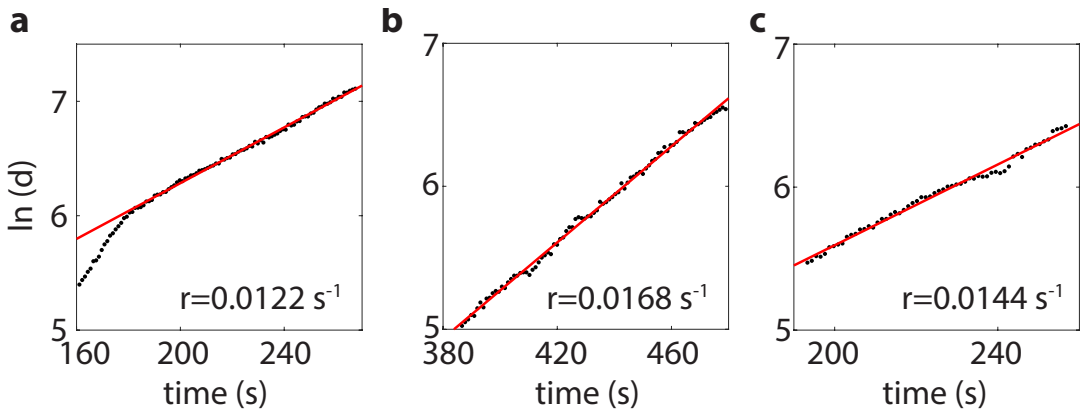

Fig. 4.8) Semi-log plots of growing contour length as a function of time with defect separation rates, a) 0.0122 s^{-1}, b) 0.0168 s^{-1}, and c) 0.0144 s^{-1} for 50μM ATP. (reproduced from Tan et al, 2019 with permission ©2019 Springer Nature)

4.3.4 Varying energy input at the local level

The 2D active nematic exhibits characteristics of chaotic advection that is seen in chaotic mixing. Since collective motion in active materials arises from individual units consuming energy, we hypothesized that change in input energy will change the overall collective dynamics. To address this hypothesis, we varied the concentration of ATP in the active network and measured the topological entropy as a function of ATP. We measured the root-mean square velocity of the active network by using PIV analysis on the movies of beads attached to the network. The V_{rms} of the network as a function of ATP is shown in Fig. 4.9. Similar to kinesin motors walking along filaments or gliding microtubules, the network velocity as a function of ATP follows Michaelis-Menten kinetics. The collective dynamics of the network are faster than those for individual microtubule gliding where the V_{max}~3μm/s for the active network, but V_{max}~0.15μm/s for microtubule gliding from chapter 3. This discrepancy may arise from the difference in the geometry of the system. In the active network, the kinesin motors in the cluster crosslinking the bundles are walking in opposite directions, thus propelling the microtubule bundles so that they slide relative to each other. Since kinesin motors are propelling the microtubules from both sides, the overall dynamics may be enhanced.

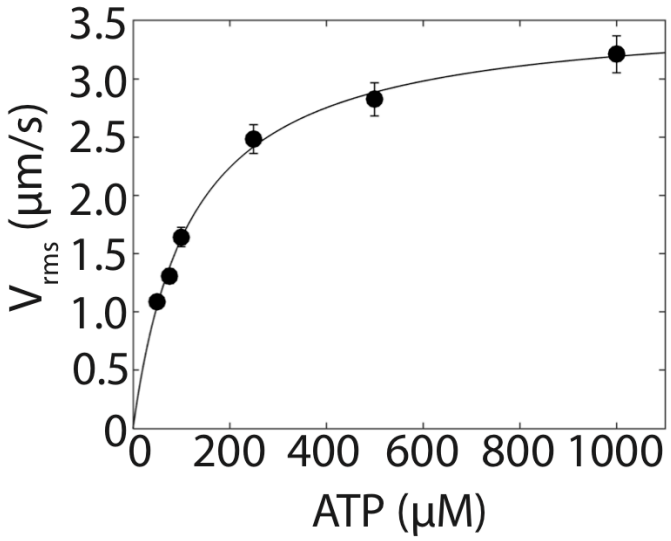

Fig. 4.9) Root-mean square velocity of the active network as a function of ATP. The V_{rms} is measured from PIV analysis from beads. The relationship follows Michaelis-Menten kinetics with fit parameters, K_m=120(±20) μM and v_{max}=3.57(±0.19) μm s^{-1}. (reproduced from Tan et al, 2019 with permission ©2019 Springer Nature)

Fig. 4.10 and Fig. 4.11 show the distribution of bead separation rate data and defect separation data for ATP concentrations from 50μM to 1000μM. The dashed line shows the mean bead separation rate, or defect separation rate, <r>, and the gray shaded region indicates the standard deviation calculated from the data set. In both bead pair and defect pair separations, there is more variation in separation rates at high ATP concentrations. At higher ATP concentrations, the defect dynamics are faster where the lifetime of the defects are shorter. These increase in dynamics may be the source for variation in the defect separation rate.

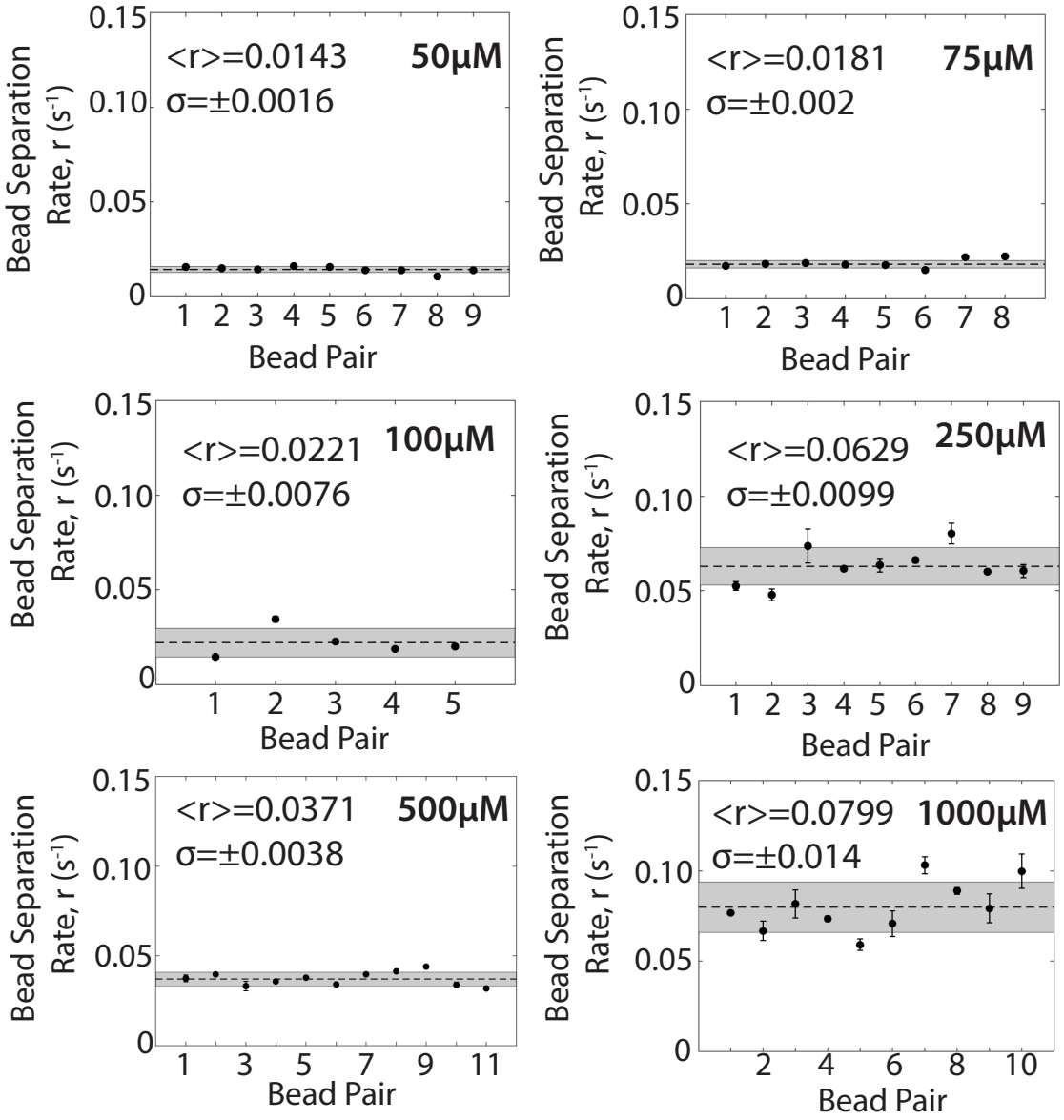

Fig. 4.10) Bead separation rate, r (s^{-1}), of bead pairs for ATP concentrations ranging from 50μM to 1000μM. The average separation rate, <r> is shown by the dashed line, and the standard deviation, σ, is denoted by the gray shaded region. The error bars on each bead pair are from the goodness of fit from the semi-log plots. (reproduced from Tan et al, 2019 with permission ©2019 Springer Nature)

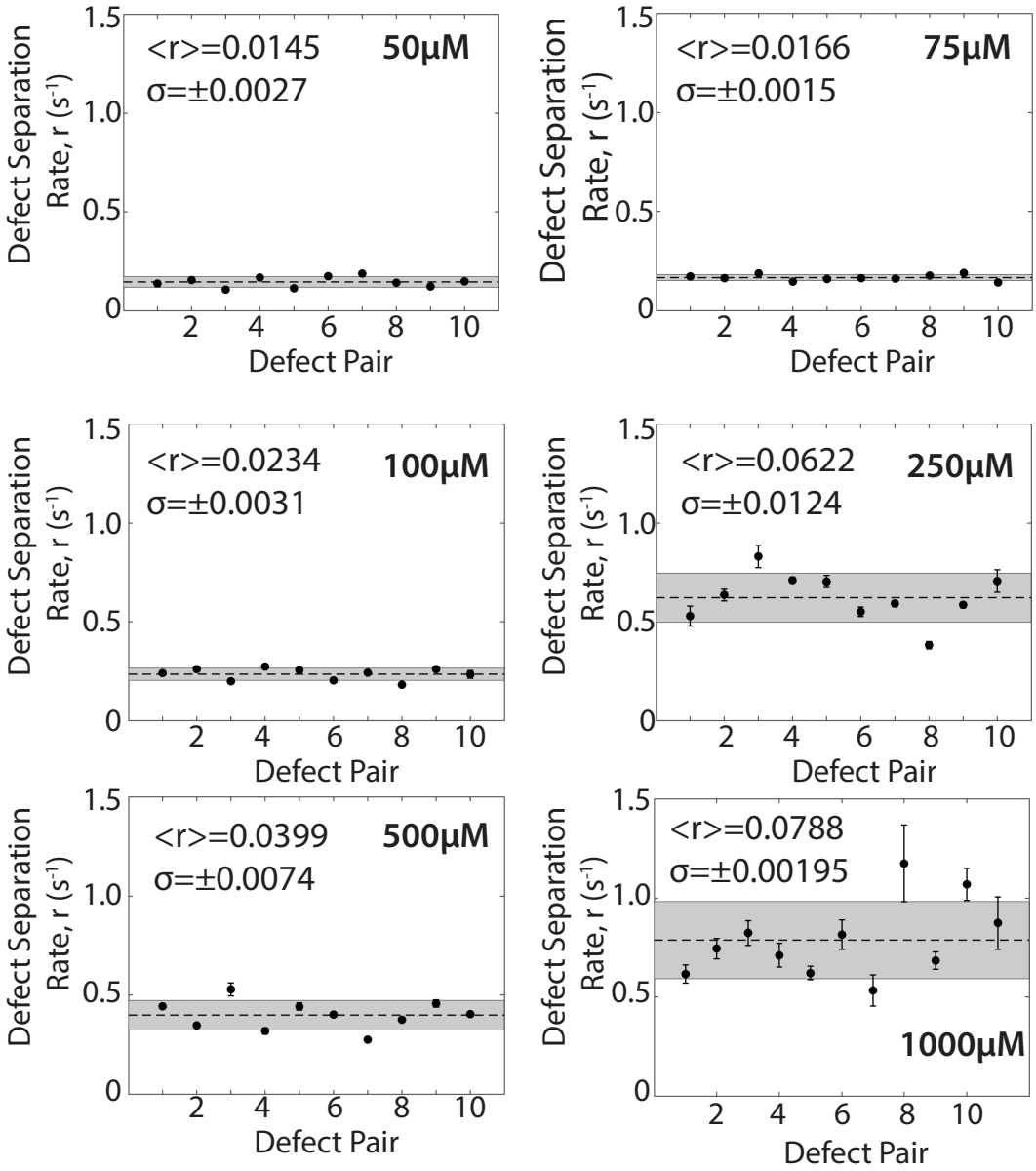

Fig. 4.11) Defect separation rate, r (s^{-1}), of defect pairs for ATP concentrations ranging from 50μM to 1000μM. The average separation rate, <r> is shown by the dashed line, and the standard deviation, σ, is denoted by the gray shaded region. The error bars on each defect pair are from the goodness of fit from the semi-log plots. (reproduced from Tan et al, 2019 with permission ©2019 Springer Nature)

We calculated the topological entropy, *h*, from the bead separation rates as described in Section 4.3.2. Fig. 4.12 shows the topological entropy as a function of ATP concentration. There is a non-monotonic relationship between h_{beads} and ATP, that has a general increasing trend. To understand this relationship, we considered how the length-scale in the active nematic system varies with activity based on a balance between elastic

bend energy and activity. We calculated the active length scale following Hemingway et al.[62] by calculating the velocity-velocity correlation function and measuring the length at which the correlation function drops to 1/2. Fig. 4.13 shows the length-scale as a function of ATP. The length-scale for the range of ATP concentrations is roughly constant as consistent with the work done by Lemma et al.[61] where they showed the length-scale does not show significant changes in the length-scale until ATP concentrations are below 10μM. The minor fluctuations in length-scale can be attributed to slight variations in microtubule length from sample to sample. Fig. 4.14 shows the slight variation in length-scales between an image from 50 μM and 1000 μM. It is possible this slight variation arises from microtubule shearing when we pipette the sample.

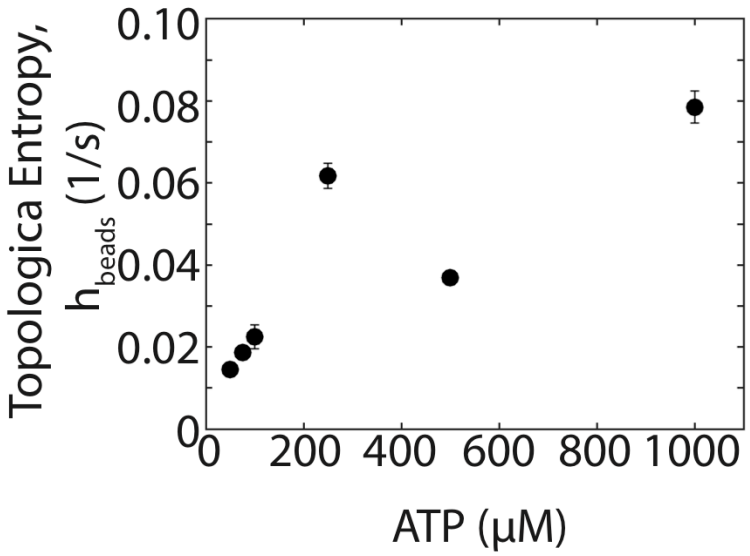

Fig. 4.12) Topological entropy for bead pair separation as a function of ATP concentration. (reproduced from Tan et al, 2019 with permission ©2019 Springer Nature)

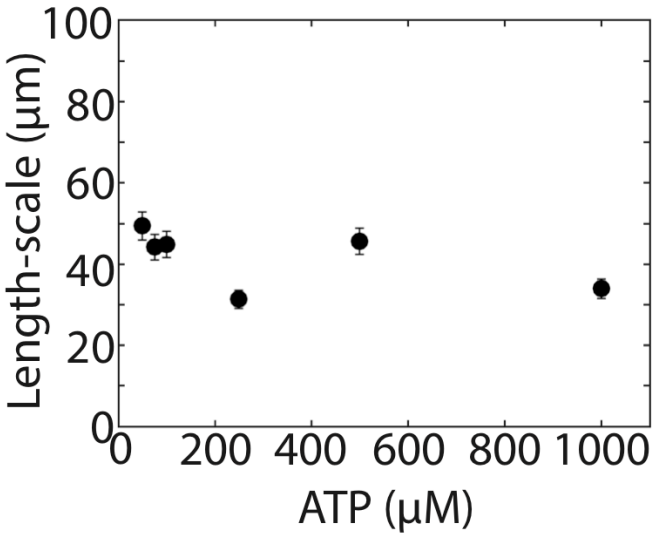

Fig. 4.13) Length-scale between defects as a function of ATP concentration. Length-scale is calculated from velocity-velocity correlation from PIV analysis. (reproduced from Tan et al, 2019 with permission ©2019 Springer Nature)

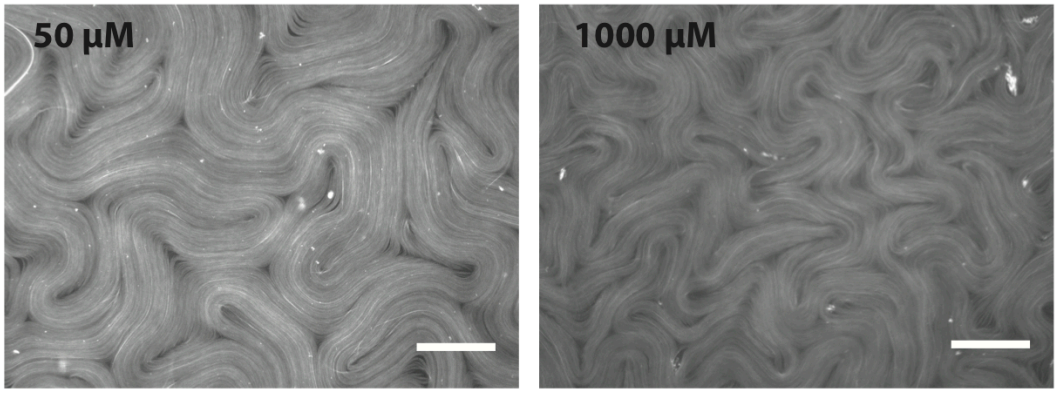

Fig. 4.14) Fluorescence microscopy image of variation in length-scale between defects between 50μM and 1000μM. Scale bars, 100μm

Prior work has shown microtubule length distributions can be tuned via shearing through a syringe[1]. We tested the effects of shearing on the active network by shearing the microtubules through a syringe prior to assembly into a network. Fig. 4.15a and Fig. 4.15c shows the difference in length-scales in the 2D active nematic network from non-sheared microtubules as the control and microtubules that have been sheared three times. Visibly, there is a difference in the length-scale between defects, which is consistent with the length calculated from the velocity-velocity correlation shown in Fig. 4.15b and Fig. 4.15d. This result shows that there can be minor variations in the microtubule lengths from shearing,

which can ultimately change the length-scale between defects in the 2D active nematic from sample to sample.

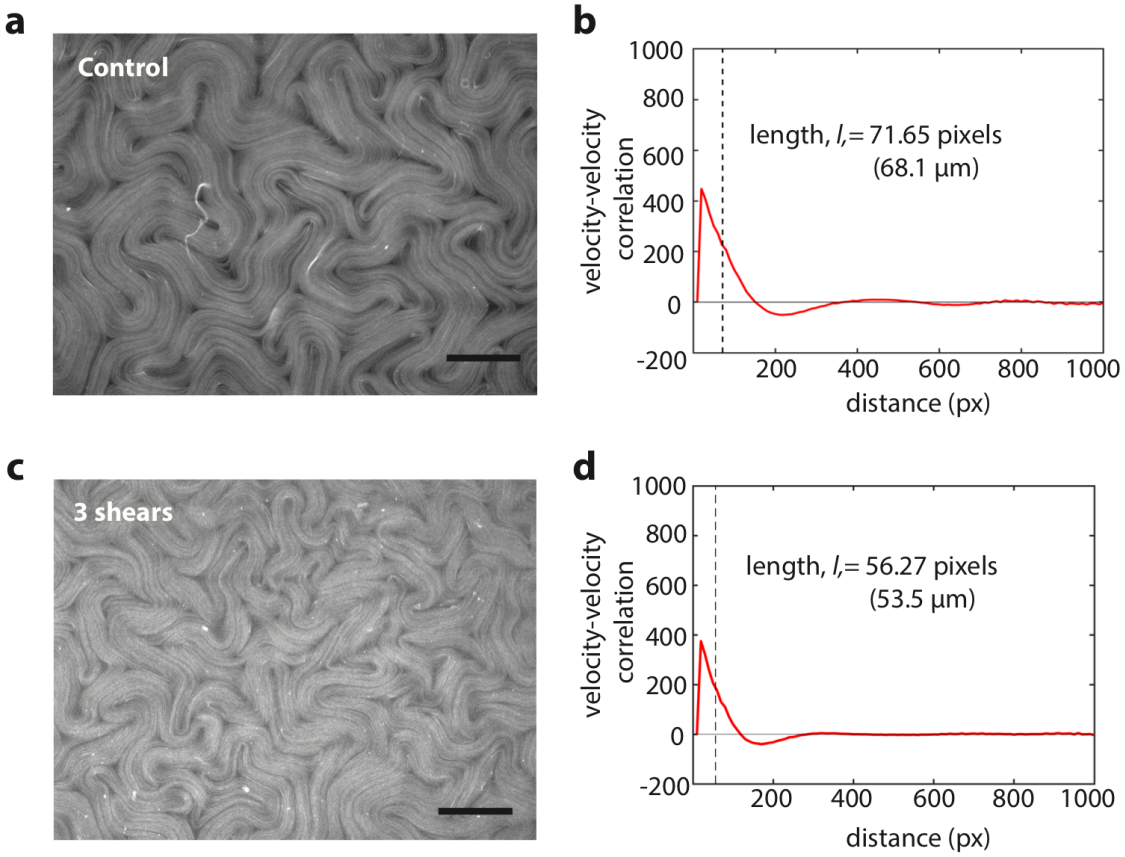

Fig. 4.15) Change in length-scale between defects after shearing a) Fluorescence microscope image of microtubules in the 2D active network before shearing. Scale bar, 200µm. b) Velocity-velocity correlation as a function of distance. Correlation length, l=68.1µm . c) Fluorescence microscopy image of 2D active network after microtubules are sheared three times. Scale bar, 200µm d) Corresponding velocity-velocity correlation as a function of distance. Correlation length, l=53.5 µm.

Considering the changes in length-scale, we calculate a characteristic timescale for each ATP concentration. The characteristic timescale, τ, is defined as

$$\tau = \frac{l}{v_{rms}}$$

where l is the length-scale, and v_{rms} is the network velocity. We use τ to rescale h_{bead} to h', which will provide insight to the overall mixing behavior of the system removing

contributions from fluctuations in the length or velocity. *h'* results in a measure of topological entropy that only depends on the geometry of the flow.

Fig. 4.16 shows h_{beads}' as a function ATP concentration. Remarkably, the nondimensionalized h_{beads}, h_{beads}', results in a fairly constant value for all ATP concentrations. This result indicates h_{beads}' is insensitive to changes in the input energy and the geometry of the flow is the same.

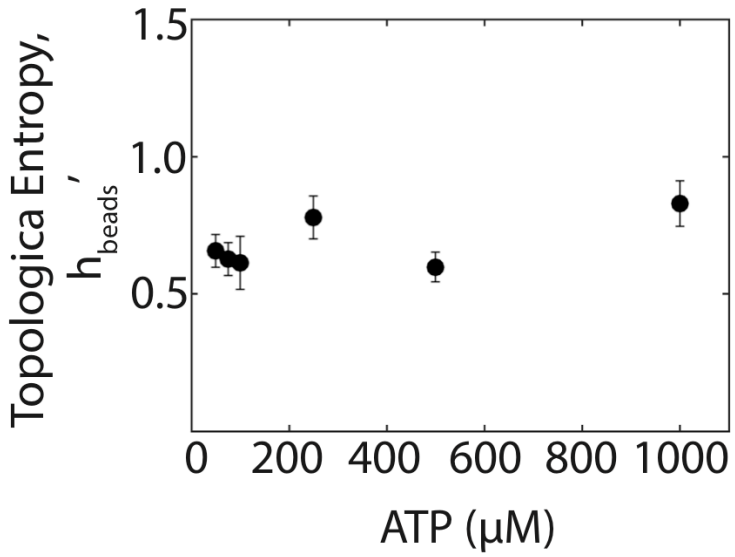

Fig. 4.16) Nondimensionalized topological entropy for bead separation. The topological entropy, *h'*, was nondimensionalized by a time-scale, $\tau = l / V_{rms}$ (for each ATP concentration). The error bar is the weighted standard error of the mean. (reproduced from Tan et al, 2019 with permission ©2019 Springer Nature)

The same analysis was done for defect pair separations as a confirmation of the behavior we observed for bead separation. Fig. 4.17a shows $h_{defects}$ as a function of ATP concentration and the dimensionless $h_{defects}'$ in Fig. 4.17b shows $h_{defects}$ as a function of ATP is in strong agreement with h_{beads}. Again, $h_{defects}'$, results in a constant value for all ATP concentrations. These two independent measures of local stretching given similar resulting trends both for *h* and *h'*. In all cases, *h* is a positive value indicating signs of chaos in the active fluid.

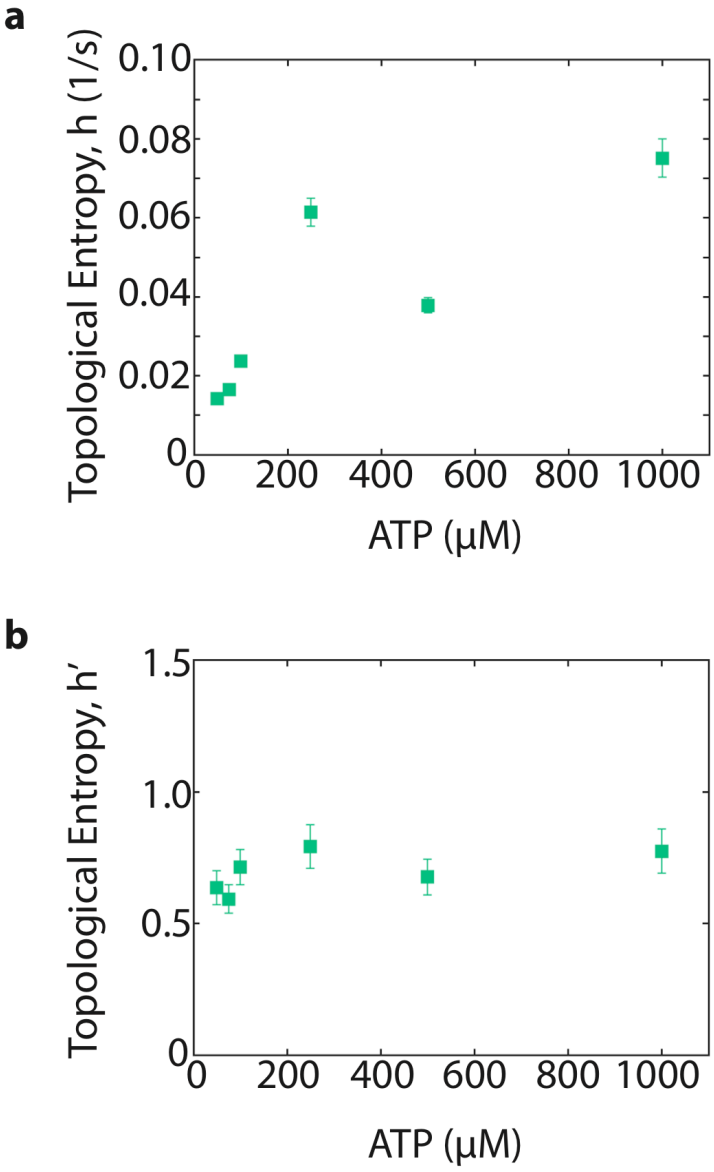

Fig. 4.17) Topological entropy measured for defect pair separation. a) Topological entropy, *h* (s^{-1}) as a function of ATP concentration. b) Nondimensionalized topological entropy, *h'*, as a function of time.

4.3.5 Measures of global mixing

To further measure the robustness of the topological entropy, we measured the topological entropy from global mixing. In this situation, we considered the topological defects to be virtual stirring rods and use the concepts from braid theory as developed by Thiffeault *et al*[80]. As the defects move within the fluid, they drag the "fluid" (i.e.

microtubules) with it. The first question to answer is do the topological defects braid around each other, and if so, do the defects generate topological entropy? Fig. 4.18a shows the trajectory of five defects over time do braid around one another. To explore this behavior, we implemented an algorithm called "Ensemble-based Topological Entropy Calculation" (ETEC) to calculate a lower bound for the topological entropy for two-dimensional systems[97].

ETEC is a method developed by Roberts et al.[97] that uses computational geometry to track the evolution of a rubber band that is continuously stretched and folded as data points move and cross it. The data points in our system would be the tracked defects. We use the defect trajectory data from the defect tracking algorithm and create an initial mesh connecting the defects at an initial state. The initial state of the mesh is shown in Fig. 4.18b. As the defects evolve, and wrap around each other, they pass through lines connecting the mesh. The number of line segments connecting the defects grows as the mesh is deformed as shown in Fig. 4.18c. The method keeps track of the growing number of line segments within the mesh as it's deformed. The evolved mesh is a measure of how the defects wrap around each other. Fig. 4.18d shows the semi-log plot of the growing number of line segments as a function of time. The slope gives a measure for the lower bound on the topological entropy.

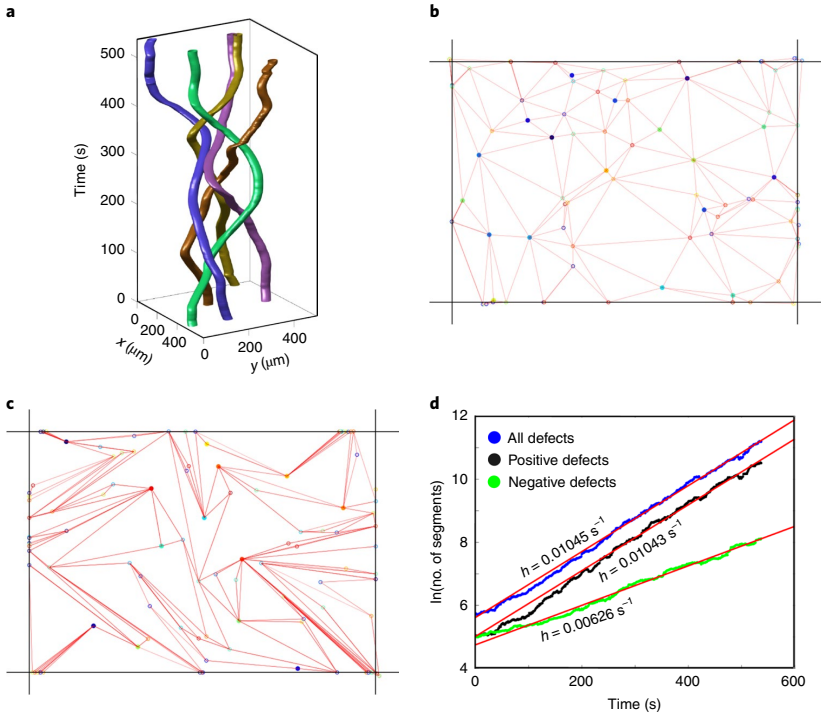

Fig. 4.18) Defect braiding using ETEC (50μM data set) a) An example of five defects' trajectories as a function of time showing defect braiding. b) Rubber band mesh connecting defects at their initial state. c) Final state of the rubber band mesh after defects have evolved. The thickness of the lines indicates the weight of the line. d) Semi-log plot of the number of line segments as a function of time for all defects (blue), positive defects (black), and negative defects (green), with h_{all}=0.01045 s^{-1}, h_{+}=0.01043 s^{-1}, and h_{-}=0.00626 s^{-1}. (reproduced from Tan et al, 2019 with permission ©2019 Springer Nature)

One challenge of ETEC is it requires the trajectories to stay in the field of view for the length of the movie. Since the ±1/2 defects are active, they constantly emerge and annihilate, which means the tracked defects also disappear and emerge. To circumvent this issue, when the defects disappear, the algorithm creates a "ghost defect" that becomes passively advected by the flow field. The flow field is calculated from PIV. Using the trajectories from the 50μM data of all the defects yielded a positive h_{all} = 0.0145 s^{-1}, which is in close agreement to h_{beads} and h_{defect}. This result is evidence that the measures of local stretching match the quantity measured from global mixing. In this active fluid, the +1/2 defects are propelled actively through the fluid, whereas the -1/2 defects are passively advected. When ETEC was used only consider the +1/2 defects, h_{+}=0.0145 s^{-1}, which is close to the value measured when all defects were considered. When the -1/2 defects only were considered, h_{-}=0.00626 s^{-1}, which is almost half of h_{all}. This result means the +1/2 defects are generating all the topological entropy in the system and are responsible for the majority of the braiding.

4.3.6 Nondimensionalized topological entropy for all methods

Now with established methods of measuring the complexity of the active fluid, both with local stretching and global mixing, we compared *h'*, for all methods. One additional quantity that we considered is the Lyapunov exponent, λ, which we directly compute by taking the gradient of the velocity field:

$$\lambda = \nabla v$$

where λ is the Lyapunov exponent, and v is the velocity field computed from PIV. For the 50 μM data set, λ=0.0120(±0.0006) s^{-1}, which is in agreement with the other methods.

Fig. 4.19 compares the nondimensionalized value for all the four methods. Shockingly, all the methods result in a relatively constant value. h_{brad}' is consistently lower than all the other methods, which is makes sense because ETEC computes a lower bound for the topological entropy. Additionally, the braiding technique inherently gives a lower value because the braiding of rods may not always capture the entirety of the mixing dynamics. Braiding may not consider secondary folds in the fluid. Overall, *h'*, is a quantity that is insensitive to changes in activity, which may mean that the underly geometry of the flow could be a universal quantity that can be applied to other active fluid-like systems.

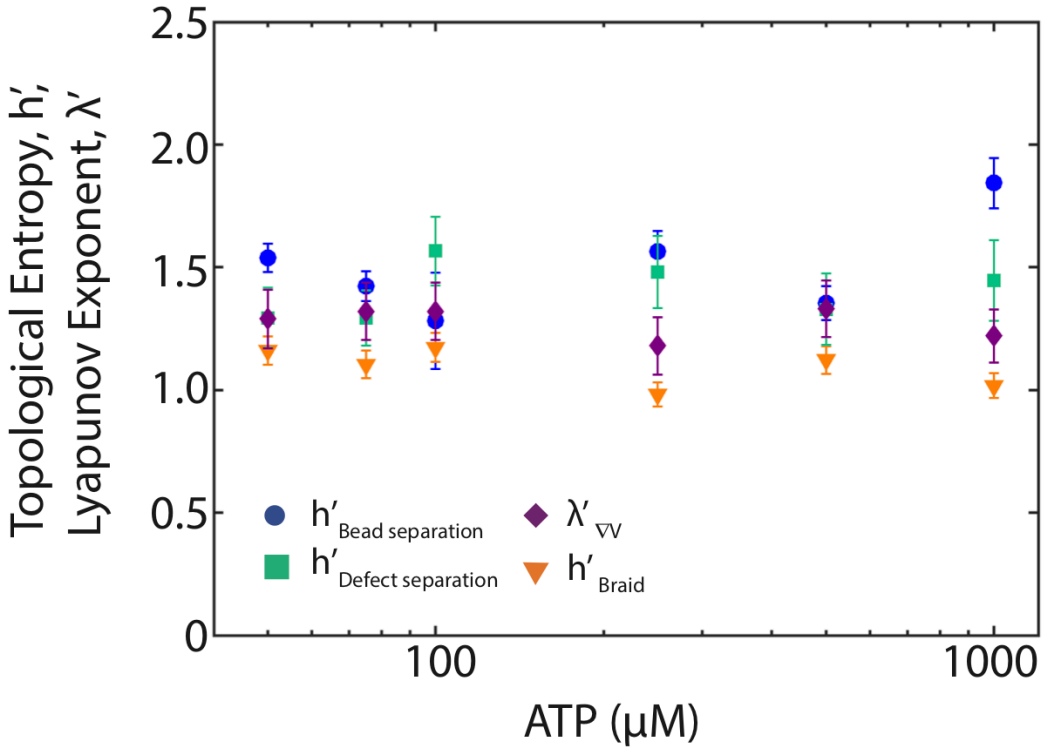

Fig. 4.19) Nondimensionalized topological entropy, *h'*, and Lyapunov exponent, *λ,* as a function of ATP compared for bead separation (blue circle), defect separation (green square), defect braiding (orange triangle), and the Lyapunov exponent, λ (purple diamond). (reproduced from Tan et al, 2019 with permission ©2019 Springer Nature)

4.4 Conclusions

Until now, the active nematic fluid flows have not been view through the lens of chaotic dynamics. This work has introduced a new method to quantify the complexities of this self-mixing active fluid. We compared three methods of measuring topological entropy and the Lyapunov exponent and find all methods are in agreement, which is evidence for how robust the measures of chaos are in this system. Measures of defect braiding shows positive defects were responsible for generating all the topological entropy in the system and were the main "rods" creating braids in the fluid, whereas negative defects contribute little, if any, topological entropy. The consistency in topological entropy for local stretching and defect braiding may imply the local stretching on the microscale gives rise to the large-scale defect motion.

Varying the energy available to the system resulted in a general increase in topological entropy, but the most shocking outcome is the nondimensionalized topological entropy and nondimensionalized Lyapunov exponent are insensitive to changes in local

energy injection. This may imply that this is a universal quantity that describes the underlying geometric dynamics in the active fluid.

Overall, this work introduced new concepts applicable to a 2D active nematic network, and may be applicable to other active fluids composed of self-propelled particles Further work must be done to explore the universality of the dimensionless quantities.

Acknowledgements

Thank you to Marc Ridilla from the Brandeis MRSEC group and Linnea Lemma from Zvonimir Dogic's group for purifying and polymerizing microtubules, purifying kinesin motors, and preparing the premixture and microtubules for the experiments. Thank you to Eric Roberts, Spencer Smith, and Kevin Mitchell for the work done on defect tracking and defect braiding using ETEC. Thank you to Jorge Artega, Ulysses Alvarado, and Sam Fortini for their contributions with defect separation analysis.

Chapter 5: Biological active nematic in viscous environments

In this chapter, I will discuss the mixing dynamics of the microtubule-kinesin active nematic in contact with different oil viscosities. This work extends on the project discussed in Chapter 4. Dynamical and defect morphology changes with different oil viscosities. These changes in the network represent the material's response to external changes in its environment. In this chapter, I discuss our work exploring how the mixing dynamics respond to external changes to the active nematics' environment.

5.1 Introduction

Active matter systems constantly convert chemical energy into motion. Biological systems are a class of active matter that includes cellular tissues, bacterial colonies, and proteins, such as molecular motors and filaments. Each cell, bacterium, or protein operates as machines converting chemical energy from its environment to mechanical work. Often in biology, processes occur in complex environments, so it is important to understand how these entities navigate through and collectively behave in viscous environments. For example, certain bacteria have been shown to retain motility even in highly viscous environments, whereas other types of bacteria can be immobilized at much lower viscosities[98]. Another example is bovine sperm, which have exhibited collective swimming in viscoelastic environments[99].

The microtubule/kinesin based extensile active network has been an exciting material to study with rich dynamics to uncover. In 2D, the active network forms an active nematic with flows self-generated by moving topological defects. Guillamat et al. probes the shear viscosity of the active nematic by designing an experimental setup that allows them to vary the viscosity of the bounding oil over five magnitudes[100]. This group observed drastic changes in active nematic morphology and dynamics with increasing viscosity. Fig. 5.1 shows fluorescence confocal micrographs of the active nematic at varying viscosities over five orders of magnitude by Guillamat et al. In addition to the qualitative differences in the morphology of the active nematic, the network velocity decreased with increasing viscosity, and the number defect density increased with increasing viscosity[100]. What was not addressed in this work was how these changes affect the generated fluid flows.

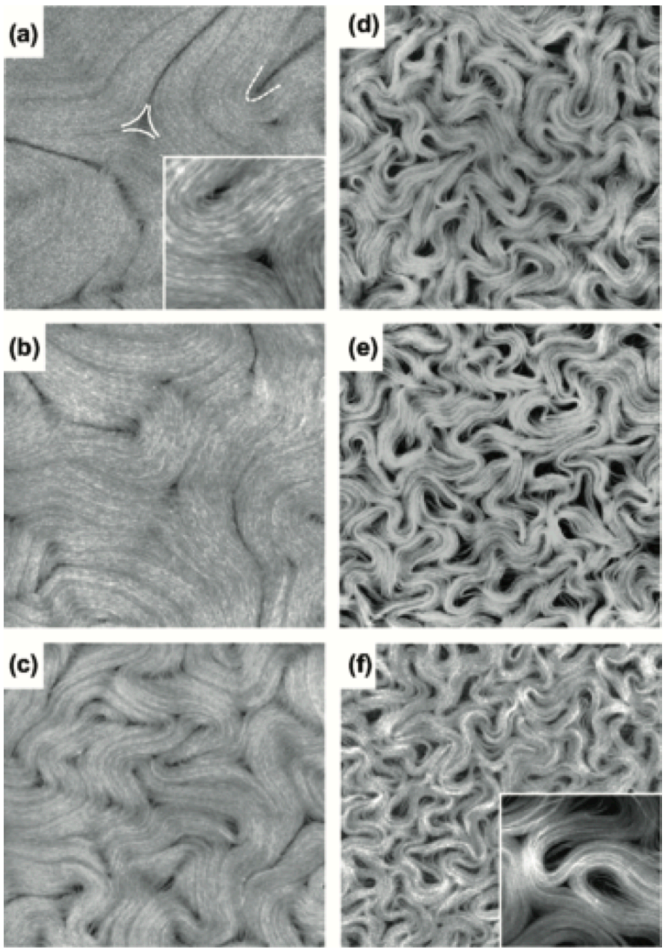

Fig. 5.1) Fluorescence confocal micrographs of active nematic in varying viscosities of oils. The viscosities of oils vary from a) 5 mPa s, b) 50 mPa s, c) 500mPa s, d) 5000 mPa s, e) 12,500 mPa s, and f) 300,000 mPa s. The width of the image is 400 μm. (reproduced from Guillamat et al. 2016 with permission ©2016 American Physical Society)

In our previous work, we characterized the flows within the active network as chaotic where the fluid material (microtubules) exhibited exponential stretching as discussed in Chapter 4[101]. We observed the dimensionless topological entropy remained constant across three independent measures of chaos and was in agreement with the dimensionless Lyapunov exponent[101]. These quantities were also insensitive to changes in the input energy in the system[101]. To understand the potential universality of this quantity, we next investigated the mixing dynamics of the same active fluid in viscous environments. Changing the viscosity of oil of which the active fluid is in contact with is a method to study how the active fluid behaves in response to external changes.

In this experiment, we used an experimental setup adapted from Guillamat et al. where a polydimethylsiloxane (PDMS) well is glued onto a polyacrylamide coverslip[100]. The well is filled with silicon oils of varying viscosity and the active microtubule network

is injected at the bottom of the well to wet the surface in 2D at a water/oil interface. Since the oil is now on top of the sample, an analogy to the changes in viscosity is the virtual stirring rods (active defects) of the active nematic are now trying to mix a fluid like honey. Will the dynamics in the active fluid change in response to its environment?

5.2 Experimental Methods

5.2.1 PDMS well construction

To create a PDMS well, we combine 0.1g Sylgard 184 Elasomer curing agent and 1g Sylgard184 Elastomer base in a plastic weigh boat and mix until milky white with bubbles. The mixture is placed in a desiccator to degas for ~1 hour until all bubbles have disappeared. A glass slide is cleaned with acetone, methanol and ethanol and placed in the middle of a piece of masking tape such that tape is visible on all outside edges of the glass slide. The edges of the tape are folded such that the tape forms walls on all four sides of the glass slide. The PDMS mixture is poured into the glass-slide well (~1-2mm thick) and the well is set on a hot plate at 65°C until fully cured. Once the PDMS is cured, small blocks of PDMS are cut using a razor blade. A 5mm diameter hole is punched in the center.

The PDMS well is cleaned with isopropyl alcohol and ddH_2O. Acrylamide coated coverslips as described in the Appendix (A.5) are previously prepared, rinsed with ddH_2O and left to air dry. A pipette tip is used to place UV-curable glue (RapidFix) onto the bottom of the PDMS well and then placed onto the dried coverslip. A UV light is used to cure the glue, so the well is stuck onto the coverslip.

5.2.2 Rheological measures of silicon oil mixtures

We use the Stresstech HR Rheometer to measure the viscosity of our silicon oil and silicon oil mixtures. We use commercial silicon oil (Elkem silicon oil) with a viscosity of 350 mPa s, and 1000 mPa s. We create intermediate silicon oil mixtures from the commercial oils at 70% 350 mPa s/ 30% 1000 mPa s (v/v%), 50% 350 mPa s/ 50% 1000 mPa s (v/v%), and 30% 350 mPa s/ 70% 1000 mPa s (v/v%). We measure the viscosity for all silicon oil samples with the rheometer with two settings: varying stress with constant temperature, and varying temperature with constant stress. We vary the stress from 2-10 Pa while maintaining the temperature at 25°C. We vary the temperature from 18°C-28°C while maintain a constant stress, 2.5 Pa for 350mPa s, 70% 350 mPa s/30% 1000 mPa s, 5 Pa for 50% 350 mPa s/50% 1000 mPa s and 30% 350 mPa s/70% 1000 mPa s, and 6 Pa for 1000mPa s. We determine the viscosity of the oil and oil mixtures by averaging the viscosity measured for temperatures between 20°C and 25°C to account for temperature fluctuations in lab.

5.2.3 Sample preparation

Fig. 5.2 shows the experimental setup of the silicon oil well. To prepare the active network, we prepare the active premix that is described in the Appendix (A.8) with 1mM

ATP concentration and add 2µl of GMPCPP microtubules. While the active network forms, the PDMS well is filled with 60µl of silicon oil ranging from 382.2 mPa s to 1144 mPa s. Then, 0.75µl of the active network is injected to the bottom of the PDMS well to allow the network to wet the bottom surface. The network is left to settle to the oil/water interface for about 30 min to 1 hour.

5.2.4 Image and analysis

Once samples have settled, we image using (Leica DMP) fluorescence microscope and Hamamatsu ORCA-flash 4.0 LT CMOS camera. Image sequences were taken with 500 ms exposure and 500 ms intervals between frames for 600 frames.

We manually trace the growth of the contour length as defect pairs separate as taken from Tan et al. [101]. We generate a velocity field of the active network using PIV analysis, from PIVlab in Matlab. We generate a velocity fields for three to four cropped sections of the field of view sized 800x800 pixels. We used cropped sections to avoid tubulin aggregates diffusing in the field of view that may affect the velocity field calculation. We quantify the characteristic length scale, or length scale between defects, as the distance where the velocity-velocity correlation function = 1/2 as done previously[62,101,102].

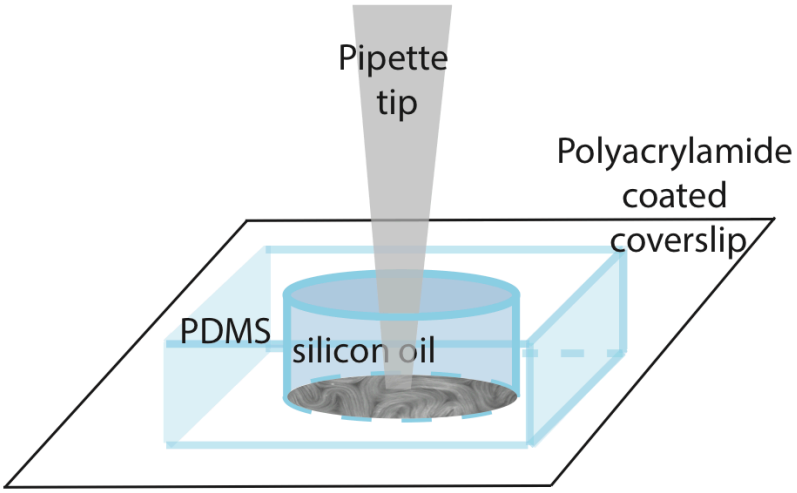

Fig. 5.2) Schematic of experimental setup. A hole is punched in a PDMS block to create a well and the PDMS block is glued onto a polyacrylamide coated coverslip. The well is filled with silicon oil and the active network is injected at the bottom of the coverslip.

5.3 Results

5.3.1 Measures of viscosity for mixtures of silicon oil

We used a mixtures of commercial silicon oil with viscosity 350 mPa s and 1000 mPa s to get intermediate viscosities. First, we measured the viscosity of the oil mixtures at a constant temperature of 25°C and varying stress applied to the fluid. The stress applied is given by a constant torque applied to the fluid. We applied a range of applied stress to each silicon oil and measured the viscosity. Fig. 5.3 shows the viscosity as a function of varying applied stress. For the given applied stress, the viscosity remained constant for all oils. This measurement is to ensure that the silicon oil behaves as a Newtonian fluid.

The flow behavior of Newtonian fluids is described by a linear relation between shear stress and shear rate and the proportionality constant is the viscosity. Shear stress on an object occurs when a force is applied to a material parallel to a cross-sectional area of the object[33]. Shear rate is the rate at which the shear stress deformation occurs on an object. This linear relationship between shear stress and shear rate is defined as

$$\tau_s = \eta \cdot \gamma$$

where τ_s is the shear stress, γ is the shear rate and η is the viscosity.

Next, we measured the viscosity of the oils as a function of temperature. We applied a constant applied stress and vary the temperature from 18°C to 28°C. We chose this range for the temperature to account for temperature fluctuations in the lab. Fig. 5.4 shows the viscosity as a function of temperature for all silicon oil samples. The viscosity of the oil shows a slight decrease with increasing temperature for all oil samples. The temperature fluctuations in the lab range from 20°C to 25°C, we define the viscosity of the oil as the average viscosity measured from 20°C to 25°C. Table 4.1 below contains the results of the average viscosities for the silicon oil mixtures.

Table 4.1) Measured viscosities for silicon oil mixtures. The reported error is the standard error of the mean.

Silicon Oil Mixture	**Average viscosity, $\langle\eta\rangle_{20°C\text{-}25°C}$**
350 mPa s	382.2 (±6.4) mPa s
70% 350 mPa s 30% 1000 mPa s	554.2 (±9.1) mPa s
50% 350 mPa s 50% 1000 mPa s	685.6 (±11.7) mPa s
30% 350 mPa s 70% 1000 mPa s	939.4 (±16.4) mPa s
1000 mPa s	1144 (±19.2) mPa s

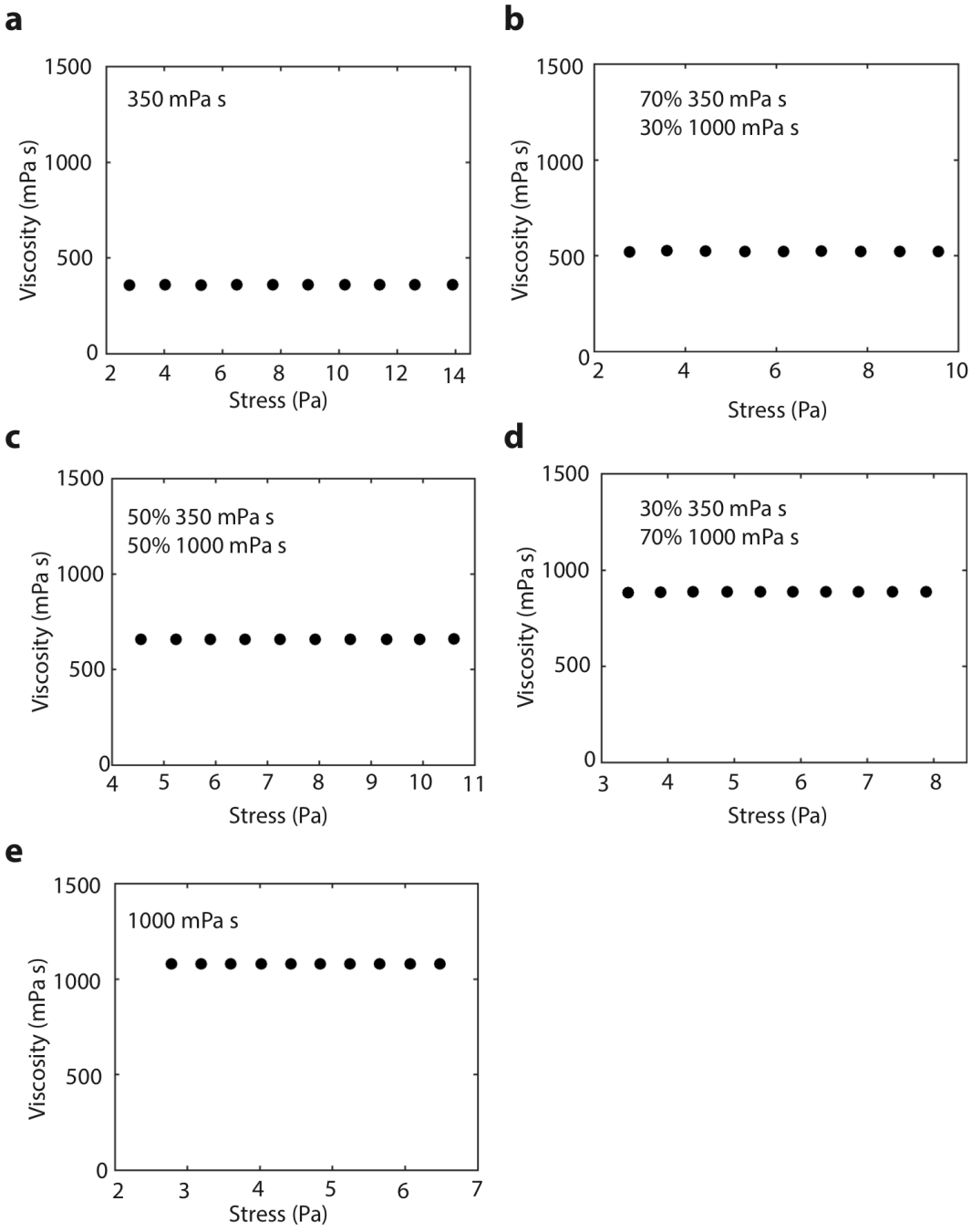

Fig. 5.3) Silicon oil viscosity as a function of stress. The viscosity is measured for silicon oil with viscosity a) 350 mPa s, b) 70% 350mPa s/30% 1000mPa s, c) 50% 350mPa s/50% 1000mPa s, d) 30% 350mPa s/70% 1000mPa s, and e) 1000 mPa s of varying stress at a constant temperature of 25°C.

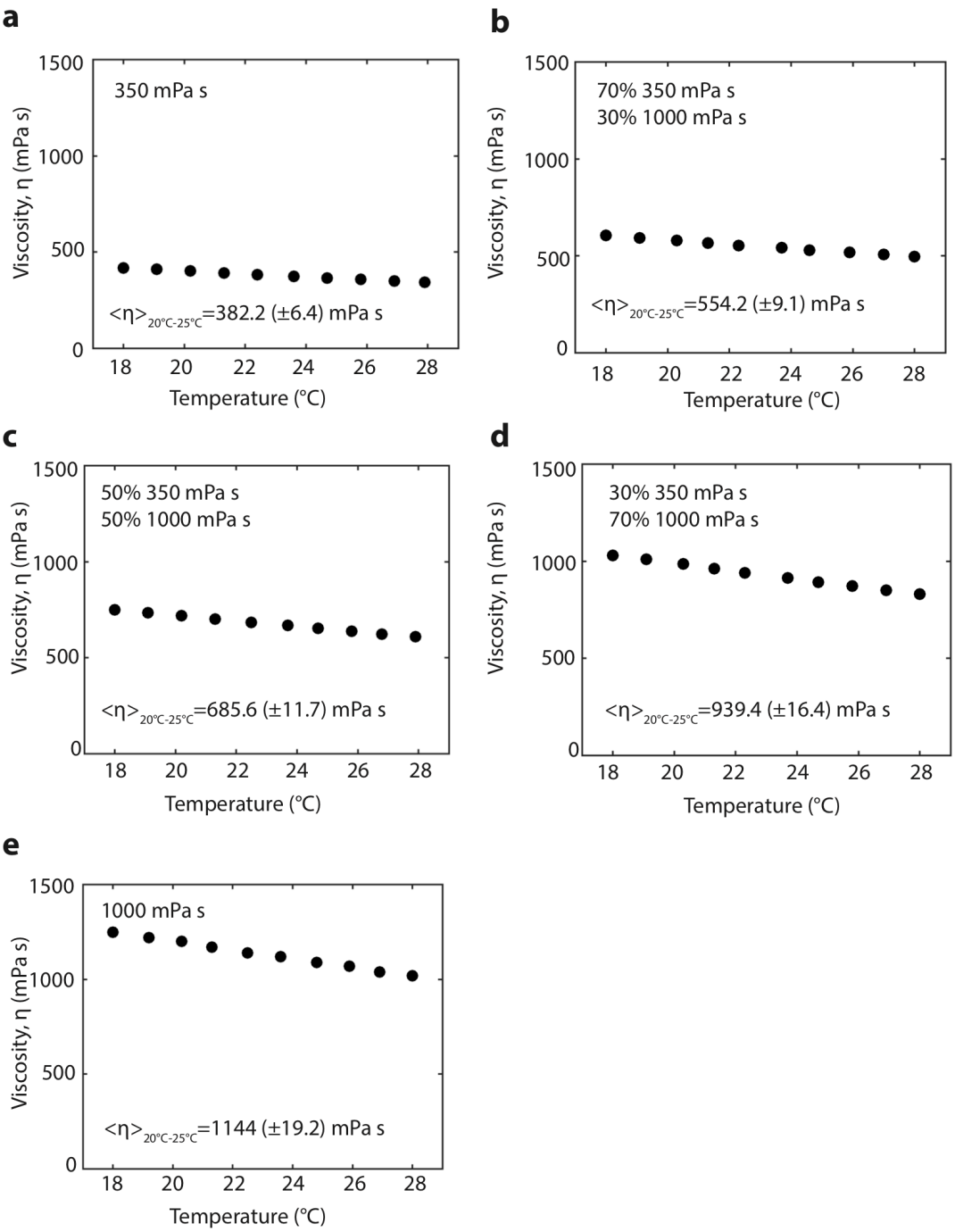

Fig. 5.4) Viscosity of silicon oil as a function of temperature. The viscosity, η, is measured for silicon oil a) 350 mPa s with a constant stress 2.5 Pa, b) 70% 350mPa s/30% 1000mPa s with constant stress 2.5 Pa, c) 50% 350mPa s/50% 1000mPa s with constant stress 5 Pa, d) 30% 350mPa s/70% 1000mPa s with constant stress 5 Pa, and e) 1000 mPa s with constant stress 6 Pa varying temperature from 18°C to 28°C. The average η, <η>, is averaged over 20°C-25°C to account for temperature fluctuations in lab. The error is the standard error of the mean.

5.3.2 Defect stretching in different viscous environments

The PDMS well was filled with silicon oil of varying viscosities. The active microtubule network was injected at the bottom of the well and allowed to sediment at the oil/water interface. In Fig. 5.5, we show fluorescence images of the active nematic in contact with oil of increasing viscosity. In this experimental geometry with different viscous environments, we observed qualitative differences in the defects compared to the previous setup where the active network was suspended at an oil water interface with the oil under the sample[4,101]. We observed defect fracturing forming disclination lines. Fig. 5.6 shows an example of a defect fracture. In the case of a fracturing defect, intermediate defects in between the head and tail of the separating defect pair during creation (as shown in Fig. 5.6b). As the defect propels forward, the intermediate defects annihilate and merge together. All the intermediate defects merge into a disclination line. We observed more frequent examples of defect fracturing and line formation when the active fluid is in these viscous environments as compared to the case where the active fluid is suspended at an oil/water interface.

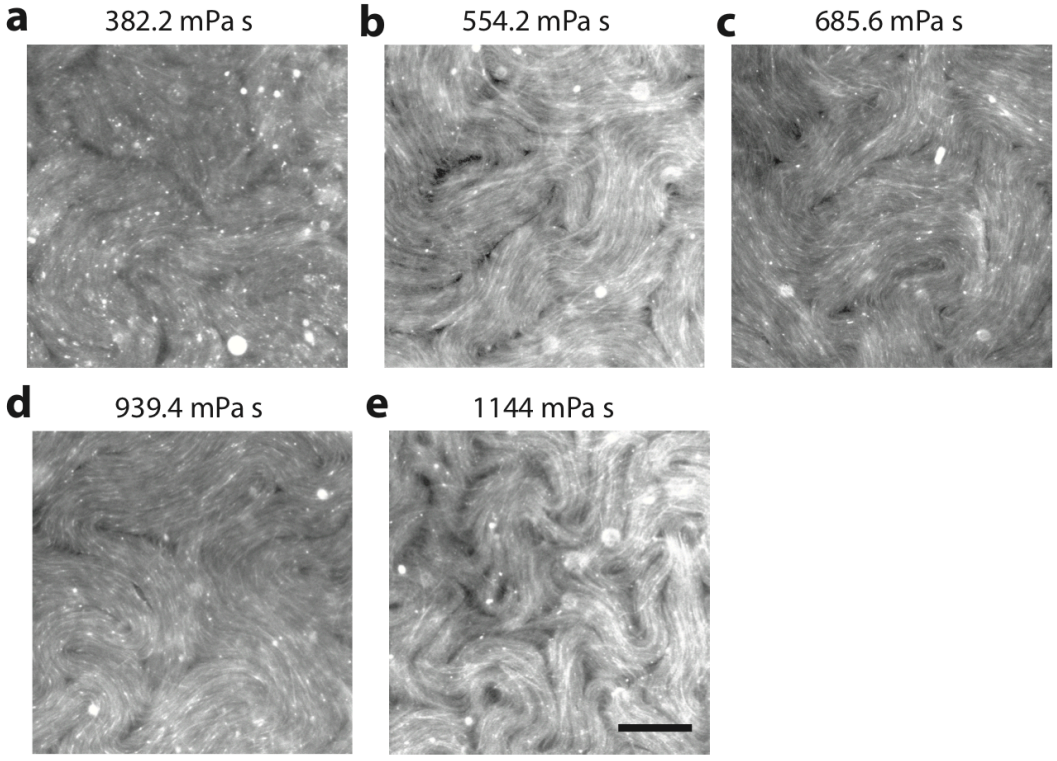

Fig. 5.5) Fluorescence microscope images of active nematic fluid in viscous environments. The viscosity of the oil varies from a) 382.2mPa s, b) 554.2 mPa s, c) 685.6 mPa s d) 939.4 mPa s, e) 1144 mPa s. Scale bar, 100 μm.

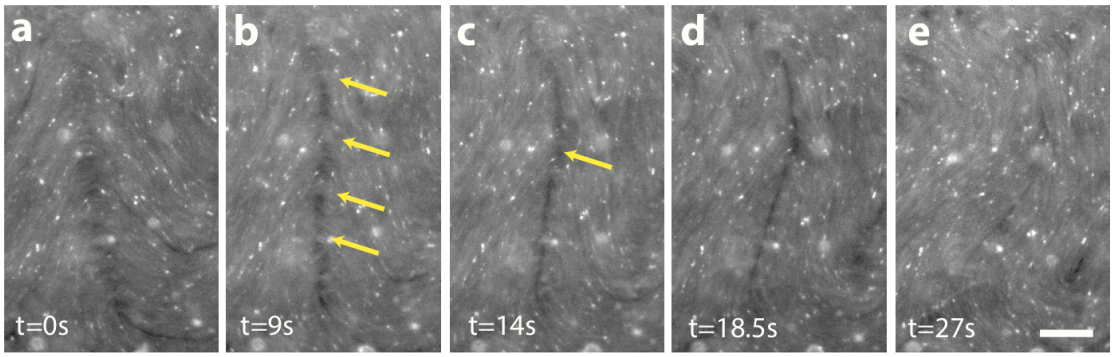

Fig. 5.6) Image sequence of defect fracturing. a) Initial +1/2 defect emerges at t=0. b) Multiple intermediate +1/2 defects form (indicated by the yellow arrows) as the defect propels forward, resembling fracturing at t=9s. c) Intermediate defects merge, with some intermediate defects remaining (yellow arrow) at t=14s. d) Disclination line forms after intermediate defects merge at t=18.5s. e) Defect line disappears at t=27s. Scale bar, 50 μm

We observed nonmonotonic changes in the V_{rms} of the fluid varying the viscosity of the oil that is in contact with the active fluid as shown in Fig. 5.7. The length-scale between defects remained fairly constant except for a slight decrease at the highest viscosity of 1144(±19.2) mPa s shown in Fig. 5.8. Our results are different from those observed in Guillamat et al.[100] where they observe a decrease in velocity and length-scale with increasing viscosity. The reason for this discrepancy may be that Guillamat et al. used varying viscosities over six decades, whereas in our experiments, we focus on a narrow range of viscosities ranging from ~300-1200 mPa s. Our results show the intermediate changes in velocity and length-scale for this specific range.

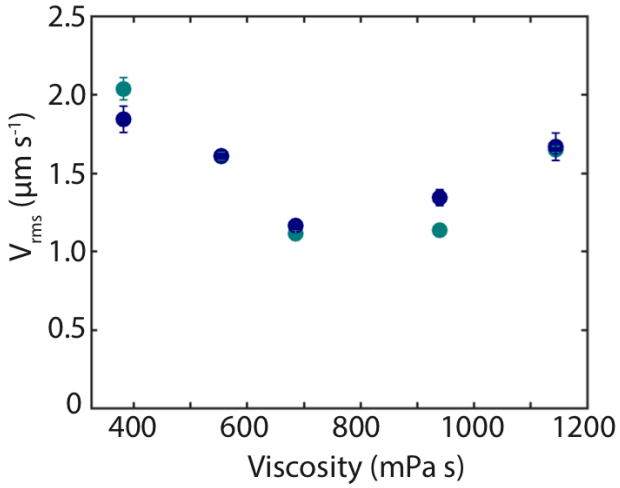

Fig. 5.7) V_{rms} of the active fluid as a function of viscosity. The average V_{rms} shown for run 1 (dark blue) and run 2 (teal). V_{rms} shown here is the average V_{rms} calculated from PIV analysis of cropped sections of the field of view. The error is the standard error of the mean.

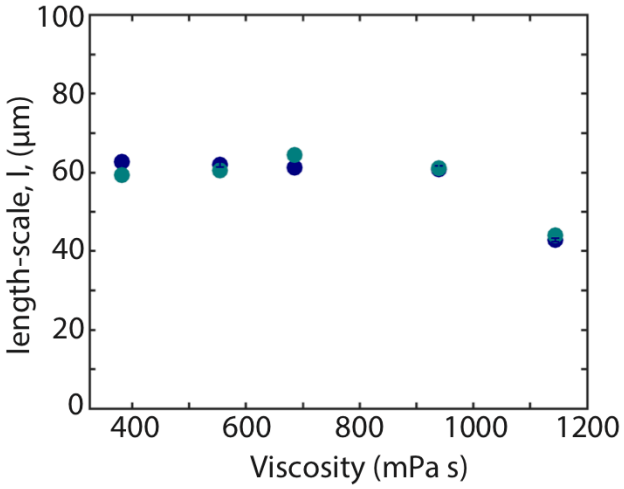

Fig. 5.8) Characteristic length-scale as a function of viscosity. The characteristic length-scale, or length-scale between defects for run 1 (dark blue) and run 2 (teal). The length-scale, l, is calculated by the distance, r, at which the velocity-velocity correlation function, C(r)=1/2. The error on the length-scale is defined as 5% of the length.

We measured the separation rate of defect pairs for all viscosities. There are two runs for each viscosity. The two runs are taken ~10 minutes apart from the same sample. We manually traced the growing contour length connecting the defect pair as they separate away from each other. Fig. 5.9a shows a time-lapse of a defect pair stretching in η=939.4 (±16.4) mPa s, where the yellow line is the traced contour length. Fig. 5.9b is the corresponding semi-log plot of the contour length as a function of time with separation

rate, r=0.024 s^{-1}. The semi-log plot shows an exponential relationship between the growing contour length, d, over time. This result indicates the active fluid under viscous environments exhibits exponential stretching. Despite the difference in geometry of the experimental setup, and the viscosity of the oil of which the active fluid is in contact with, the active fluid still exhibits the exponential stretching observed previously in ref[101].

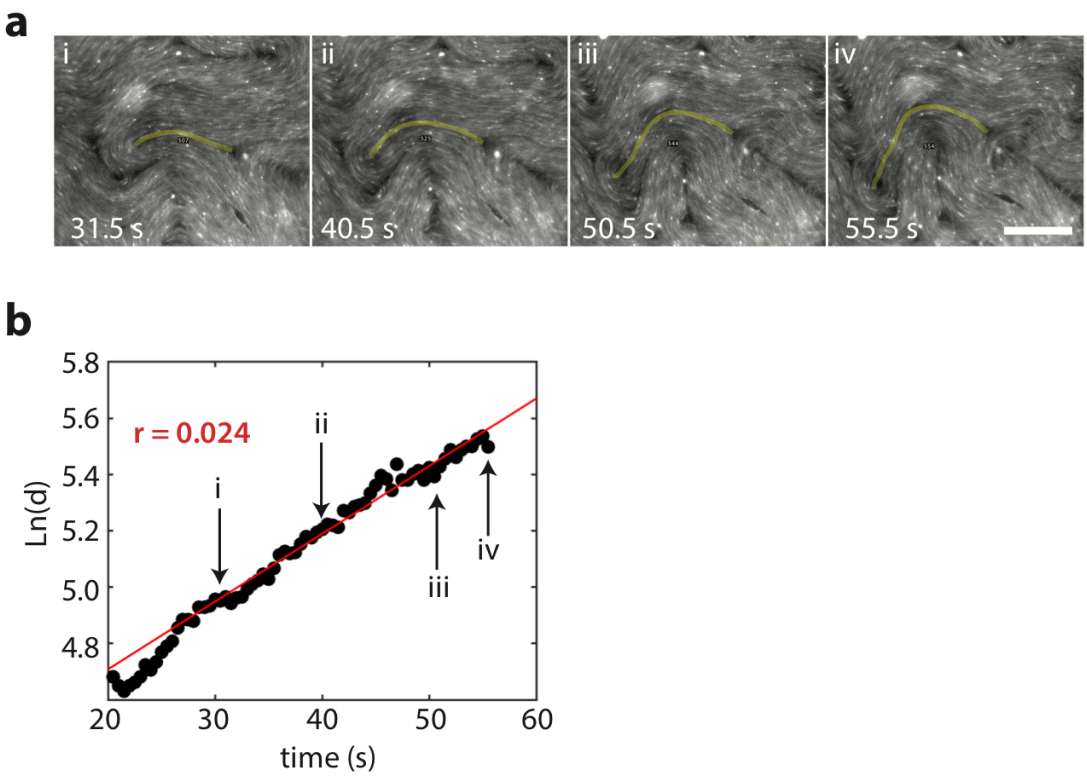

Fig. 5.9) Defect pair separation in viscous environment a) Time-lapse of defect pair separation for η=939.4(±16.4) mPa s. The yellow line indicates the growing contour length connecting the defect pair at each time point. Scale bar, 100 μm. b) Semi-log plot of contour length, d, as a function of time. b (i-iv) correspond to the time points in a (i-iv). The separation rate, r, for this example is r=0.024 s^{-1}.

Fig. 5.10 shows the defect separation rate, r, for all defect pairs in both runs for all viscosities. We report the average separation rate, <r>, as denoted by the dotted lines, and the gray shaded region represents the standard deviation. The spread of the data is largest for the lowest viscosity (η=382.2(±6.4) mPa s), and highest viscosity (1144 (±19.2) mPa s). At low viscosities, the structure of the defects is not as well-defined compared to the intermediate viscosities, and we observe more cases of defect lines in addition to ±1/2 defects.

At higher viscosities, the length-scale between defects decreases as shown in Fig. 5.8. The decrease in length-scale between defects is an indication of increased number

defect density. The increase in number of defects in the higher viscosity can lead to shorter defect lifetimes because there are more potential creation and annihilation events.

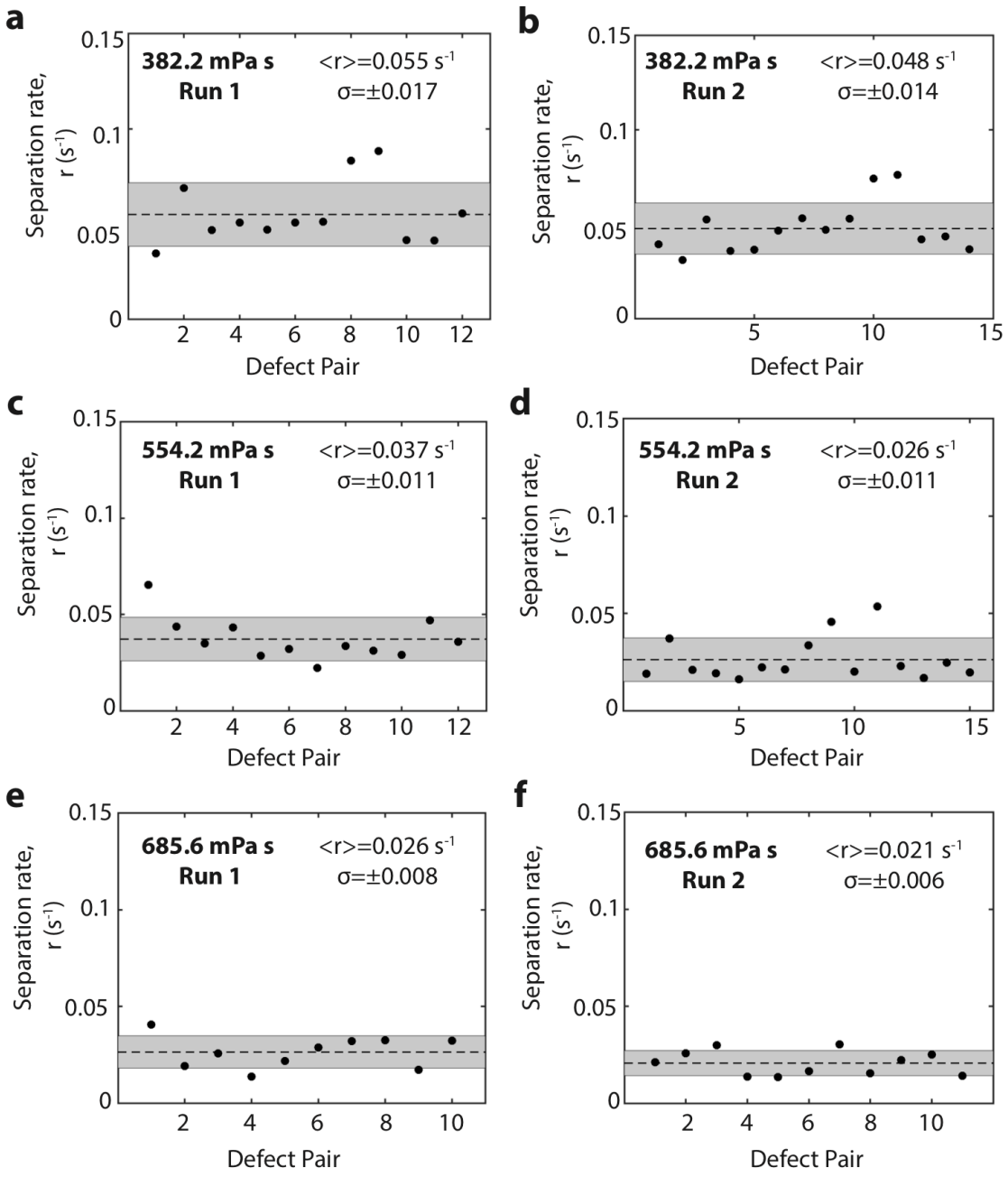

(*continued*)

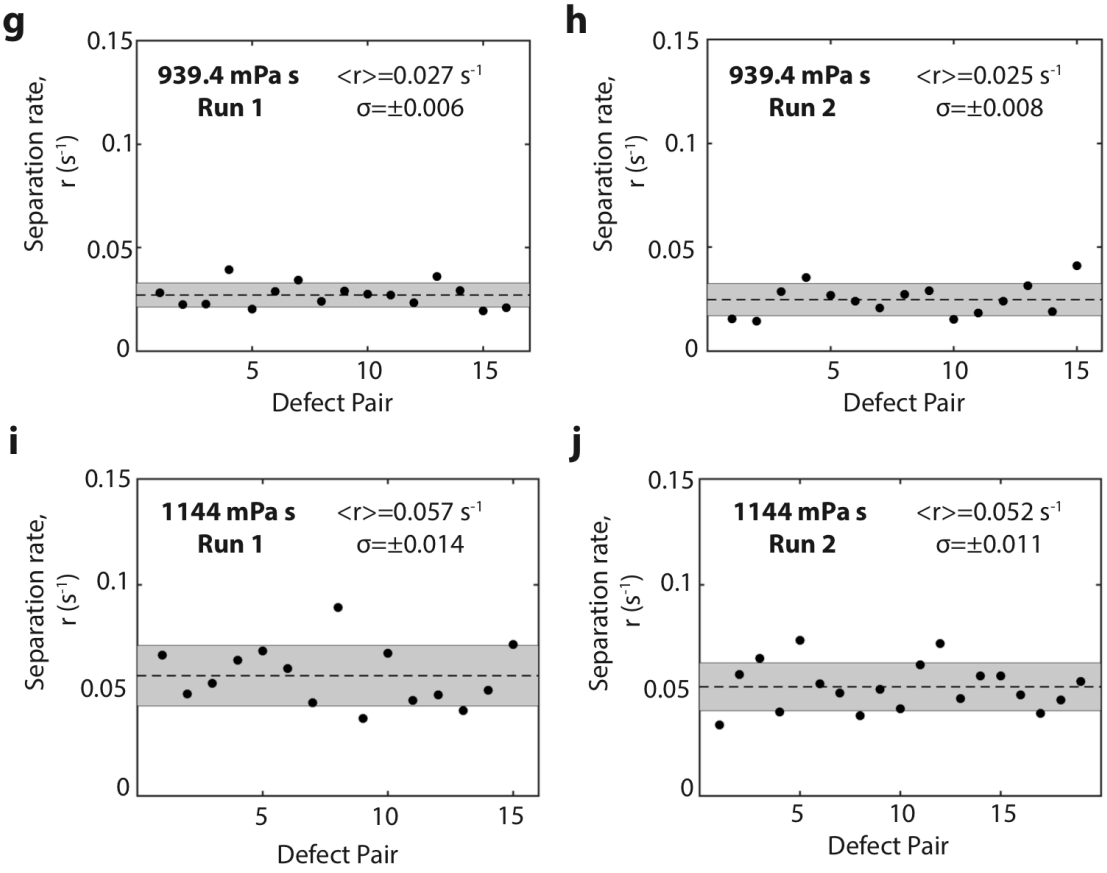

Fig. 5.10) Separation rate for defect pairs for all viscosities for run 1 and run 2. The average separation rate for a) 382.2 mPa s (run1) is 0.055 (±0.017) s^{-1} b) 382.2 mPa s (run 2) is 0.048 (±0.014) s^{-1}, c) 554.2 mPa s (run 1) is 0.037 (±0.011) s^{-1}, d) 554.2 mPa s (run 2) is 0.026 (±0.011) s^{-1} e) 685.6 mPa s (run 1) is 0.026 (±0.008) s^{-1}, f) 686.6 mPa s (run 2) is 0.021 (±0.006) s^{-1}, g) 939.4 mPa s (run 1) is 0.027 (±0.006) s^{-1}, h) 939.4 mPa s (run 2) is 0.025 (±0.008) s^{-1}, i) 1144 mPa s (run 1) is 0.057 (±0.014) s^{-1}, and 1144 mPa s (run 2) is 0.052 (±0.011) s^{-1}. The dotted line represents the mean separation rate, and the shaded grey region represents the standard deviation.

5.3.3 Topological entropy in viscous environments

To study the complexities of the active fluid in different viscous environments, we measured the topological entropy from the average of defect separation rates that are weighted by the final length where the fit ends[101]. Fig. 5.11 shows the nonmonotonic relation of topological entropy as a function of viscosity. To understand the pure geometric effects when we vary the viscosity, we nondimensionalized h to h', to remove the length-scale and velocity factors. To nondimensionalize, we multiply h, by a characteristic time, τ defined as

$$\tau = \frac{l}{V_{rms}}$$

where l is the characteristic length computed by the velocity-velocity correlation as described in section 4.2.4, and V_{rms} is the network velocity computed from PIV. The dimensionless topological entropy, h', is defined by

$$h' = h \cdot \tau$$

where h is the topological entropy and τ is the characteristic time. The nondimensionalized topological entropy, h', as a function of viscosity remains remarkably constant for both runs (run 1 in dark blue, and run 2 in teal), shown in Fig. 5.12. We find the nondimensionalized topological entropy in viscous environments is about three times the h' measured in the previous system where the active nematic was suspended at an oil/water interface where the oil was below the fluid.

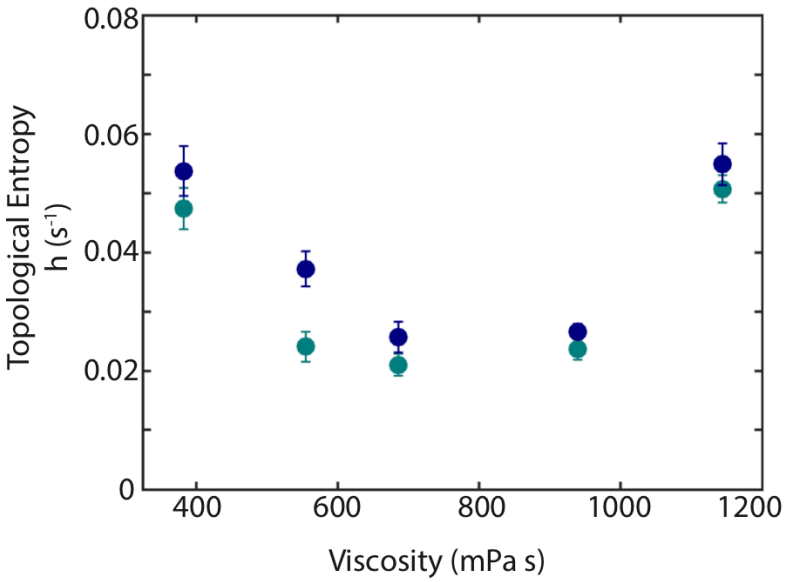

Fig. 5.11) Topological entropy as a function of viscosity. The topological entropy for run 1 (dark blue) and run 2 (teal) are calculated from the weighted average of defect separation rates. The average is weighted by the final length of where the fit ends. The error is the weighted standard error of the mean.

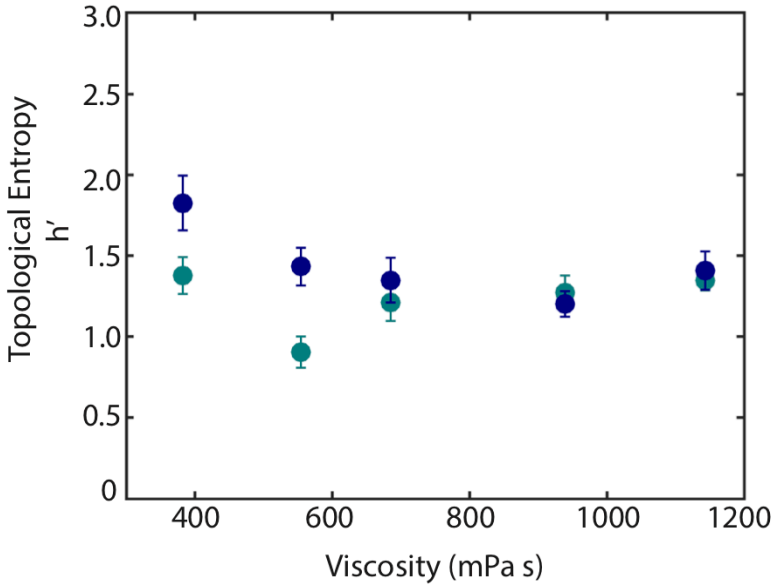

Fig. 5.12) Nondimensionalized topological entropy as a function of viscosity. The nondimensionalized topological entropy, h', for run 1 (dark blue) and run 2 (teal) are nondimensionalized by $\tau = l/V_{rms}$. The error bars are defined as $\Delta h' = h'\sqrt{\left(\left(\frac{\Delta\tau}{\tau}\right)^2 + \left(\frac{\Delta h}{h}\right)^2\right)}$.

5.3.4 Lyapunov Exponent

Another measure of chaos in the fluid is calculating the Lyapunov exponent, λ. The Lyapunov exponent describes how nearby trajectories diverge away from each other over time. The behavior of the trajectories can be described by evaluating the derivative of the flow map, which maps an initial point of the fluid to the point at a later time. We computed the same analysis as described in Tan et al.[101] and section 4.3.6, where λ is defined as

$$\lambda = \nabla v$$

where v is the velocity field generated from PIV analysis of our movies. We calculated λ, for each cropped region of the field of view used to find the V_{rms} and find the average λ for each viscosity. Fig. 5.13 shows the nonmonotonic relationship of λ as a function of viscosity. We nondimensionalized λ to compare to our topological entropy result by multiplying λ by the characteristic time, τ. Fig. 5.14 shows λ' remains relatively constant for increasing viscosity. Here, λ' is about three times smaller than *h'* measured in this system.

Surprisingly, the λ' calculated is in close agreement with the nondimensionalized topological entropy and Lyapunov exponent from Tan et al.[101] and section 4.3.6 where these quantities remained constant with increasing ATP concentration; however, there is a discrepancy between then λ' and *h*' in this experimental system.

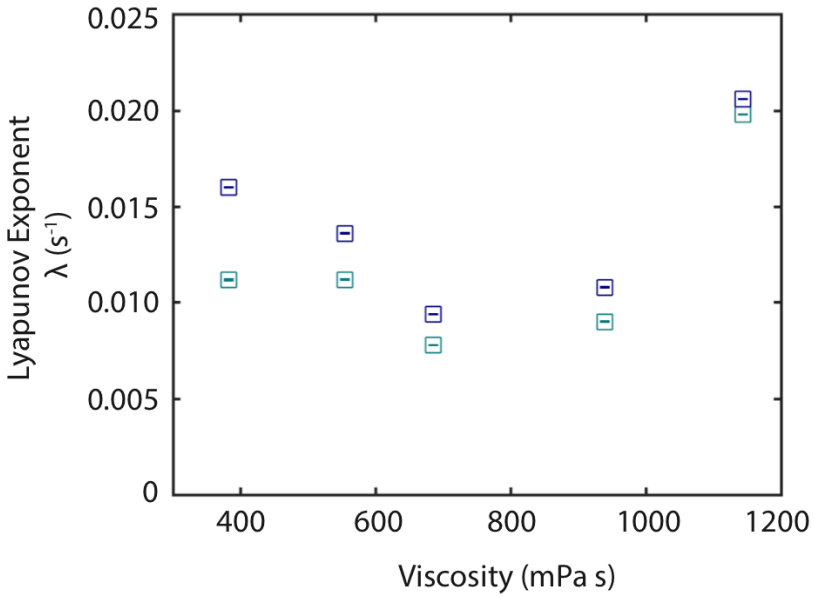

Fig. 5.13) Lyapunov exponent as a function of viscosity. The Lyapunov exponent, λ, for run 1 (dark blue) and run 2 (teal) are the average λ calculated from the gradient of the velocity field for cropped regions of the field of view. The error bars are the standard error of the mean.

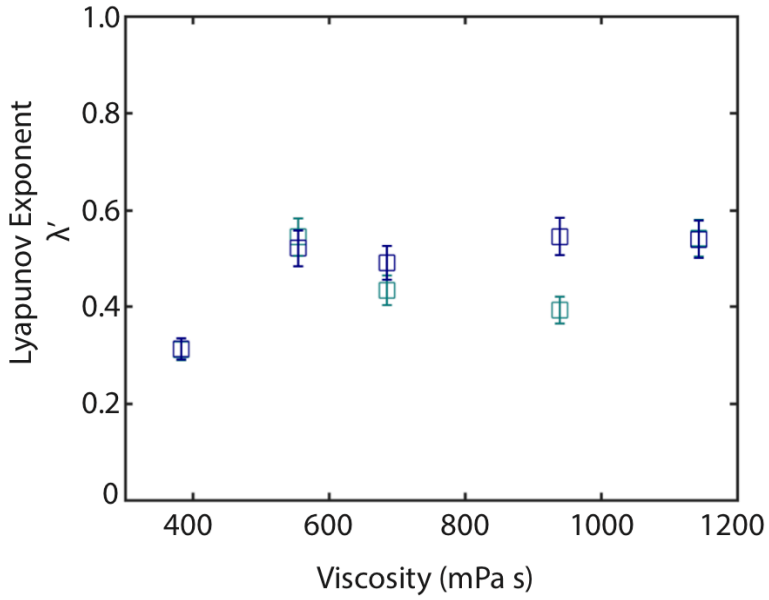

Fig. 5.14) Nondimensionalized Lyapunov exponent as a function of viscosity. The nondimensionalized Lyapunov exponent, λ', for run 1 (dark blue) and run 2 (teal) are calculated by $\lambda' = \lambda \cdot \tau$ where τ is the time-scale. The error in λ' is defined as $\Delta\lambda' = h'\sqrt{\left(\left(\frac{\Delta\tau}{\tau}\right)^2 + \left(\frac{\Delta\lambda}{\lambda}\right)^2\right)}$.

5.4 Discussion and Conclusions

The motivation of this work is to observe how the mixing behavior of the active fluid changes when in contact with viscous environments. In chapter 4, we showed the generated flows from the active nematic have characteristics of chaotic advection. We consider the active nematic to be a self-mixing active fluid. In this prior work, the nondimensionalized topological entropy was insensitive to changes in the energy injected at the local level[101]. Since the prior work focused on changing the energy injected locally, we wanted to observe how the material responds to changes in its environment.

Changing the oil viscosity that the active fluid is in contact with and keeping the ATP concentration constant is one way to probe how the structure and behavior of the active fluid adjusts to external effects. First, we created mixtures of silicon oil and determined the viscosity using rheology. The viscosity of the mixture of oils ranged from 382.2mPa s and 1144 mPa s. There are qualitative differences in the morphology of the active fluid with increased examples of defect fracturing. We observed nonmonotonic changes in the V_{rms}. The characteristic length calculated from velocity-velocity correlation remained constant for all viscosities except for a decrease at the highest viscosity. This slight decrease at 1144 mPa s is indicative of an increase in defect density, which is consistent with changes in active nematic morphology observed by Guillamat et al[100].

We compute the topological entropy by measuring defect pair separation rates in the fluid. There is a nonmonotonic relationship between topological entropy and viscosity; however, when the changes in velocity and characteristic length are removed by nondimensionalizing h to h', h' remains fairly constant for all viscosities. This indicates that the geometric complexity of the mixing remains the same despite the differences in viscosity of their environment.

As a separate independent measure of chaos in this system, we compute the Lyapunov exponent by taking the gradient of the velocity field. The Lyapunov exponent showed a similar nonmonotonic relationship with viscosity; however, the dimensionless Lyapunov exponent collapses to a constant value as a function of viscosity. Interestingly, the dimensionless Lyapunov exponent is about three times less than the dimensionless topological entropy.

The source of this discrepancy is still unknown. We hypothesize that the difference in the two quantities may be explained by the defect fracturing events. When a defect fractures, the intermediate defects annihilate each other successively. When the intermediate defects annihilate each other, the defect separation undergoes a “leap-frog”-like behavior where the defect front continues to change as defects annihilate. This may effectively increase the defect separation rate because the defect front is hopping from one intermediate defect pair to another. The increased separation rate from fracturing could be captured by defect pair separation measurements, but not necessarily in the velocity field. Therefore, the defect fracturing can contribute to higher measures of topological entropy, but not the Lyapunov exponent. Further measures comparing the velocity field at the specific locations of fracturing events and the defect velocity would provide insight to whether the defect fracturing is the cause for the discrepancy.

We conclude that complexities generated by defects in the microtubule active fluid are insensitive to changes in its external environment. Despite the addition of defect

fracturing and disclination lines in the morphology of the active fluid at different viscosities, the underlying geometric factors that contribute to the complexities of the system remain the same. This result is fascinating because changing the viscosity of the environment is a completely external way of adjusting the defect dynamics and fluid structure; however, the resulting behavior is similar to the case where the defect dynamics were changed via adjusting the energy injected locally. This consistency may indicate that the defect dynamics and fluid structure adjust accordingly in order to maintain a certain level of mixing. More work must be done to fully understand the dynamics of this self-mixing fluid.

Acknowledgements
I'd like to thank Pawan Panwar from the Martini group at UC Merced for his time and help with the viscosity measurements on the rheometer.

Chapter 6: Final remarks and future directions

Active materials are unique nonequilibrium systems that exhibit collective motion. Biological systems are a large class of active matter since biological processes constantly convert chemical energy to mechanical work. In biology, many cellular processes rely on both self-assembly and collective motion.

We explored two microtubule-kinesin based active matter systems in this dissertation. The first system is a motility assay with low density of microtubule filaments that self-assemble into a rotating spool. The second system is a microtubule/kinesin based active network that self-assembles into an extensile dynamic gel. The work done in this dissertation provides a new approach to characterizing flows in the active microtubule network and introduces the concepts from chaos theory to the field of soft matter. This new bridge connecting these fields can open up new avenues of research and methods of characterizing the unique flows in active nematics.

6.1 Transport velocity of spool formation

Microtubules driven by kinesin motors can self-assemble into rotating spools that convert chemical energy to mechanical work. These structures are an interesting bio-machine that can potentially have applications as a bio-actuator. We used kinesin propelled biotin functionalized microtubules to form rotating spools. We investigated how the transport velocity affects the timescale of which microtubules form spools to a saturating level and the spool sizes. Our results showed that the when microtubules are gliding faster the time it takes for spools to form is shortest, and this time constant increases with decreasing velocity. Interestingly, the average initial spool size is smaller for slower gliding velocities and larger for the faster gliding velocities. We speculate that the smaller circumference at slower gliding velocities arises from a confinement effect. The microtubules are slower to disperse from the initial isotropic network, so the microtubules are confined to a smaller space when the spool forms. Once the system reaches as steady state the gliding velocity has effect on the number density of spools reaches saturation and the average spool circumference. Studying the role of gliding velocity helps provide insight to mechanisms that drive self-assembly of spools. Understanding the mechanisms that drive spool formation can help understand how to control the size and behavior of the spools. Learning the key parameters that drive the spool formation is important for future studies on creating similar structures using synthetic materials.

6.2 Topological Chaos in active nematics

We studied the microtubule/kinesin active system developed by both Nédélec et al.[5] and Sanchez et al.[4]. The active network confined at a 2D oil/water interface spontaneously forms active topological defects that will have self-generated fluid flows.

We took a completely new approach and propose that the 2D active nematic behaves as an active fluid where the microtubules are the advected fluid material. As the defects move around, they act as virtual stirring rods that actively mix the microtubules. We used concepts from chaos theory, like topological entropy and Lyapunov exponent, to characterize the fluid-like behavior of the active nematic.

We used three independent measures of topological entropy and compute the Lyapunov exponent to elucidate the behavior in the active nematic dynamics. Remarkably, all measures were in agreement and indicated there is exponential stretching in the material indicating chaotic fluid-like behavior. Additionally, we found that dimensionless topological entropy and dimensionless Lyapunov exponent are all insensitive to changes in input energy (ATP concentration). This result may indicate these dimensionless quantities may describe a universal feature in these active systems.

6.3 Active fluid mixing in viscous environments

In our previous work, we investigated how changing the energy input to the active fluid affects the mixing dynamics. To further explore the potential universal features, we study how the structure and dynamics of the active fluid respond to external changes in its environment and investigate how these changes affect the mixing characteristics.

When the active fluid is in contact with oils of varying viscosity, the defect velocity and defect density change. Qualitatively, we observed an interesting difference in the defects, where there are intermediate defects that resemble fracturing as it is propelled. For our range of oil viscosities, we saw a nonmonotonic relationship between the V_{rms} of the fluid and viscosity. Also, the length-scale between defects remained constant except for the highest viscosity where there was a small decrease. The small decrease in length-scale indicates an increase in defect density.

We measured the topological entropy via defect separation and the Lyapunov exponent from the gradient of the velocity field. The dimensionless topological entropy and dimensionless Lyapunov exponent both remain constant for all viscosities; however, the dimensionless topological entropy is about three times greater than the Lyapunov exponent. The source of this discrepancy is still unclear and will need further analysis. We speculate that the discrepancy may arise from defect fracturing.

6.4 Future directions

One of the main focuses in the field of active matter is to develop theories to describe the rich nonequilibrium dynamics seen in both biological and synthetic systems. We approach the microtubule/kinesin based extensile active network from a chaos theory perspective and propose the idea of describing this reconstituted network as an active fluid itself. The work described in this dissertation provide evidence that the active network shows characteristics typically seen in in chaotic flows. This is the first-time concepts of chaos have been directly tied to active matter. Many questions remain unanswered from this perspective.

One avenue of interest is to explore more methods of quantifying chaos in this fluid. One possible method is to study a growing interface as the active network mixes. Fig. 6.1 shows an example of a potential method of studying a growing interface. Mixing two populations of microtubules in the active network and observing the evolution of the interface as the two populations mix can be another method of quantifying the complexity of the mixing behavior. Fig. 6.1 is an example of a 3D microtubule network where half the population is fluorescent, and the other half is not fluorescent. When the populations mix, it is evident that the interface becomes more complex.

A proposed experiment to study the growing interface in 2D is to use Fluorescence Recovery After Photobleaching (FRAP). In a FRAP experiment, a localized area in the sample is photobleached, then the fluorescence recovers as the fluorescent material diffuses into the photobleached area. FRAP is a common technique used to measure diffusion constants lipid membranes. With FRAP, a spot-size in the active material can be photobleached to create a sharp interface, and the evolution of the interface can be recorded as the active fluid mixes. Additionally, the recovery time of the fluorescence may provide information about the timescale at which the material mixes.

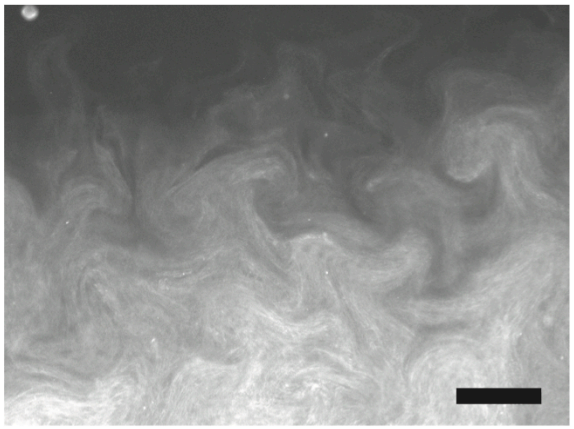

Fig. 6.1) Fluorescence image of 3D active microtubule network mixing at an interface. The bottom half of the image represents fluorescent microtubules in the flow cell. The top half of the image contains unlabeled microtubules. As the fluorescent microtubules mix, the interface becomes convoluted. Scale bar, 200 μm.

Moreover, an interesting complement to classic mixing experiments would be introducing a colored dye into the active fluid and studying the growth of the dye material as the defects process and braid around each other. A similar experiment can be done by using two fluorescent labels for the microtubules. One label can be used to image the whole active nematic, whereas microtubules with the second label can be used as tracer filaments to see how the filaments are advected throughout the fluid.

Another characteristic of chaotic flows is that tracers in the flow develop complex fractals. A fractal describes geometric structures that appear the same at different length-scales. An example of a fractal pattern seen in nature is lightning. The different paths that lightning takes to strike the ground exhibit the same pattern, at different length-scales.

Fractal analysis has been used to study self-similarity of structures in flows with chaotic advection, such as mixing magma[103]. The fractal dimension can describe the degree of dispersion of one fluid mixed in another. Fractal analysis on the microtubule active fluid can provide information about the self-similar structures present as the fluid mixes. This can also be used as a tool to compare the microtubule active fluid to other fluids found in nature.

A quantity used to classify nonequilibrium dynamics is number density fluctuations. A characteristic of equilibrium systems of size N and volume V is that fluctuations in the standard deviation of N particles, ΔN, is proportional to $\sqrt{N}$, so that fluctuations in the number density decrease as $1/\sqrt{V}$. For active systems, ΔN grows faster than $\sqrt{N}$. These large number fluctuations arise from a coupling between the order and density fields in active systems[104]. Large number fluctuations have been observed in active systems such as agitated granular rods[10], propelled filament proteins[105], and swimming filamentous bacteria[104]. These large number fluctuations seem to be a common characteristic in active matter that describes how the systems become ordered when they collectively move. Since this quantity has been observed in a wide range of systems, it could potentially be a universal feature of active matter. Exploring this analysis on the active microtubule network would be an interesting direction to understand the fundamental features that connect active systems together.

Furthermore, an interest of study is to find methods of controlling the defect dynamics. Groups have started exploring how defects act when confined in various geometries[64,65,68]. In these confined geometries, groups have observed defects moving in a quasi-periodic motion. Designing geometries that can better control and stabilize defect dynamics can lead to optimizing mixing dynamics in this active fluid. Optimizing mixing dynamics can help develop applications such as a self-mixing solvent.

The studies presented here in this dissertation have focused on self-assemblies and collective motion using microtubules and kinesin motors. We have introduced a new perspective on active nematics by using chaos to describe the active dynamics; however, there are still many remaining questions to be answered. The potential experiments outlined here could shed more light on developing theories to explain the system.

Appendix

A.1 Kinesin Prep (Hirst Lab)

Day One

1. Make 400mL TPM media in 1L flask:

LB Broth	**TPM Media (400ml)**
10g/L Tryptone	8g Tryptone
5g/L	6g Yeast Extract
10g/L	1.6g NaCl
	0.8g Na2HPO4
	0.4g KH2PO4
	Add ddH2O to bring final volume to 395.6mL and autoclave

2. **Make Agar plates (if needed)**

   LB Agar Powder: Dissolve 32 g/100ml

   Making ~10 plates
   1. Add 3.2 g LB Agar Powder to 100 ml ddH20
   2. Autoclave for 30 min on liquid setting
   3. Allow LB agar to cool to Room temperature but not too long or it will solidify. If it forms a solid, you can microwave it to get it back to liquid.
   4. Add 100ul 100mg/ml Ampicillin to the 100ml LB Agar.
   5. Pour LB Agar into petri dishes and let sit. (only need to fill to the bottom line ~10ml per plate.
   6. Parafilm the sides and store upside down in fridge

3. **If starting from plasmid from Addgene or plasmid in DH5α-cells (storage):**

   The plasmids from Addgene come in a bacterial slab. The cells from the bacterial slab need to be plated, grown, and transformed into BL21 cells.

   1. Make a sterile environment (near a flame or Bunsen burner)
   2. Take agar plates with anti-biotic resistance (Ampicillin) and label the bottom with plasmid type, date, and name. Keep agar plates flipped upside down
   3. Working near the flame, open the agar plate by lifting the bottom part over. (Open upside down keeping the lid facing up)

4. Take the bacterial slab, and use a sterilized loop, toothpick or pipette tip to touch the punctured area in the bacterial slab and make a streak (#1) on the plate like in the diagram:

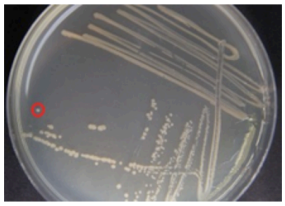

5. Take a fresh sterile loop, toothpick, or pipette tip, and run it through streak (#1)
And make a second streak (#2). Repeat for streak number 3.
6. Close the agar plate keeping it upside down, and place in 37C for 12-18 hours (overnight).

https://www.addgene.org/protocols/streak-plate/

Growing up cells for DNA miniprep

In the morning, if there are enough single-colonies, you can save the plate by parafilming the edge and keeping it in 4C.

1. In a sterile environment (near flame), take agar plate with bacterial growth and locate single colonies.
2. In a sterile falcon tube (50ml), add:

5ml LB Broth
5ul 100mg/ml Ampicillin
50ul 20% glucose

3. Pick a colony with a sterile pipette tip and add 1 colony (with the pipette tip) into the starter culture and grow in shaker shaking a 225rpm at 37C (4-8hrs). When capping the falcon tube, make sure the cap is not screwed on completely to allow air flow. The starter culture should be cloudy when ready OD_{600}=1
4. Once the starter culture is ready, can cap and store in 4C overnight before spinning the cells down, or continue with the next steps.

*Can make a glycerol stock by spinning down starter culture at 4500 rpm for 30 min at 4C. Dump out the supernatant and resuspend the cells in fresh 1ml fresh LB broth. Take 500ul of 50% glycerol (autoclaved) and 500ul of resuspended cells and mix in a screw-cap tube. Vortex and drop freeze. Store in -80.

DNA Miniprep

Once the starter culture is ready:

1. Cool down the centrifuge to 4C

2. In a sterile environment, carefully remove the pipette tip from the starter culture and close the cap tightly. Make a balance with equal weight.
3. Spin down the cells at 4500 rpm for 30 min
4. Dump out the supernatant and follow the instructions for QIAprep Spin Miniprep kit
(From the Miniprep kit instructions):
5. Resuspend pelleted bacterial cells in 250ul Buffer P1 and transfer to microcentrifuge tube.
6. Add 250 ul Buffer P2 and mix thoroughly by inverting the tube 4-6 times until the solution becomes clear. Do not allow the lysis reaction to proceed for more than 5 min.
7. Add 350 ul Buffer N3 and mix immediately and thoroughly by inverting the tube 4-6 times.
8. Centrifuge for 10 min at 13,000 rpm in a table-top centrifuge
9. Apply 800 ul supernatant from step 8 to the QIAprep 2.0 spin column by pipetting.
10. Centrifuge for 30-60 s and discard the flow through.
11. Wash the QIAprep 2.0 spin column by adding 0.5 ml Buffer PB and centrifuge for 30-60 s and discard the flow-through
12. Wash the QIAprep 2.0 spin column by adding 750 ul Buffer PE. Centrifuge for 30-60 s and discard the flow through.
13. Centrifuge for 1 min to remove residual wash buffer
14. Place the QIAprep 2.0 column in a clean 1.5 ml Eppendorf tube. To elute the DNA, add 50ul Buffer EB (10mM TrisCl, pH 8.5) or water to the center of the column and let stand for 1 min.
15. Centrifuge for 1 min.
16. Check the purity/concentration of plasmid using nanodrop.
17. Drop freeze DNA plasmid and store in -80. (label and date) Use this DNA to transform into BL21 cells.

4. **Make buffers if needed (use sterile filters and store in 4 degree C)**

Lysis Buffer:	**Wash Buffer:**	**Elution Buffer:**
50mM NaPO4 pH. 8.0 250mM NaCl	50mM NaPO4, pH 6.0 250mM NaCl 1mM MgCl2	50mM NaPO4, pH 7.2 500mM Imidazole 250mM NaCl 1mM MgCl2

5. **Transform kinesin DNA into Rosetta competent cells (BL21 cells)**

➔ If starting from glycerol stock, can skip the transformation, and directly plate glycerol stock and grow on a plate, or scrape some from glycerol stock and put into starter culture

Transformation Protocol (BL21 Invitrogen)

1. Thaw 1 vial of one shot BL21 cells on ice (50ul)

2. Add 5-10 ng of DNA (in volumes of 1-5 ul) to cells and mix by tapping gently (DO NOT PIPETTE)

3. Incubate vial on ice for 30 min

4. Heat shock cells by incubating vial in 42C water bath for EXACTLY 30 sec. Do not mix or shake

5. Remove vial from 42C bath and quickly place on ice

6. Add 250 ul of pre-warmed SOC medium to the vials. (SOC is a rich medium; use proper sterile technique to avoid contamination). Make sure everything is sterile when adding SOC to the vials. Add the SOC medium in fume hood.

7. Secure vial(s) in a microcentrifuge rack with tape. Place the rack in a shaking incubator and shake the vials at 37C for 1 hour at 225 rpm.

8. Set up a flame, and do not turn on air in the hood. Do everything near the flame to keep sterile. When plating, use the glass spreaders. Dip the glass spreader in alcohol, let dry a bit and wave over the flame, then you can use it to spread the cells on the plate. Add the amount of cells on the plate, and use the sterile glass spreader to spread cells on plate.
Plate two different volumes (ranging from 20-200ul) of the transformation reaction onto LB plates containing the appropriate antibiotic for plasmid selection. Plate 2 plates. For single colonies take 10ul of the cells +90ul of LB broth. And plate the 100ul on LB agar plate.
Remaining cells can be stored in 4C. If the cells don’t grow, can replate using the same transformed cells.

9. Invert plates and grow over night at 37C

Day 2
Take plates out of the 37C in the morning. Make sure there are enough single colonies. Parafilm and keep at 4C until starting the starter culture.

Starter Culture (from bacteria plate)
Put 15 ml of LB broth into 50ml falcon tube.
Add 15ul 100mg/ml Amp and 150 ul 20% glucose
Pick a colony with a sterile pipette tip
Add 1 colony (with the pipette tip) into the starter culture and grow overnight in shaker shaking a 225rpm at 37C (12-18 hours)

Starter Culture (from glycerol stock)
Put 15ml of LB broth into 50ml falcon tube
Add 15ul 100mg/ml Amp and 150ul 20% glucose
Take glycerol stock from -80 (DO NOT THAW) and scrape a bit from the top with a pipette tip
Add the tip to the falcon tube and grow overnight in shaker shaking at 225rpm at 37C (12-18 hours)

Day 3

1. Cool centrifuge to 4C.
3. Centrifuge cells at 4500 rpm at 4C for 30 min. Dump out supernatant and resuspend in 1ml LB for glycerol stock and TPM media for culture
2. **To make glycerol Stock:** Take 500ul of cell and 500ul of 50% glycerol. Vortex. Drop freeze and store in -80. (Can store in fridge until you can drop freeze)
4. Add to TPM media 4ml 20% glucose
400ul 100mg/ml Ampicillin
6. Take 1ml TPM media out to set Ref
7. Add starter culture to the 400ml culture
8. Shake at 37C until OD_{600} reaches 0.6-1

Time start: _____ Time end: _____ Final OD:_____

9. Take 400 ul gel sample, spin down at 14xg rpm for 10 min and resuspend in 50ul 1xDB
10. Let culture come to room temperature
11. Add 0.2 mM final concentration IPTG
12. Shake overnight at 225rpm at 22C

Day 4
1. Take a 400ul sample of the cells after overnight growth. Spin down. Keep 50ul of the sup and resuspend in 2XDB. Resuspend the pellet in 1XDB
2. Pour the cells into centrifuge tubes and spin down cells for 10 min at 4oC, at 5000 rpm (RC6Plus)

4. Pour off supernatant, freeze pellet in -80 for 1 hour (Can stop here and save pellet up to a week for purification later)
5. Put pellet on ice and resuspend in 30mL cold lysis buffer after *(keep on ice during resuspension)

*To 30ml Lysis buffer add: 30ul 2mg/ml Aprotonin
30ul 2mg/ml Leupeptin
30ul 2mg/ml Pepstatin
30ul Tween-20
150 ul 100mM ATP

6. Add 62 mg Lysozyme
7. Rock at 4oC for 20 min
8. Add 15ul DNase-1 (Sigma)
9. Sonicate 1 minute on ice (Setting 3)
10. Centrifuge 30 min 4oC, 40,000xg (24,000 rpm in Munoz lab) (T865 rotor)

Bead Equilibration
Do not put beads on ice
**put beads on rocker to ~30 minutes at 4oC to get beads fully into solution before using*

1. Add 500ul Ni-Agarose beads to 2mL tube. Add 1.5 mL Lysis buffer. Invert tube 10 times, spin 2 minutes at 500xg, remove supe without disturbing bead bed.
2. Repeat for a total of 4 times

11. Pour supernatant (from step 10) into 50ml conical tube
12. Take 50 ul gel sample
13. Add 620 ul 1M Imidazole to supernatant
14. Add some supernatant to beads and bring back and forth to get beads into supernatant conical
15. Incubate at 4oC on rocker for 1.5 hours

Wash and Elution Buffers: *Add ATP right before use*

Wash Buffer	**Elution Buffer**	**PEM-100:**
25mL Wash Buffer	2.5mL Elution Buffer	12mL PEM-100
25 ul 100mM ATP	2.5 uL 100mM ATP	12 ul 100mM ATP

17. Flow Lysate supe + beads through column (*take 50ul of gel sample of flow-through) *Lysate FT may be put in -80 freezer and use for another purification
18. Flow 25 ml Wash buffer (w/ ATP) over column (*take 50 ul gel sample)
19. Flow 150ul Elution buffer (w/ATP) over column and collect first fraction (*take 50 ul gel sample)
20. Flow 500ul Elution Buffer (w/ ATP) over column for fractions 2-5 (*take 50ul gel sample)

(collect all 500ul (fraction 2) then flow another 500ul through the column and repeat for all 5 fractions

Gel Samples
___2 ____3 ___4___5

*Keep fractions from step 19 and 20 (should have 5 fractions total)
21. dot blot to verify fraction containing kinesin:
-with pencil, draw 5 circles on a piece of filter paper, label circles
-add 1ul of each fraction to respective circles
-stain with coomassie for 30 seconds
-destain

Buffer Exchange
1. Remove top and bottom cap of NAP-5 column
2. Allow buffer to completely drain by gravity flow
3. Add 10mL PEM-100(w/ATP) and allow to completely enter gel bed
4. Add 500ul of elution with protein (determined by dot blot) (**wait until all sample is entirely in the gel bed before collecting)**
5. Put new 1.5 mL tube under column when all of the sample is in the gel bed
6. Add 1mL PEM-100 (w/ ATP) and collect elution (20uL gel sample)

Add 200uL 60% sucrose (10% final concentration) to buffer exchanged kinesin
Aliquot
Drop freezing in liquid nitrogen and store in -80oC

*If you take 20ul out of an elution for gel, add 20ul of the next elution into the first elution to bring it back up to 500ul.

A.2 Tubulin Purification from Pig Brains

Hirst Lab Protocol (adapted from Ross Lab)

Reference: Shelanski, M.L, F. Gaskin, and CR Cantor (1973). PNAS 70:765-768

Stock Solutions: Buffer (200mL)		PM Buffer (200mL) pH6.9	PMG
500mM PIPES		40mL	30.4 mL
200mM EGTA		2mL	2mL
100mM $MgCl_2$		2mL	2mL
13.7M Glycerol	(stock)	-------	
s116mL			

	Super PMG (200mL)
1M PIPES (500mM)	16mL 32mL
1M $MgCl_2$	2mL
200mM EGTA	2mL
13.7M Glycerol (stock)	175.2mL 164mL

1mL GTP (Sigma-Aldrich G8877) 5mL of 100mM GTP

1. Clean brains (3) and put in pre-tared 1L beaker: weight of beaker:_____
2. Weigh cleaned brains: _____g
3. Put brains in blender
   Add 0.5mL PM buffer per 1g of brain. Volume of PM: _____mL
4. Pulse blender to homogenize brains
5. Pour blended brains into ultracentrifuge tubes (Victor's rotor)
6. Balance tubes with the caps
7. Centrifuge at 100,000 xg (37,000rpm) for 45 minutes at 2°C
8. Pour supernatant into 500mL graduated cylinder (use pasteur pipettes to get all sup)
   Volume of sup: _____mL
9. Add same volume of PMG to the sup (1:1 PMG:sup ratio) Total volume: _____
   *Alternative: If sup volume is greater than 100mL, add ½ sup volume as super PMG ie: sup=110mls, add 55mls SUPER PMG)
10. Add GTP to final concentration of 1mM
    _____mL of 100mM GTP stock
11. Mix by inverting cylinder (cover with parafilm)
12. Put sup into 50ml Falcon tube, polymerize MTs for 45 min at 37C water bath
13. Set ultracentrifuge to 37°C, place MLA-55 rotor in 37°C incubator to warm up
14. Pour the sup from the falcon tube to centrifuge tubes, balance (with caps)

15. Centrifuge at 100,000xg in MLA-55 rotor for 45 minutes at 37°C (37000rpm in victors centrifuge)
(IF STOPPING) Pour most of the supernatant except for a small amount to cover the pellets. Scrape pellet out and put in falcon tube to drop freeze in LN2 and store in -80.
(STOPPING POINT)
These are the 1X Pellets (can drop freeze and store at -80°C or continue)

2X Pellets:
Cool MLA-55 rotor to 4°C and cool the centrifuge to 4°C.
*If continuing the same day, remove all the supernatant by dumping into waste and pipetting off the last bit.
*If continuing from frozen pellets, quickly thaw pellets at 37°C. Dump excess sup that froze with pellets, and pipette the excess.

1. Add PM to pellets using 1/5 volume of original homogenate (step 3 above). Put a bit on top of each pellet.
    Volume of PM Buffer added: _____mL
2. Using a thin, pointed spatula, scrape pellet off side of centrifuge tube and into PM buffer
    Lightly shake tube to make sure pellet is loose
    Quickly dump PM buffer + pellet into 15mL dounce in ice slurry
    Repeat for each pellet
3. Homogenize pellets in cold dounce until no large chunks seen (will be cloudy)
    Incubate on ice 30 minutes and homogenize every 2-3 minutes (avoid excessive bubbling)
4. Put homogenized tubulin into ultra-centrifuge tubes (MLA-55 optiseal tubes). Balance two tubes at a time and don't forget to balance with caps.
5. Centrifuge 100,000xg for 30 minutes at 2°C
6. Pour sup into graduated cylinder and approximate volume
    Volume of supernatant: _____mL
7. Add PMG buffer 1:1 with supernatant (same as step 9)
    Add _____mL PMG
8. Add GTP to final concentration of 1mM
    Add _____µL 100mM GTP stock
9. Mix PMG and sup by inverting cylinder with parafilm over top. Be careful not to lose any!
10. Put supernatant into new ultracentrifuge tubes (optiseal tubes), close caps, and incubate 45 minutes at 37°C in water bath to polymerize. Place MLA-55 rotor into the 37C incubator to warm up. Set ultracentrifuge to 37C and turn on vacuum to allow to warm up.
11. Centrifuge at 37°C for 45 minutes at 100,000xg (2X pellets)
12. Save 2X pellets by removing most of the sup, leaving a small amount to cover the pellets. Pellets can be further purified with high salt.
13. Drop freeze pellets in liquid nitrogen and store at -80°C

High Salt

1. Quickly thaw pellets at 37ºC (in water bath), dump excess supernatant that froze with pellet
2. Take 2 2X pellets and homogenize in 5mL PM buffer for 30 minutes on ice (as in step 3 above) (in dounce).
3. Using T865 rotor, Spin at 100,000xg at 4ºC (MLA-55 rotor) for 30 minutes
4. Save sup and add equal amounts of the high salt buffer to the supe:

<u>High Salt Buffer</u>
0.5M PIPES
10% DMSO
1mM GTP
2mM EGTA
1mM $MgCl_2$

5. Incubate at 37ºC for 10 minutes
6. Spin 20 minutes at 20,000xg at 37ºC (MLA-55 rotor)
7. Homogenize pellet in 4mL PEM-100 on ice for 30 minutes
8. Spin 30 minutes at 100,000xg at 4ºC (MLA-55 rotor)
Take a same to run a gel (1x high salt)
<u>2x Wash</u>
9. Add equal amounts of high salt buffer to sup
10. Incubate at 37°C for 10 minutes
11. Spin 20 min at 20,000xg at 37°C (MLA-55)
12. Homogenize pellet in 5mL PEM-100 on ice for 30 minutes
13. Spin 30 min at 100,000xg at 4°C (MLA-55 rotor)
14. Take a sample and run a gel to see check purity (2x high salt)
15. Bradford of tubulin
    Dilute to 5 mg/mL using PEM-100
    Aliquot
    Drop freeze in liquid nitrogen and store in -80ºC

A.3 GTP Microtubule Polymerization

Protocol **Record lot:**_____

1. Start centrifuge
2. Gel aliquot of unlabeled tubulin from -80°C freezer-Thaw in hand
    a. Resuspend Rhodamine Tubulin in PEM 100 – (20mg rhodamine tubulin)

3. Incubate tubulin (rhodamine and unlabeled) on ice for 10 min

4. Add unlabeled tubulin and labeled tubulin together

    For _____% labeled: _____ul tagged + _____ul unlabeled = _____ul total

5. Centrifuge in MICRO ULTRA for 10 min at 90,000 rpm to remove dead tubulin
    a. Use small rotor that's cooled to 4°C
    b. Centrifuge with label out to help locate pellet
    c. Get 100mM GTP from -20°C Freezer

6. Remove supernatant and put 1.5 ml Eppendorf tube (save sup) Add _____ul _____mM GTP to make 1mM (final) GTP

7. Put Eppendorf tube in incubator for 20 min at 37°C.

8. Add _____ul 2mM Taxol (final concentration should be 50uM)

9. Incubate for 20 min at 37°C

10. Centrifuge Eppendorf tube for 10 min at 25C -14,000xg

11. Pippette supernatant out and discard. Resuspend pellet in final concentration - 50uM taxol and original volum x ul of PEM100.

12. Incubate MTs for 1 day to yield best result

A.4 Microtubule spooling assay

Kinesin solution
100nM kinesin
20mM DTT
in PEM80

Chamber Wash (Surface blocking solution)
5 mg ml^{-1} Bovine Serum Albumin (BSA)
50μM Taxol
20 mM DTT
in PEM80

Diluted Microtubules
0.047 mg ml^{-1} tubulin
20 μM Taxol
in PEM80

Anti-fade Solution
10μM ATP
20 mM DTT
8.5 mg ml^{-1} glucose
0.28 mg ml^{-1} glucose oxidase*
210 mM catalase*
in PEM80

Streptavidin Solution
0.01 mg ml^{-1} FITC streptavidin
10μM ATP
20μM Taxol
0.2 mg ml^{-1} BSA
in PEM80

ATP (With Regenerating system) (1mMATP)
1mM ATP
50μM Taxol
20mM DTT
2mM Phosphocreatine*
70μg ml^{-1} creatine phosphokinase*
0.28 mg ml^{-1} glucose oxidase*
210 mM catalase *
in PEM80

*add right before use

1. Clean cover glass and cover slip with ethanol.
2. Make a flow cell by sticking two pieces of double-stick tape ~5mm apart on the cover glass and sticking the cover slip on top.
3. Flow in 10μl of kinesin solution (100nM kinesin and 20 mM DTT in PEM80) and incubate for 5 minutes to allow motors to absorb to the glass.
4. Exchange fluid in flow cell with 10μl of surface blocking solution (5 mg ml^{-1} bovine serum albumin (BSA), 50 μM Taxol, 20mM DTT in PEM-80) by flowing in new solution on one end of the flow cell, and wicking out the other end with a piece of filter paper.
5. Flow in 10μl of fluorescent biotinylated microtubules (0.047 mg ml^{-1} tubulin and 20 μM Taxol in PEM-80) and incubate for 3 minutes to allow microtubules to bind to kinesin motors.
6. Excess microtubules not bound to kinesin are washed out using 10μl of anti-fade solution (10μM ATP, 20 mM DTT, 8.5 mg ml^{-1} glucose, 0.28 mg ml^{-1} glucose oxidase, 210 mM catalase in PEM-80)
7. Flow in 10μl of streptavidin solution (0.01 mg ml^{-1} FITC streptavidin, 10μM ATP, 20 μM Taxol, 0.2 mg ml^{-1} BSA in PEM-80) and incubate for 3 minutes.
8. Excess streptavidin is washed out using 10 μl of the anti-fade solution from step 6.

9. Flow in 10 µl of motility mix with ATP regenerating system (1mM ATP, 50µM Taxol, 20mM DTT, 2 mM phosphocreatine, 70 µg ml^{-1} creatine phosphokinase, 0.28 mg ml^{-1} glucose oxidase, 210 mM catalase in PEM-80) to activate kinesin motion.
10. Seal off flow cell with vacuum grease and image.

A.5 Acrylamide polymer brush glass slide treatment

1. Warm ddH_2O with ~100µl of soap in a 100ml beaker on a hot plate
2. Add glass coverslips into the soapy water
3. Rinse each coverslip in the soapy water and rinse 3-4 times with fresh ddH_2O to wash the soap off. Can be store in ddH_2O until further cleaning and treatment
4. Fill a 100ml beaker with Ethanol. Rinse coverslips in ethanol and 3 times with ddH_2O.
5. Fill a 100ml beaker with 0.1M NaOH. Rinse coverslips in 0.1M NaOH and 3 times with ddH_2O.

6. Lay coverslips on a glass dish and pour silane solution over the coverslips and let sit for 10-15 min.

Silane solution:
100ml ethanol
1ml acetic acid
500µl Trimethyl…

7. Rinse coverslips 3 times with ddH_2O.

8. Lay the coverslips on a glass petri dish and pour acrylamide solution over coverslips.

Acrylamide solution:
95 ml ddH_2O
5 ml 40% acrylamide solution (degas for 30 min)
Add:
35µl TEMED
0.07g Ammonium persulfate

9. Store coverslips in the acrylamide gel until ready for use. Rinse coverslips with ddH_2O prior to use.

A.6 Aquapel treatment for glass slides

1. Clean glass slide with acetone, methanol and ethanol.
2. Drop-cast 100µl of Aquapel onto a glass slide.
3. Place a second glass slide face-down, perpendicular to the first slide to spread the aquapel evenly on both surfaces. Let sit for 1min.
4. Dry with compressed air and sonicate slides in ddH_2O for 2 min.
5. Rinse slides in ddH_2O and let air dry prior to use.

A.8 GMPCPP microtubule polymerization

1. Mix _____µl of _____mg/ml unlabeled tubulin with _____µl of _____mg/ml labeled tubulin in a 500µl ultracentrifuge tube. Incubate on ice for 10 min. (Final concentration desired: (6.8mg/ml and ~4% labeling)

Total volume_____ and %labeled_____

2. Spin down tubulin mixture for 10 min at 90,000 rpm at 4°C.

3. Remove the supernatant and put into a new Eppendorf tube.

4. Add _____µl of 10 mM GMPCPP (final concentration 0.6mM)

_____µl of 100mM DTT (final concentration 1mM)

5. Incubate at 37C water bath for 30 min

6. Remove from water bath and spin down in table-top centrifuge at 14,000 rpm for 10 min.

7. Remove the supernatant and resuspend the pellet in _____µl of M2B buffer for final concentration of 6mg/ml. Store at room temperature for 2 days before use.

A.8 Active Premix (for active nematic experiments)

From Dogic Lab

M2B Buffer
80mM PIPES pH 6.8
2mM $MgCl_2$
1mM EGTA

Solutions in M2B buffer:
PEP (Monopotassium Salt) 200mM pH to 6.9 with NaOH
0.5M DTT
0.352 mg/ml Streptavidin

Solutions in 20mM K_2HPO_4 (Dibasic Potassium phosphate)
20mM Trolox (pH 7.48)
Glucose (300mg/ml) + 70mM KCl (pH 7.2)
20mg/ml Glucose Oxidase (pH 7.5)
3.5 mg/ml Catalase+100mM KCl (pH 7.4)

KSA
5µl K401 (0.7mg/ml)
5.7 µl 0.325mg/ml Streptavidin
0.5µl 1:100 DTT (diluted from 0.5M DTT)
Incubate for 40 min
Add 9.7µl M2B

MIX
933µl M2B
67 µl 1M $MgCl_2$

AO1
16µl 0.5M DTT
4µl M2B
20 µl 300 mg/ml Catalase

AO2
20 µl 3.5 mg/ml Catalase
20 µl Glucose Oxidase

Premix (w/o ATP and buffer)
12 µl 6% (wt%) 20kD PEG
8 µl PEP
6 µl Trolox
4 µl KSA
2.9 µl MIX
1.7 µl PKLDH
1.33 µl AO1
1.33 µl AO2

(Recipe leaves out ATP and M2B/Pluronic F127 Buffer)
Take 3.73 µl of the premix and add 1.27 µl of ATP/M2B/12%Pluronic to bring up to volume (5µl). Add 1 µl GMPCPP microtubules.

A.9 Active Nematic Velocity Experiments

1. Rinse a polyacrylamide coated coverslip with ddH_2O and let dry. Prepare an aquapel coated glass slide.

2. Construct a flow cell with a ~6µl volume channel by placing two pieces of double-sided tape ~3mm apart onto the hydrophobic surface on the glass slide. Place the hydrophilic coverslip on top and press down on the edges to ensure a tight seal.

3. Prepare the active network by combining 3.33µl of premix, x µl of ATP (final concentration 0.05-1mM), 0.25µl of silica beads, 1µl of GMPCPP microtubules, and x µl of M2B (final total volume 6µl).

4. Flow in 6µl of HFE7500 oil with 1.8% RAN surfactant into the flow cell.

5. Exchange the oil in the flow cell with 6µl of active network mixture.

6. Seal the edges of the flow cell with UV-curing glue (RapidFix).

7. Spin down the sample in a swinging bucket rotor at 300 rpm for 42-45 min.

8. Image the sample in bright-field to view the beads, and fluorescence to view the active nematic.

A.10 Active Nematic Viscosity Experiments

PDMS well construction

1. Tare weigh boat
2. Mix together 0.1g Sylgard 184 Elastomer curing agent/1g Sylgard 184 Elastomer base using a metal spatula until many tiny bubbles form.
3. Degas the mixture in desiccator until all bubbles have disappeared (~30min to 1 hour)
4. Clean a glass slide with acetone, methanol and ethanol.
5. Take a piece of tape that is wider and longer than the glass slide. Place the glass slide in the center of the tape. Fold up the long edges of the tape around the glass slide, then fold up the short edges of the tape around the glass. This will form walls around the glass slide.
6. Pour the degassed PDMS mixture into the well so that the PDMS is about 1-2mm thick and heat at 65C on a hot plate for a few hours until cured. Can also leave the PDMS out at room temperature overnight until cured.
7. Once cured use a razor blade to cut squares large enough for a 5mm diameter hole. Take a 5mm diameter hole puncher and punch a hole into the PDMS block.

Experimental setup

1. Clean PDMS well with isopropyl alcohol and rinse with ddH_2O.
2. Rinse acrylamide brush coverslip with ddH_2O and air dry.
3. Use a pipette tip to place UV-curable glue (RapidFix) onto the bottom of the PDMS mold and fix onto the acrylamide brush coverslip.
4. Use UV light to cure the glue. Check that the PDMS mold is stuck onto the coverslip.
5. **Prepare active premix**
    a. Quickly thaw one aliquot of active premix (3.73µl) and one aliquot of 6mg/ml GMPCPP microtubules and leave on bench.
    b. Add 0.6µl of 10mM ATP and 0.67µl of 12% Pluronic F127 to the premix.
    c. Add 1µl of 6mg/ml GMPCPP microtubules to the premix.
6. Fill the PDMS well with ~60µl of silicon oil (viscosities varying from 100mPa s – 1000mPa s).
7. Take 0.75µl of active microtubule network and inject it to the bottom of the well. The active network should wet the surface of the coverslip.
8. Allow active network to settle into the 2D oil/water interface (~30min-1 hr) before imaging.

References

1. Cavagna, A. & Giardina, I. Bird Flocks as Condensed Matter. *Annual Review of Condensed Matter Physics* **5**, 183–207 (2014).
2. Katz, Y., Tunstrøm, K., Ioannou, C. C., Huepe, C. & Couzin, I. D. Inferring the structure and dynamics of interactions in schooling fish. *PNAS* **108**, 18720–18725 (2011).
3. Dell'Arciprete, D. *et al.* A growing bacterial colony in two dimensions as an active nematic. *Nat Commun* **9**, 1–9 (2018).
4. Sanchez, T., Chen, D. T. N., DeCamp, S. J., Heymann, M. & Dogic, Z. Spontaneous motion in hierarchically assembled active matter. *Nature* **491**, 431–434 (2012).
5. Nédélec, F. J., Surrey, T., Maggs, A. C. & Leibler, S. Self-organization of microtubules and motors. *Nature* **389**, 305–308 (1997).
6. Schaller, V., Weber, C., Semmrich, C., Frey, E. & Bausch, A. R. Polar patterns of driven filaments. *Nature* **467**, 73–77 (2010).
7. Theurkauff, I., Cottin-Bizonne, C., Palacci, J., Ybert, C. & Bocquet, L. Dynamic Clustering in Active Colloidal Suspensions with Chemical Signaling. *Phys. Rev. Lett.* **108**, 268303 (2012).
8. Ginelli, F., Peruani, F., Bär, M. & Chaté, H. Large-Scale Collective Properties of Self-Propelled Rods. *Phys. Rev. Lett.* **104**, 184502 (2010).
9. Palacci, J., Sacanna, S., Steinberg, A. P., Pine, D. J. & Chaikin, P. M. Living Crystals of Light-Activated Colloidal Surfers. *Science* **339**, 936–940 (2013).
10. Narayan, V., Ramaswamy, S. & Menon, N. Long-Lived Giant Number Fluctuations in a Swarming Granular Nematic. *Science* **317**, 105–108 (2007).
11. Vicsek, T., Czirók, A., Ben-Jacob, E., Cohen, I. & Shochet, O. Novel Type of Phase Transition in a System of Self-Driven Particles. *Phys. Rev. Lett.* **75**, 1226–1229 (1995).
12. Marchetti, M. C. *et al.* Hydrodynamics of soft active matter. *Rev. Mod. Phys.* **85**, 1143–1189 (2013).
13. Toner, J. & Tu, Y. Long-Range Order in a Two-Dimensional Dynamical XY Model: How Birds Fly Together. *Physical Review Letters* **75**, 4326–4329 (1995).
14. Hatwalne, Y., Ramaswamy, S., Rao, M. & Simha, R. A. Rheology of Active-Particle Suspensions. *Phys. Rev. Lett.* **92**, 118101 (2004).
15. Giomi, L., Bowick, M. J., Ma, X. & Marchetti, M. C. Defect Annihilation and Proliferation in Active Nematics. *Phys. Rev. Lett.* **110**, 228101 (2013).
16. Giomi, L. Geometry and Topology of Turbulence in Active Nematics. *Phys. Rev. X* **5**, 031003 (2015).
17. Giomi, L., Bowick, M. J., Mishra, P., Sknepnek, R. & Marchetti, M. C. Defect dynamics in active nematics. *Philosophical Transactions of the Royal Society A: Mathematical, Physical and Engineering Sciences* **372**, 20130365–20130365 (2014).
18. Ravnik, M. & Yeomans, J. M. Confined Active Nematic Flow in Cylindrical Capillaries. *Phys. Rev. Lett.* **110**, 026001 (2013).
19. Shendruk, T. N., Doostmohammadi, A., Thijssen, K. & Yeomans, J. M. Dancing disclinations in confined active nematics. *Soft Matter* **13**, 3853–3862 (2017).

20. Buhl, J. *et al.* From Disorder to Order in Marching Locusts. *Science* **312**, 1402–1406 (2006).
21. Valadares, L. F. *et al.* Catalytic Nanomotors: Self-Propelled Sphere Dimers. *Small* **6**, 565–572 (2010).
22. Kron, S. J. & Spudich, J. A. Fluorescent actin filaments move on myosin fixed to a glass surface. *Proc Natl Acad Sci U S A* **83**, 6272–6276 (1986).
23. Wang, Y. *et al.* Bipolar Electrochemical Mechanism for the Propulsion of Catalytic Nanomotors in Hydrogen Peroxide Solutions. *Langmuir* **22**, 10451–10456 (2006).
24. Nogales, E., Whittaker, M., Milligan, R. A. & Downing, K. H. High-Resolution Model of the Microtubule. *Cell* **96**, 79–88 (1999).
25. Mandelkow, E. M., Mandelkow, E. & Milligan, R. A. Microtubule dynamics and microtubule caps: a time-resolved cryo-electron microscopy study. *The Journal of Cell Biology* **114**, 977–991 (1991).
26. Arnal, I. & Wade, R. H. How does taxol stabilize microtubules? *Current Biology* **5**, 900–908 (1995).
27. Carlier, M. F. & Pantaloni, D. Kinetic analysis of guanosine 5'-triphosphate hydrolysis associated with tubulin polymerization. *Biochemistry* **20**, 1918–1924 (1981).
28. Mitchison, T. & Kirschner, M. Dynamic instability of microtubule growth. *Nature* **312**, 237–242 (1984).
29. Downing, K. H. & Nogales, E. Tubulin structure: insights into microtubule properties and functions. *Current Opinion in Structural Biology* **8**, 785–791 (1998).
30. Schiff, P. B. & Horwitz, S. B. Taxol stabilizes microtubules in mouse fibroblast cells. *Proc Natl Acad Sci U S A* **77**, 1561–1565 (1980).
31. Hyman, A. A., Salser, S., Drechsel, D. N., Unwin, N. & Mitchison, T. J. Role of GTP hydrolysis in microtubule dynamics: information from a slowly hydrolyzable analogue, GMPCPP. *Mol Biol Cell* **3**, 1155–1167 (1992).
32. Hawkins, T. L., Sept, D., Mogessie, B., Straube, A. & Ross, J. L. Mechanical Properties of Doubly Stabilized Microtubule Filaments. *Biophys J* **104**, 1517–1528 (2013).
33. Hirst, L. S. *Fundamentals of Soft Matter Science*. (CRC Press, 2013).
34. Gittes, F., Mickey, B., Nettleton, J. & Howard, J. Flexural rigidity of microtubules and actin filaments measured from thermal fluctuations in shape. *J. Cell Biol.* **120**, 923–934 (1993).
35. Hyman, A. A., Chrétien, D., Arnal, I. & Wade, R. H. Structural changes accompanying GTP hydrolysis in microtubules: information from a slowly hydrolyzable analogue guanylyl-(alpha,beta)-methylene-diphosphonate. *The Journal of Cell Biology* **128**, 117–125 (1995).
36. Edozie, B. *et al.* Self-Organization of Spindle-Like Microtubule Structures. *bioRxiv* 624874 (2019) doi:10.1101/624874.
37. Vale, R. D., Reese, T. S. & Sheetz, M. P. Identification of a novel force-generating protein, kinesin, involved in microtubule-based motility. *Cell* **42**, 39–50 (1985).
38. Vale, R. D. *et al.* Direct observation of single kinesin molecules moving along microtubules. *Nature* **380**, 451–453 (1996).

39. Woehlke, G. *et al.* Microtubule Interaction Site of the Kinesin Motor. *Cell* **90**, 207–216 (1997).
40. Vale, R. D. The Molecular Motor Toolbox for Intracellular Transport. *Cell* **112**, 467–480 (2003).
41. Urrutia, R., McNiven, M. A., Albanesi, J. P., Murphy, D. B. & Kachar, B. Purified kinesin promotes vesicle motility and induces active sliding between microtubules in vitro. *Proc Natl Acad Sci U S A* **88**, 6701–6705 (1991).
42. Taylor, E. W. & Borisy, G. G. Kinesin Processivity. *J Cell Biol* **151**, 27–30 (2000).
43. Schnitzer, M. J. & Block, S. M. Kinesin hydrolyses one ATP per 8-nm step. *Nature* **388**, 386–390 (1997).
44. Yildiz, A., Tomishige, M., Vale, R. D. & Selvin, P. R. Kinesin Walks Hand-Over-Hand. *Science* **303**, 676–678 (2004).
45. Heald, R. *et al.* Self-organization of microtubules into bipolar spindles around artificial chromosomes in Xenopus egg extracts. *Nature* **382**, 420–425 (1996).
46. Sanchez, T., Welch, D., Nicastro, D. & Dogic, Z. Cilia-Like Beating of Active Microtubule Bundles. *Science* **333**, 456–459 (2011).
47. Pazour, G. J., Agrin, N., Leszyk, J. & Witman, G. B. Proteomic analysis of a eukaryotic cilium. *J Cell Biol* **170**, 103–113 (2005).
48. Pringle, J. *et al.* Microtubule organization by kinesin motors and microtubule crosslinking protein MAP65. *J. Phys.: Condens. Matter* **25**, 374103 (2013).
49. Stanhope, K. T., Yadav, V., Santangelo, C. D. & Ross, J. L. Contractility in an extensile system. *Soft Matter* **13**, 4268–4277 (2017).
50. Hess, H. *et al.* Molecular Self-Assembly of "Nanowires" and "Nanospools" Using Active Transport. *Nano Lett.* **5**, 629–633 (2005).
51. Lam, A. T., Curschellas, C., Krovvidi, D. & Hess, H. Controlling self-assembly of microtubule spools via kinesin motor density. *Soft Matter* **10**, 8731–8736 (2014).
52. Liu, H. *et al.* Biomolecular Motor-Powered Self-Assembly of Dissipative Nanocomposite Rings. *Adv. Mater.* **20**, 4476–4481 (2008).
53. Liu, L., Tüzel, E. & Ross, J. L. Loop formation of microtubules during gliding at high density. *Journal of Physics: Condensed Matter* **23**, 374104 (2011).
54. Tan, A. J., Chapman, D. E., Hirst, L. S. & Xu, J. Understanding the role of transport velocity in biomotor-powered microtubule spool assembly. *RSC Adv.* **6**, 79143–79146 (2016).
55. Lam, A. T. *et al.* Cytoskeletal motor-driven active self-assembly in in vitro systems. *Soft Matter* (2015) doi:10.1039/c5sm02042e.
56. Liu, L., Tüzel, E. & Ross, J. L. Loop formation of microtubules during gliding at high density. *J Phys Condens Matter* **23**, 374104 (2011).
57. Selinger, J. V. *Introduction to the Theory of Soft Matter: From Ideal Gases to Liquid Crystals*. (Springer, 2016).
58. Rodarte, A. L., Pandolfi, R. J., Ghosh, S. & Hirst, L. S. Quantum dot/liquid crystal composite materials: self-assembly driven by liquid crystal phase transition templating. *J. Mater. Chem. C* **1**, 5527–5532 (2013).
59. Henkin, G., DeCamp, S. J., Chen, D. T. N., Sanchez, T. & Dogic, Z. Tunable dynamics of microtubule-based active isotropic gels. *Philos Trans A Math Phys Eng Sci* **372**, (2014).

60. Yang, Y., Lin, J., Kaytanli, B., Saleh, O. A. & Valentine, M. T. Direct correlation between creep compliance and deformation in entangled and sparsely crosslinked microtubule networks. *Soft Matter* **8**, 1776–1784 (2012).
61. Lemma, L. M., DeCamp, S. J., You, Z., Giomi, L. & Dogic, Z. Statistical properties of autonomous flows in 2D active nematics. *Soft Matter* **15**, 3264–3272 (2019).
62. Hemingway, E. J., Mishra, P., Marchetti, M. C. & Fielding, S. M. Correlation lengths in hydrodynamic models of active nematics. *Soft Matter* **12**, 7943–7952 (2016).
63. Leonardo, R. D. *et al.* Bacterial ratchet motors. *PNAS* **107**, 9541–9545 (2010).
64. Hardoüin, J. *et al.* Reconfigurable flows and defect landscape of confined active nematics. *Commun Phys* **2**, 1–9 (2019).
65. Opathalage, A. *et al.* Self-organized dynamics and the transition to turbulence of confined active nematics. *PNAS* 201816733 (2019) doi:10.1073/pnas.1816733116.
66. Keber, F. C. *et al.* Topology and dynamics of active nematic vesicles. *Science* **345**, 1135–1139 (2014).
67. Henkes, S., Marchetti, M. C. & Sknepnek, R. Dynamical patterns in nematic active matter on a sphere. *Phys. Rev. E* **97**, 042605 (2018).
68. Ellis, P. W. *et al.* Curvature-induced defect unbinding and dynamics in active nematic toroids. *Nature Physics* **14**, 85–90 (2018).
69. Guillamat, P., Ignés-Mullol, J. & Sagués, F. Patterning active materials with addressable soft interfaces. *Proceedings of the National Academy of Sciences* **113**, 5498–5502 (2016).
70. Leduc, C. *et al.* Molecular crowding creates traffic jams of kinesin motors on microtubules. *Proc. Natl. Acad. Sci. U.S.A.* **109**, 6100–6105 (2012).
71. Conway, L., Wood, D., Tüzel, E. & Ross, J. L. Motor transport of self-assembled cargos in crowded environments. *PNAS* **109**, 20814–20819 (2012).
72. Aref, H. Stirring by chaotic advection. *Journal of Fluid Mechanics* **143**, 1–21 (1984).
73. Aref, H. *et al.* Frontiers of chaotic advection. *Rev. Mod. Phys.* **89**, 025007 (2017).
74. Ottino, J. M. *The kinematics of mixing: stretching, chaos, and transport*. (Cambridge University Press, 1989).
75. Greiner, W. Lyapunov Exponents and Chaos. in *Classical Mechanics: Systems of Particles and Hamiltonian Dynamics* (ed. Greiner, W.) 503–516 (Springer, 2010). doi:10.1007/978-3-642-03434-3_26.
76. Aref, H. & Balachandar, S. Chaotic advection in a Stokes flow. *The Physics of Fluids* **29**, 3515–3521 (1986).
77. Boyland, P. L., Aref, H. & Stremler, M. A. Topological fluid mechanics of stirring. *Journal of Fluid Mechanics* **403**, 277–304 (2000).
78. Thiffeault, J.-L. Measuring Topological Chaos. *Phys. Rev. Lett.* **94**, 084502 (2005).
79. Thiffeault, J.-L. & Finn, M. D. Topology, braids and mixing in fluids. *Philosophical Transactions of the Royal Society of London A: Mathematical, Physical and Engineering Sciences* **364**, 3251–3266 (2006).
80. Finn, M. D. & Thiffeault, J.-L. Topological Optimization of Rod-Stirring Devices. *SIAM Rev.* **53**, 723–743 (2011).
81. Thiffeault, J.-L. & Budisic, M. Braidlab: A Software Package for Braids and Loops. *arXiv:1410.0849 [math]* (2014).

82. Kawamura, R., Kakugo, A., Osada, Y. & Gong, J. P. Microtubule bundle formation driven by ATP: the effect of concentrations of kinesin, streptavidin and microtubules. *Nanotechnology* **21**, 145603 (2010).
83. Wada, S. *et al.* Effect of length and rigidity of microtubules on the size of ring-shaped assemblies obtained through active self-organization. *Soft Matter* **11**, 1151–1157 (2015).
84. Inoue, D. *et al.* Growth of ring-shaped microtubule assemblies through stepwise active self-organisation. *Soft Matter* **9**, 7061–7068 (2013).
85. Liu, H. & Bachand, G. D. Understanding energy dissipation and thermodynamics in biomotor-driven nanocomposite assemblies. *Soft Matter* **7**, 3087–3091 (2011).
86. Needleman, D. J. *et al.* Synchrotron X-ray diffraction study of microtubules buckling and bundling under osmotic stress: a probe of interprotofilament interactions. *Phys. Rev. Lett.* **93**, 198104 (2004).
87. VanDelinder, V., Brener, S. & Bachand, G. D. Mechanisms Underlying the Active Self-Assembly of Microtubule Rings and Spools. *Biomacromolecules* **17**, 1048–1056 (2016).
88. Shankar, S., Ramaswamy, S., Marchetti, M. C. & Bowick, M. J. Defect Unbinding in Active Nematics. *Phys. Rev. Lett.* **121**, 108002 (2018).
89. Heidenreich, S., Dunkel, J., Klapp, S. H. L. & Bär, M. Hydrodynamic length-scale selection in microswimmer suspensions. *Phys. Rev. E* **94**, 020601 (2016).
90. Doostmohammadi, A., Shendruk, T. N., Thijssen, K. & Yeomans, J. M. Onset of meso-scale turbulence in active nematics. *Nature Communications* **8**, 15326 (2017).
91. Muzzio, F. J., Swanson, P. D. & Ottino, J. M. The statistics of stretching and stirring in chaotic flows. *Physics of Fluids A: Fluid Dynamics* **3**, 822–834 (1991).
92. Chaiken, J., Chevray, R., Tabor, M. & Tan, Q. M. Experimental study of Lagrangian turbulence in a Stokes flow. *Proc. R. Soc. Lond. A* **408**, 165–174 (1986).
93. Vikhansky, A. Chaotic advection of finite-size bodies in a cavity flow. *Physics of Fluids (1994-present)* **15**, 1830–1836 (2003).
94. Gouillart, E., Thiffeault, J.-L. & Finn, M. D. Topological mixing with ghost rods. *Phys. Rev. E* **73**, 036311 (2006).
95. Crocker, J. C. & Grier, D. G. Methods of Digital Video Microscopy for Colloidal Studies. *Journal of Colloid and Interface Science* **179**, 298–310 (1996).
96. Jeune-Smith, Y. & Hess, H. Engineering the length distribution of microtubules polymerized in vitro. *Soft Matter* **6**, 1778–1784 (2010).
97. Roberts, E., Sindi, S., Smith, S. & Mitchell, K. Ensemble-based Topological Entropy Calculation (E-tec). *arXiv:1809.01005 [physics]* (2018).
98. Greenberg, E. P. & Canale-Parola, E. Motility of flagellated bacteria in viscous environments. *J Bacteriol* **132**, 356–358 (1977).
99. Tung, C. *et al.* Fluid viscoelasticity promotes collective swimming of sperm. *Scientific Reports* **7**, 3152 (2017).
100. Guillamat, P., Ignés-Mullol, J., Shankar, S., Marchetti, M. C. & Sagués, F. Probing the shear viscosity of an active nematic film. *Phys. Rev. E* **94**, 060602 (2016).
101. Tan, A. J. *et al.* Topological chaos in active nematics. *Nat. Phys.* 1–7 (2019) doi:10.1038/s41567-019-0600-y.

102. Lemma, L. M., DeCamp, S. J., You, Z., Giomi, L. & Dogic, Z. Statistical Properties of Autonomous Flows in 2D Active Nematics. *Soft Matter* (2019) doi:10.1039/C8SM01877D.
103. Perugini, D., Poli, G. & Mazzuoli, R. Chaotic advection, fractals and diffusion during mixing of magmas: evidence from lava flows. *Journal of Volcanology and Geothermal Research* **124**, 255–279 (2003).
104. Nishiguchi, D., Nagai, K. H., Chaté, H. & Sano, M. Long-range nematic order and anomalous fluctuations in suspensions of swimming filamentous bacteria. *Phys. Rev. E* **95**, 020601 (2017).
105. Schaller, V. & Bausch, A. R. Topological defects and density fluctuations in collectively moving systems. *PNAS* **110**, 4488–4493 (2013).